

ADAPTIVE OPTICS OPTICAL COHERENCE TOMOGRAPHY FOR *IN VIVO* RETINAL IMAGING

by

Yifan Jian

B.Sc., University of Shanghai for Science and Technology, 2010

Thesis Submitted in Partial Fulfillment of the
Requirements for the Degree of
Doctor of Philosophy

in the
School of Engineering Science
Faculty of Applied Sciences

© Yifan Jian 2014

SIMON FRASER UNIVERSITY

Spring 2014

All rights reserved.

However, in accordance with the *Copyright Act of Canada*, this work may be reproduced, without authorization, under the conditions for "Fair Dealing." Therefore, limited reproduction of this work for the purposes of private study, research, criticism, review and news reporting is likely to be in accordance with the law, particularly if cited appropriately.

Approval

Name: Yifan Jian

Degree: Doctor of Philosophy

Title of Thesis: *ADAPTIVE OPTICS OPTICAL COHERENCE
TOMOGRAPHY FOR IN VIVO RETINAL IMAGING*

Examining Committee: Chair: Dr. Jie Liang, P. Eng.
Associate Professor

Dr. Marinko V. Sarunic, P.Eng.
Senior Supervisor
Associate Professor

Dr. Robert J. Zawadzki
Supervisor
Associate Research Professor

Dr. Mirza Faisal Beg, P.Eng.
Supervisor
Associate Professor

Dr. Andrew Rawicz, P.Eng.
Internal Examiner
Professor
School of Engineering Science

Dr. Michael Pircher
External Examiner
Associate Professor
Medical Physics
Medical University of Vienna

Date Defended/Approved: April 25, 2014

Partial Copyright Licence



The author, whose copyright is declared on the title page of this work, has granted to Simon Fraser University the non-exclusive, royalty-free right to include a digital copy of this thesis, project or extended essay[s] and associated supplemental files (“Work”) (title[s] below) in Summit, the Institutional Research Repository at SFU. SFU may also make copies of the Work for purposes of a scholarly or research nature; for users of the SFU Library; or in response to a request from another library, or educational institution, on SFU’s own behalf or for one of its users. Distribution may be in any form.

The author has further agreed that SFU may keep more than one copy of the Work for purposes of back-up and security; and that SFU may, without changing the content, translate, if technically possible, the Work to any medium or format for the purpose of preserving the Work and facilitating the exercise of SFU’s rights under this licence.

It is understood that copying, publication, or public performance of the Work for commercial purposes shall not be allowed without the author’s written permission.

While granting the above uses to SFU, the author retains copyright ownership and moral rights in the Work, and may deal with the copyright in the Work in any way consistent with the terms of this licence, including the right to change the Work for subsequent purposes, including editing and publishing the Work in whole or in part, and licensing the content to other parties as the author may desire.

The author represents and warrants that he/she has the right to grant the rights contained in this licence and that the Work does not, to the best of the author’s knowledge, infringe upon anyone’s copyright. The author has obtained written copyright permission, where required, for the use of any third-party copyrighted material contained in the Work. The author represents and warrants that the Work is his/her own original work and that he/she has not previously assigned or relinquished the rights conferred in this licence.

Simon Fraser University Library
Burnaby, British Columbia, Canada

revised Fall 2013

Ethics Statement



The author, whose name appears on the title page of this work, has obtained, for the research described in this work, either:

- a. human research ethics approval from the Simon Fraser University Office of Research Ethics,

or

- b. advance approval of the animal care protocol from the University Animal Care Committee of Simon Fraser University;

or has conducted the research

- c. as a co-investigator, collaborator or research assistant in a research project approved in advance,

or

- d. as a member of a course approved in advance for minimal risk human research, by the Office of Research Ethics.

A copy of the approval letter has been filed at the Theses Office of the University Library at the time of submission of this thesis or project.

The original application for approval and letter of approval are filed with the relevant offices. Inquiries may be directed to those authorities.

Simon Fraser University Library
Burnaby, British Columbia, Canada

update Spring 2010

Abstract

Optical coherence tomography (OCT) is a non-invasive micrometer-resolution volumetric imaging modality that has been employed in diverse applications. In this thesis, we first describe a GPU accelerated program to perform FDOCT data processing and real time 3D volumetric rendering. The real time visualization of volumetric images provided by the GPU acceleration was essential to the rest of the work described in this thesis.

Small animal models of retinal diseases serve as a vital component in vision research, and non-invasive *in vivo* imaging is becoming an increasingly important tool in the field. We describe the first adaptive optics optical coherence tomography (AOOCT) imaging system for high resolution mouse retinal imaging. Images of mouse retina acquired with AOOCT showed significant improvement in the brightness and contrast of capillaries and nerve fiber bundles. However, the accuracy of wavefront sensing limited the performance of AOOCT.

A novel wavefront sensorless adaptive optics (WSAO) OCT system was developed to overcome the issues associated with conventional wavefront sensing. Combination of WSAO with OCT allows coherence gated, depth resolved aberration correction. Images of both pigmented and albino mouse retinas acquired using WSAO OCT system demonstrated superior image quality. The real time high resolution WSAO OCT was leveraged for a time course study of laser exposure in the retina.

Keywords: Adaptive Optics, Optical Coherence Tomography, Wavefront Sensorless, Graphics Processing Unit, Mouse retina

Dedicated to my family

Acknowledgements

First and foremost, I would like to express my deepest and sincerest gratitude to my senior supervisor Dr. Marinko Sarunic for his continuous support of my Ph.D study and research, for his patience, encouragement, immense knowledge and most importantly for sharing his passion in the research. His guidance helped me throughout the research and writing of this thesis. I could not have imagined having a better advisor and mentor.

I would like to thank my committee members Dr. Robert Zawadzki for equipping me with knowledge on adaptive optics and inspiring me with great ideas. I would like to thank Dr. Faisal Beg for teaching me the skills in image processing and offering advices on this thesis.

I am most grateful to be part of the Biomedical Optics Research Group (BORG) family. I thank all the BORG members for their friendships.

Last but not least, I would like to thank my family for their unconditional love and continued support in all my endeavours.

Table of Contents

| | |
|---|-----------|
| Approval..... | ii |
| Partial Copyright Licence | iii |
| Ethics Statement..... | iv |
| Abstract..... | v |
| Dedication | vi |
| Acknowledgements..... | vii |
| Table of Contents..... | viii |
| List of Tables..... | xi |
| List of Figures..... | xii |
| List of Acronyms..... | xviii |
| | |
| Chapter 1. Introduction..... | 1 |
| 1.1. Optical coherence tomography | 1 |
| 1.2. Mouse retinal imaging | 5 |
| 1.3. Overview of the thesis..... | 7 |
| | |
| Chapter 2. Adaptive Optics in Ophthalmic Imaging | 9 |
| 2.1. Overview of Adaptive Optics | 9 |
| 2.2. Point spread function | 11 |
| 2.3. Wavefront aberration..... | 12 |
| 2.4. Wavefront Corrector..... | 14 |
| 2.5. Wavefront sensor | 15 |
| 2.5.1. The principle of Shack-Hartmann wavefront sensor..... | 15 |
| 2.5.2. Centroiding | 17 |
| 2.5.3. Wavefront Reconstruction | 18 |
| 2.6. Summary..... | 19 |
| | |
| Chapter 3. Graphics processing unit accelerated optical coherence tomography processing at megahertz axial scan rate and high resolution video rate volumetric rendering | 20 |
| 3.1. Introduction | 20 |
| 3.2. Methods | 21 |
| 3.3. Results and Discussion..... | 25 |
| 3.4. Summary..... | 30 |
| | |
| Chapter 4. Adaptive optics optical coherence tomography for in vivo mouse retinal imaging | 32 |
| 4.1. Introduction | 32 |
| 4.2. Methods | 34 |
| 4.2.1. FD-OCT Engine..... | 34 |
| 4.2.2. Wavefont sensor..... | 35 |

| | |
|-------------------------------------|----|
| 4.2.3. Adaptive Optics FD-OCT | 35 |
| 4.2.4. Mouse Handling..... | 38 |
| 4.3. Results | 39 |
| 4.4. Discussion..... | 48 |
| 4.5. High resolution WFS | 51 |
| 4.6. Summary..... | 53 |

Chapter 5. Wavefront Sensorless Adaptive Optics Optical Coherence Tomography for in vivo retinal imaging in mice 55

| | |
|---|----|
| 5.1. Introduction | 55 |
| 5.2. Methods | 57 |
| 5.2.1. AO FD-OCT engine | 57 |
| 5.2.2. Imaged Based Wavefront Sensorless Adaptive Optics Modal Optimization Algorithm | 59 |
| 5.2.3. Mouse Handling..... | 61 |
| 5.3. Results | 62 |
| 5.3.1. Phantom imaging..... | 62 |
| 5.3.2. Pigmented mouse retinal imaging | 64 |
| 5.3.3. Albino mouse retinal imaging | 66 |
| 5.4. Discussion..... | 67 |
| 5.5. Summary..... | 70 |

Chapter 6. In vivo real time visualization of the mouse retina response to laser exposure using wavefront sensorless adaptive optics optical coherence tomography 71

| | |
|-------------------------|----|
| 6.1. Introduction | 71 |
| 6.2. Method | 72 |
| 6.3. Results | 73 |
| 6.4. Discussion..... | 75 |
| 6.5. Summary..... | 75 |

Chapter 7. Conclusion and future work 77

| | |
|--|----|
| 7.1. Conclusion | 77 |
| 7.2. Future work | 78 |
| 7.2.1. Refinement of WSAO OCT system | 78 |
| Custom high NA objective lens for mouse retinal imaging | 78 |
| Reduction of motion artifact during in vivo retinal imaging in mice..... | 79 |
| Faster converging algorithm for WSAO..... | 79 |
| 7.2.2. Wavefront sensorless adaptive optics simultaneous two-photon excitation fluorescence and optical coherence tomography using the same light source | 80 |
| 7.2.3. Extended depth of focus optical coherence tomography with wavefront sensorless adaptive optics..... | 81 |
| 7.3. Acknowledgements | 82 |

| | |
|---|-----------|
| References | 83 |
| Appendix A. Zernike Polynomials up to 5th order | 96 |

List of Tables

| | | |
|---------|---|---|
| Table 1 | Comparison of the human and mouse eye optics parameters. | 7 |
|---------|---|---|

List of Figures

| | | |
|------------|---|----|
| Figure 1.1 | Graphical illustration of the technical terms used in OCT..... | 2 |
| Figure 1.2 | Basic schematic of different types of OCT system. (a) Time Domain OCT. (b) Swept Source OCT. (c) Spectral Domain OCT..... | 3 |
| Figure 1.3 | Comparison of mouse retina B-scan image (left) with histology (right). NFL, Nerve Fiber Layer; GLC, Ganglion Cell Layer; IPL, Inner Plexiform Layer; INL, Inner Nuclear Layer; OPL, Outer Plexiform Layer; ONL, Outer Nuclear Layer; ELM, External limiting membrane; IS, Inner Segment; OS, Outer Segment; RPE, Retinal Pigment Epithelium; CH, Choroid..... | 6 |
| Figure 1.4 | Simplified schematic of human and mouse eye model. The mouse eye model was scaled up to size of human's for comparison..... | 7 |
| Figure 2.1 | Simplified schematic of a basic adaptive optics imaging system. Black arrow indicates the direction that light originated from the sample enters the optical system. The red lines represent the light used by the imaging system, and the green lines represent a different wavelength of light that is commonly used as a beacon for wavefront sensing..... | 11 |
| Figure 2.2 | Synthetic mouse photoreceptor mosaic..... | 13 |
| Figure 2.3 | Simulated retinal images of mouse photoreceptors mosaic under different imaging conditions..... | 14 |
| Figure 2.4 | Picture of Iris AO PT-111 DM. Reprinted with Iris AO's permission..... | 15 |
| Figure 2.5 | Principle of operation of a Shack-Hartmann wavefront sensor. The wavefront spot patterns produced by a planar wavefront (a) and by an arbitrarily aberrated wavefront (b). The blue dotted circles represent lenslets..... | 17 |
| Figure 3.1 | CUDA Profiler Timeline for SS-OCT processing and volume rendering pipeline. Memcpy HtoD [async] is transferring the raw data, subDC_PadCom is a kernel with the function of type conversion, DC subtraction and zero padding. spVector2048C_kernelTex is a kernel called by the cuFFT library which performs the FFT. CropMLS performs the modulus and Log. Memcpy DtoA [sync] copy the processed OCT data into CUDA 3D Array for volume rendering..... | 24 |

| | | |
|------------|---|----|
| Figure 3.2 | Flow chart for OCT acquisition and GPU processing. The italicized procedure names in the Processing Kernels represent the blocks that were dropped for the SS OCT implementation. | 25 |
| Figure 3.3 | OCT A-Scan batch processing rate. For SSOCT, processing pipeline includes DC subtraction, FFT, modulus and Log. For SDOCT, processing pipeline includes linear interpolation, DC subtraction, dispersion compensation, FFT, modulus and Log. | 26 |
| Figure 3.4 | (a) Screen captures of OCT images (Video 1). Upper left: OCT B-scan. Upper right: <i>En face</i> view. Lower left: 3D volumetric rendering. (b) Real time acquisition and processing of human retinal images (Video 2 [23], QuickTime, 3.33MB). | 27 |
| Figure 3.5 | Screen captures of OCT Anterior Chamber Imaging session. | 27 |
| Figure 3.6 | The svOCT images are presented in (a), (b) and (c). Color-coded R/G/B composite of (a), (b) and (c), where each color represents: NFL - blue, IPL - green, and OPL - red is shown in (e). The combined intensity <i>en face</i> image of all depth regions of interest is presented in (d). Scale bar: 200 μm | 29 |
| Figure 3.7 | Comparison between the intensity <i>en face</i> images (a, c, e, g) and the color-coded composite svOCT <i>en face images</i> (b, d, f, h), respectively. Images (a–d) were acquired at the optic nerve head region, and images (e–h) were acquired in the macula. Scale bar: 400 μm | 30 |
| Figure 4.1 | (Top) Schematic of the small animal AO FDOCT system. (Bottom) Photograph of optical layout. DC - dispersion compensation; DM - deformable mirror; FC-20/80 fiber coupler, 20% of the light from SLD goes to sample arm, 80% goes to reference arm; GM1, GM2 - horizontal and vertical galvo scanning mirrors; FL - fundus lens; PC - polarization controller. PBS - pellicle beam splitter; SLD, superluminescent diode; WFS, wavefront sensor; L – achromatic lenses: L0: (f=16mm); L1, L2: (f=300mm); L3, L4: (f=200mm); L5, L6: (f=150mm); L7, (f=100mm) L8: (f=200mm); OBJ – objective: (f=25mm); ND, neutral density filter; P represents the location of the planes conjugated to the pupil throughout the system; R represents the retinal conjugate planes. Inset: the mouse and fundus lens combination can be translated to adjust the focus. GM1 is slow scan mirror and is presented unfolded for clarity. Note that the schematic is drawn for illustrative purposes only; it does not reflect the actual physical dimensions or the optical configuration of the system. | 37 |
| Figure 4.2 | (a) Schematic of the fundus lens positioned at the mouse cornea. (b) OCT image of a fundus lens near the cornea. (c) OCT image of a fundus lens in contact with the cornea. | 38 |

| | | |
|------------|--|----|
| Figure 4.3 | Images from the wavefront sensor camera and corresponding log scale B-scans acquired simultaneously at the same location. A single wavefront sensor spot (in the red dotted circles) are shown at higher magnification in the heat maps, and the corresponding intensity profiles were taken at the position of the black line. (a) WFS image with non-optimized focus. (b) WFS images acquired with the beam focus optimized on the outer retinal layers..... | 40 |
| Figure 4.4 | (a) Measurement of the system residual aberrations with a paper phantom in the retinal plane. (b) A representative trace of the RMS wavefront error during mouse imaging. The corresponding Zernike coefficients measured before (c) and during (d) AO correction while imaging a mouse retina with the AO FD-OCT. Note that the scale of vertical axis in (a) is 10 times smaller than that of (c) and (d). (e) Averaged magnitude of Zernike coefficients and standard deviation before and after correction as measured for sample of 8 mice. The Zernike coefficients follows the OSA standard for reporting the optical aberrations of eyes. | 41 |
| Figure 4.5 | A comparison of regular rodent OCT B-scan with high resolution AO-OCT B-scan (inside yellow dotted box acquired with AO-ON). Both images were acquired from C57BL/6J (pigmented) mouse, and were generated by averaging 20 motion corrected B-scans. A logarithmic intensity scale was used for both sets of data. Note the smaller speckle size seen on AO FD-OCT inset. Scale bar: 100 μ m..... | 42 |
| Figure 4.6 | <i>In vivo</i> OCT B-scans images. (left) acquired at the same eccentricity from the retinas of C57BL/6J (pigmented) mice and depth intensity profiles (right); (a) was acquired when AO is turned off (DM flat) (b) was acquired when AO was activated and focus set on the outer retina, (c) was acquired when AO was activated and shifting the focus through the AO software to the inner retina. Images (a, b, and c) were generated by averaging 20 B-scans and are presented on a linear intensity scale. Scale bar: 50 μ m..... | 43 |
| Figure 4.7 | Cross sectional images of the mouse retina acquired <i>in vivo</i> with the AO FD-OCT system. The focal plane was set on the inner retina by changing the defocus in the AO control software. The axial depths indicated by the brackets in the B-scan represent the locations of (a-c) <i>en face</i> projections of different retinal layers with AO-ON and (d-f) <i>en face</i> projections at the same location with AO-OFF (DM flat). Scale bar: 30 μ m. | 45 |

| | | |
|-------------|---|----|
| Figure 4.8 | Cross sectional and <i>en face</i> images (IPL, INL, OPL and PRL) of the mouse retina acquired <i>in vivo</i> with the AO FD-OCT system. The focal plane was adjusted on the layers of interest as indicated by the red brackets in the B-scan images by changing the defocus in the AO control software. The axial depths indicated by the brackets in the B-scan represent the locations of (a-d) <i>en face</i> projections of the different retinal layers with AO-ON and (e-h) <i>en face</i> projections at the same location with AO-OFF (DM flat). Normalized line graphs of the image intensity taken across the capillaries at the locations labeled 1, 2 and 3 in (c) and (g) are presented in the bottom panel. Scale bar: 30 μ m..... | 47 |
| Figure 4.9 | AO FDOCT images of the mouse photoreceptor layer acquired <i>in vivo</i> with (a) adaptive optics off and (b) with the adaptive optics activated. The bright, circular features observed in the <i>en face</i> images correspond to individual photoreceptors. Bottom row: the <i>en face</i> images are extracted from the depth positions of the photoreceptor layer identified in the B-scan and corresponding to (c) the inner / outer segment junctions, and (d) and (e) two different depths of the outer segments. Scale bar: 10 μ m..... | 48 |
| Figure 4.10 | Comparison between high resolution and low resolution wavefront sensor under different imaging NA. | 52 |
| Figure 4.11 | Comparison of the performance of low resolution WFS and masked high resolution WFS in the mouse retina. Images from top to bottom are wavefront sensor RMS error plots, Zernike coefficient plots and reconstructed wavefront before and after AO correction..... | 53 |
| Figure 5.1 | Schematic of the WSAO FD-OCT system: DC - dispersion compensation; DM - deformable mirror; FC - 20/80 fiber coupler, 20% of the light from SLD goes to sample arm, 80% goes to reference arm; GM1, GM2 - horizontal and vertical galvo scanning mirrors; FL - fundus lens; PC - polarization controller; SLD - superluminescent diode; L - achromatic lenses: L0: (f=16mm); L1, L2: (f=300mm); L3, L4: (f=200mm); L5, L6: (f=150mm); L7, (f=100mm) L8: (f=300mm); OBJ - objective: (f=25mm); ND - neutral density filter; P represents the location of the planes conjugated to the pupil throughout the system. GM1 is slow scan mirror and is presented unfolded for clarity. Note that the schematic is drawn for illustrative purposes only; it does not reflect the actual physical dimensions of the system. | 58 |
| Figure 5.2 | WSAO search algorithm flowchart. DM – Deformable Mirror; k_i^* - the optimized coefficient for Zernike mode i..... | 61 |

| | | |
|------------|--|----|
| Figure 5.3 | OCT images of a leaf with and without WSAO corrections. Bottom figure: (blue line graph) The summed intensity (merit function value) of <i>en face</i> images after optimization of each Zernike mode. (red bar graph) The optimized Zernike coefficient value for each Zernike mode. Scale bar: 20 μ m. The Zernike coefficients follow the OSA standard for reporting the optical aberrations of eyes..... | 63 |
| Figure 5.4 | Merit function during the optimization process. Only the first search iteration of 8 Zernike modes are shown for clarity of the presentation, further iterations resulted in an increased value of the merit function for some of the terms. The data presented in Figure 5.3 were obtained after the complete optimization process. | 64 |
| Figure 5.5 | Screen capture of an imaging session of a pigmented mouse. The first part of the video presents the WSAO optimization on the nerve fiber layer with a low resolution scanning pattern. The field of view (170x170 μ m) was close to the optic nerve head as indicated by the converging nerve fibers. The green arrow points to a capillary and the red arrow points to the edge of the blood vessel wall. The second part of the video that shows the high resolution images is displayed at 2x the acquisition speed, and the field of view was changed to 250x250 μ m and 333x333 μ m during acquisition..... | 65 |
| Figure 5.6 | WSAO OCT images of NFL of a pigmented mouse. (a) OCT B-scan in linear scale, emphasizing the location and depth of focus of the imaging beam at the NFL. (b-d) <i>En face</i> projection of the nerve fiber layer (generated within the red brackets in (a)) before (b) and after (c) WSAO optimization. (d) was acquired with a larger field of view after WSAO optimization. (e) (Blue line graph) the summed intensity (merit function value) of <i>en face</i> images after optimization of each Zernike mode. (Red bar graph) the optimized Zernike coefficient value for each Zernike mode. The RMS of the wavefront applied by the DM is 0.125 μ m. Scale bar: 25 μ m..... | 66 |
| Figure 5.7 | (a) Cross sectional images of the albino mouse retina acquired <i>in vivo</i> with the sensorless WSAO OCT system presented on a linear scale. The axial depths indicated by the brackets represent the location of the <i>en face</i> projection of the retinal layers of interests with AO-OFF (b) and AO-ON (c,d). Scale bar: 20 μ m. (e) The effect of AO correction is demonstrated by comparing the signal intensity across lines taken from the <i>en face</i> images at locations (b, red) and (c, blue). (f) (Blue line graph) The summed intensity (merit function value) of the <i>en face</i> images after optimization of each Zernike mode. (Red bar graph) The optimized Zernike coefficient value for each Zernike mode. The RMS of the wavefront applied by the DM is 0.175 μ m. | 67 |

| | | |
|------------|---|----|
| Figure 6.1 | Modified WSAO OCT system schematic. SLD - superluminescent diode; GM - galvo scanning mirrors; DM – deformable mirror; FC – fibre coupler..... | 73 |
| Figure 6.2 | OCT images of mouse retina before and after laser exposure, (a) and (d) are mouse retina OCT B-scan, <i>en face</i> projection were generated from the layers indicated by the green (ONL) and red (photoreceptors layer) box in the B-scan. (b) and (c) are images before laser exposure, and (e) and (f) are images after laser exposure..... | 74 |

List of Acronyms

| | |
|-------|---|
| ADC | analog-to-digital converter |
| AMD | Age-related Macular Degeneration |
| AO | Adaptive Optics |
| CH | Choroid |
| cSLO | confocal Scanning Laser Ophthalmoscope |
| CUDA | Compute Unified Device Architecture |
| DM | Deformable Mirror |
| FD | Fourier Domain |
| FDML | Fourier Domain Mode Locking |
| FDOCT | Fourier Domain Optical Coherence Tomography |
| GCL | Ganglion Cell Layer |
| GPU | Graphics Processing Unit |
| INL | Inner Nuclear Layer |
| IPL | Inner Plexiform Layer |
| IS | Inner Segment |
| LCI | Low Coherence Interferometry |
| NA | Numerical Aperture |
| NFL | Nerve Fiber Layer |
| OCT | Optical Coherence Tomography |
| ONL | Outer Nuclear Layer |
| OPL | Outer Plexiform Layer |
| OS | Outer Segment |
| PBS | Pellicle Beam Splitter |
| PRL | Photoreceptor Layer |
| pvOCT | phase variance OCT |
| RNFL | Retinal Nerve Fiber Layer |
| RPE | Retinal Pigment Epithelium |
| SD | Spectral Domain |
| SLO | Scanning Laser Ophthalmoscope |
| SNR | Signal to Noise Ratio |
| SRT | Selective Retinal Therapy |

| | |
|-------|---|
| SS | Swept Source |
| svOCT | speckle variance Optical Coherence Tomography |
| TD | Time Domain |
| TPEF | Two-photon Excitation Fluorescence |
| TSOCT | transverse-scanning OCT |
| WFS | Wavefront Sensor |
| WSAO | Wavefront Sensorless Adaptive Optics |

Chapter 1.

Introduction

1.1. Optical coherence tomography

Optical coherence tomography (OCT) is a non-invasive micron-resolution volumetric imaging modality based on the principle of low coherence interferometry (LCI). Fercher et al. in 1988 reported the first biological application of low-coherence interferometry for axial eye length measurement [1]. The name Optical Coherence Tomography appeared in the literature in the early 1990s and since then OCT has undergone tremendous development [2]. A detailed review of early work in LCI and OCT can be found in the paper published by A F Fercher [3]. OCT was initially targeted as a biomedical imaging tool primarily for ophthalmic application and later on was adopted in many other fields such as, gastroenterology, dermatology, and intra-arterial imaging, etc [4]. Also, OCT found its place in industrial applications such as non-destructive testing and evaluation of manufactured parts [5].

In OCT, a series of laterally adjacent depth-scans are acquired and composited to form a volumetric image as illustrated in Figure 1.1. The lateral OCT scan is either performed by moving the sample or by raster scanning the imaging beam across the sample. An OCT depth (axial) scan is called A-scan and a 2D cross-sectional image consisting of many A-scans is called a B-scan. The 2D projection view along the direction of A-scan is called an *en face* view or fundus view.

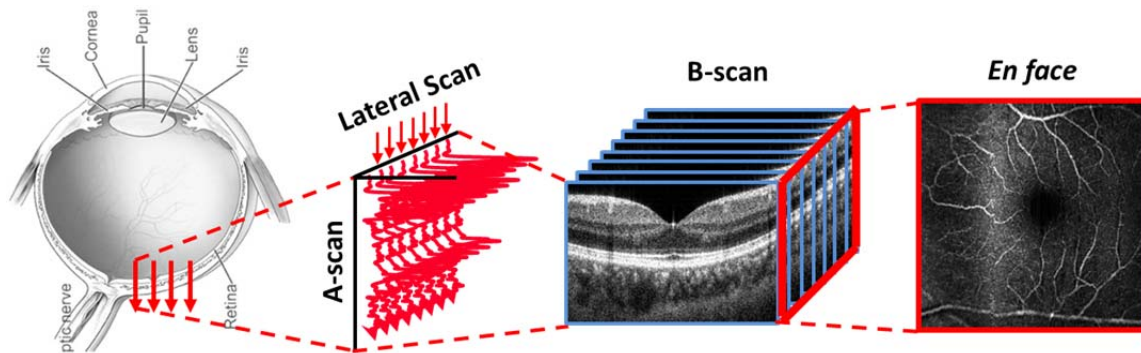


Figure 1.1 Graphical illustration of the technical terms used in OCT.

The principle and theory of OCT has been well established and discussed [4]. Briefly, OCT uses a Michelson interferometer, and in early time domain (TD) OCT systems, the depth-scan was performed by the moving the reference mirror as shown in Figure 1.2 (a). However, the needs for mechanical scanning to obtain A-scans in time domain OCT limited the speed and the signal to noise ratio. Shortly after the report of time domain OCT, the Fourier domain OCT (FDOCT) was developed with increased acquisition rate and system sensitivity [6]–[8]. Figure 1.2 (b) and (c) shows two types of Fourier domain OCT systems, spectral domain (SD) and swept source (SS) OCT. SD OCT system uses a broad bandwidth light source and a spectrometer as detector, and a SS OCT uses a wavelength sweeping light source and a photodiode as detector.

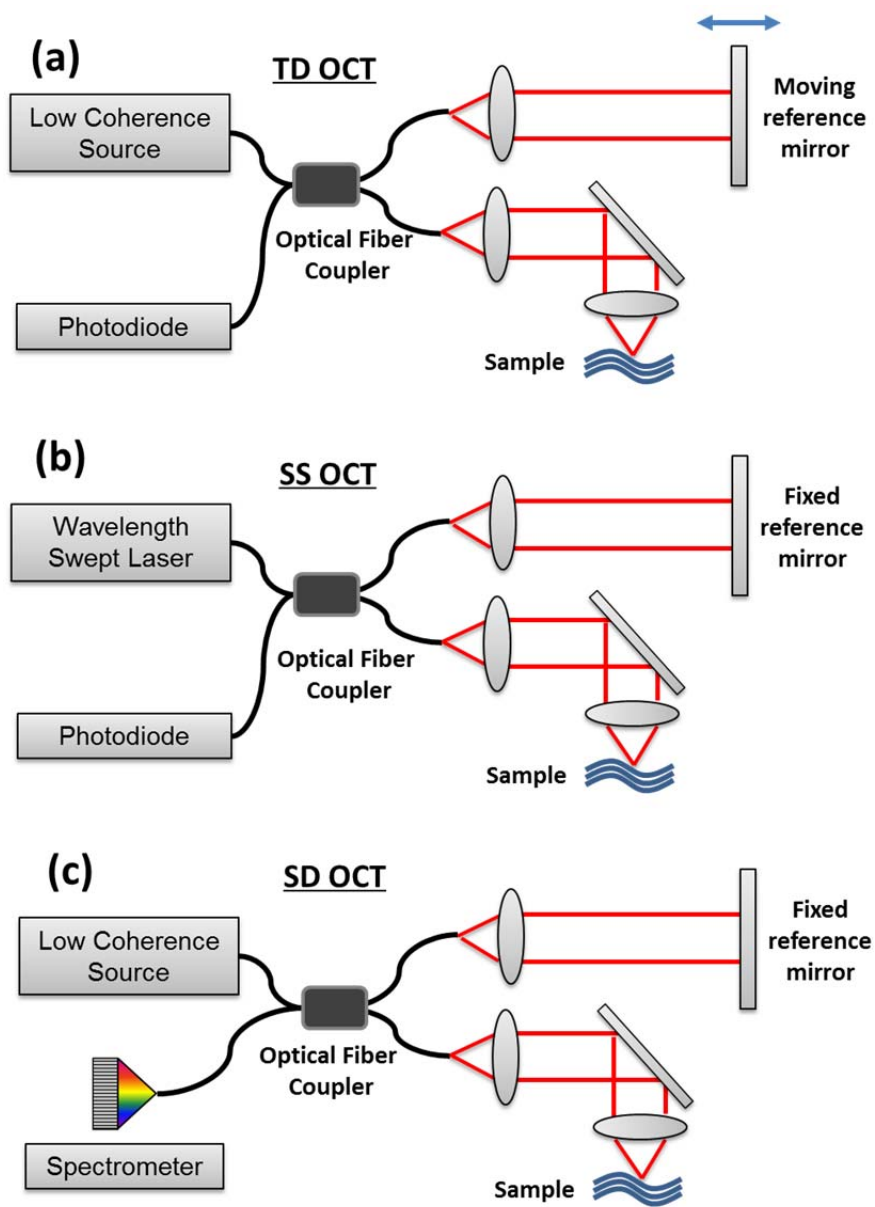


Figure 1.2 Basic schematic of different types of OCT system. (a) Time Domain OCT. (b) Swept Source OCT. (c) Spectral Domain OCT.

Both SD and SS OCT share the same principle. Light back reflected from the sample (I_S) and reference (I_R) arms are recombined at the fibre coupler and the interference between them results in modulations on the optical spectrum. The frequency of the interferogram encodes the axial location of the scatterer in the sample, with increasing frequency corresponding to larger optical path length mismatches (Δz). The axial location of the sample then can be extracted by taking the Fourier transform of

the interferogram: (Eq. 1-1). The axial resolution of an OCT system is determined by the coherence length (l_c) of the light source shown in (Eq. 1-2).

$$\mathcal{F}^{-1}\{I_{Det}\} \propto \hat{S}(z) \otimes \left\{ (I_R + I_s) \delta(z) + 2\sqrt{I_R I_s} (\delta(z + \Delta z) + \delta(z - \Delta z)) \right\}, \quad (\text{Eq. 1-1})$$

$$l_c = \frac{2 \ln 2}{\pi} \cdot \frac{\lambda_0^2}{\Delta \lambda} \approx 0.44 \cdot \frac{\lambda_0^2}{\Delta \lambda}, \quad (\text{Eq. 1-2})$$

where $\hat{S}(z)$ is the Fourier transform of the source spectrum, $\Delta \lambda$ is bandwidth of the light source and λ_0 is the center wavelength.

Compare to other volumetric medical imaging modality such as X-ray, MRI and ultrasound, OCT offers much higher resolution. Most OCT systems have resolution in the range of $1\mu\text{m}$ to $10\mu\text{m}$, and depth penetration depth in the millimeter range. Confocal microscopy usually offers higher resolution, but OCT has the advantages of being able to acquire volumetric images more rapidly and with better axial resolution. One unique property of OCT is that its lateral resolution and axial resolution are decoupled. However, most OCT systems use an imaging beam with an approximately Gaussian profile, thus the depth of focus decreases as square of the beam waist. Both increasing the lateral resolution and penetration depth are active research areas. In this thesis, adaptive optics will be incorporated into the sample arm of the OCT to reduce the optical aberrations in order to increase lateral resolution of OCT.

The acquisition rate of OCT systems is rapidly increasing since the realization of Fourier Domain detection [9]. State of the art ultra-high speed OCT using Fourier Domain Mode Locking (FDML) light source has been reported with A-scan rates at the megahertz range [10]. However due to the intensive computations needed for FDOCT system, most of the systems (clinical and research) have not been able to perform real time volumetric imaging. High speed and robust software for OCT acquisition and processing are in great demand.

1.2. Mouse retinal imaging

Small animal models of human diseases serve as a vital component in modern medical research, especially in eye-related research. Mouse models of vision robbing diseases have facilitated the understanding of the underlying biological processes, identification of potential causative genes for human disorders, and development of novel therapies. The mouse is a commonly used for preclinical vision research due to the similarity of their eyes with human eyes in retinal morphology, physiology, function, and the availability of transgenic strains that represents human diseases.

Techniques such as immunohistology provide a gold standard for studying the animal model retinas, offering exquisite resolution and variety of molecular contrast stains; but the invasiveness of the procedure limits it to a single time point and implies use of many animals. To study the time course of dynamic processes and response of single animal during treatment, non-invasive imaging provides an important alternative to histology. Additionally, non-invasive imaging can be also used as a tool for screening the effects of therapies and to assist in making a decision about the endpoint when histology should be done.

Non-invasive ophthalmic imaging modalities such as OCT have become an important tool for small animal vision research programs and has greatly accelerated numerous preclinical studies, including [11]–[20] just to name a few. OCT offers the ability to perform longitudinal *in vivo* studies which are not feasible with more invasive imaging techniques such as immunohistology. A comparison of a standard resolution FDOCT mouse retina B-scan image to DAPI stained histology is shown in Figure 1.3, all the layers in mouse retina can be clearly identified and correlate well with histology. However, to better visualize the cellular microstructure and understand the molecular processes in living small animal retinas, ultrahigh-resolution retinal imaging is desired.

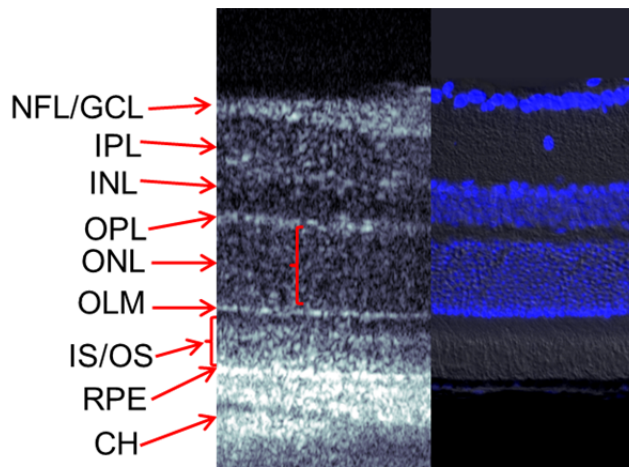


Figure 1.3 Comparison of mouse retina B-scan image (left) with histology (right). NFL, Nerve Fiber Layer; GCL, Ganglion Cell Layer; IPL, Inner Plexiform Layer; INL, Inner Nuclear Layer; OPL, Outer Plexiform Layer; ONL, Outer Nuclear Layer; ELM, External limiting membrane; IS, Inner Segment; OS, Outer Segment; RPE, Retinal Pigment Epithelium; CH, Choroid.

A summary of mouse eye anatomy compared to the human's is listed in Table 1. The mouse eye is much smaller than the human's, however, the maximum numerical aperture (NA) of a dilated mouse eye is ~ 0.5 which is almost two times larger than the human's [21], corresponding to theoretically attainable sub-micrometer resolution. The larger numerical aperture of mouse is a great advantage in ultrahigh-resolution imaging [21]. However, diffraction limited imaging performance in imaging the mouse retina is rarely achieved, *in vivo* retinal imaging of mouse retina is hampered by optical aberrations [22]. Figure 1.4 shows a mouse eye model, compared to a human eye. The mouse eye has a comparatively much larger lens and thicker retina if the to the size of human eye. Geng et al reported a detailed analysis of the effects and implications of the relatively thick mouse retina on wavefront sensing in mouse eye [21].

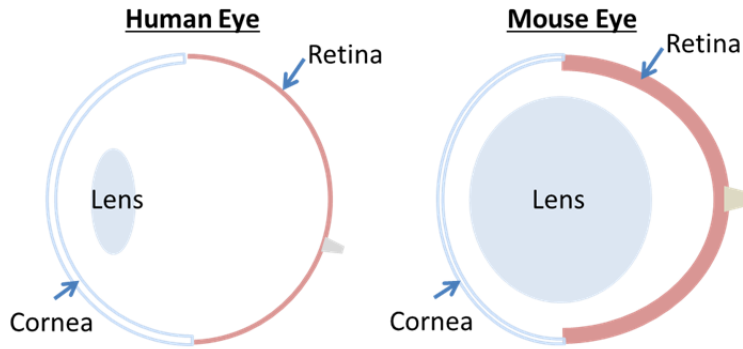


Figure 1.4 Simplified schematic of human and mouse eye model. The mouse eye model was scaled up to size of human’s for comparison.

In order to leverage the high numerical aperture of the mouse eye in retinal imaging, special systems have to be designed to accommodate the unique properties of mouse eyes and optical aberrations need to be reduced to reach diffraction limited performance. Similar to technology developed for high lateral resolution imaging in humans, adaptive optics techniques have been introduced for mouse retinal imaging. Adaptive optics is a technique where the optical aberrations in of the eye are measured and compensated. A more detailed description of adaptive optics is presented in Chapter 2.

Table 1 Comparison of the human and mouse eye optics parameters.

| | Dilated pupil Size | Focal length | Numerical aperture | Lateral Resolution* | Average retina thickness |
|-------|--------------------|--------------|--------------------|---------------------|--------------------------|
| Mouse | 2.0 mm | 2.6 mm | 0.49 | 0.65 μm | 220 μm |
| Human | 9.0 mm | 22.3 mm | 0.27 | 1.18 μm | 250 μm |

* The lateral resolution was calculated with wavelength of 860nm.

Note. Adapted from Geng et al [21], [22].

1.3. Overview of the thesis

The objective of this thesis is to design and develop a novel high speed high resolution adaptive optics optical coherence tomography imaging system for mouse retina. This thesis is organized into seven chapters including this introductory chapter. In Chapter 2, the principles of AO are discussed, major components of AO optical

system are introduced and the effect of wavefront aberrations on image quality is demonstrated. The rest of the thesis is organized as follows. First, real time video rate FDOCT acquisition and processing software is presented in Chapter 3. This software is important for real time volumetric and *en face* imaging, allowing straight forward and effortless alignment of the mouse eye and focus adjustment with real time visual feedback. The contents in Chapter 3 were published in two papers in Journal of Biomedical Optics [23], [24]. Next this software is incorporated into a lens-based adaptive optics (AO) FDOCT with a Shack-Hartmann wavefront sensor in Chapter 4. This is the first AO OCT imaging system that was specifically designed for mouse retinal imaging. The results and limitations of the wavefront sensing approach used in this system are discussed in Chapter 4 as well. In Chapter 5, the high speed processing is leveraged for wavefront sensorless adaptive optics (WSAO) OCT in order to resolve the issues associated with wavefront sensing in the mouse eye and use of a lens based AO imaging system. The WSAO OCT uses the *en face* image intensity extracted by the high speed processing software as the merit function to optimize the wavefront. Chapter 4 and 5 have been published in Biomedical Optics Express [25], [26]. In Chapter 6 this system is explored for visualization of changes in the retina in response to laser exposure. Lastly, the conclusion of this thesis work and the future work are presented in Chapter 7.

Chapter 2.

Adaptive Optics in Ophthalmic Imaging

2.1. Overview of Adaptive Optics

Adaptive optics (AO) is an established technology used to improve the performance of optical systems by dynamically sensing and compensating optical aberrations. The concept of adaptive optics was first proposed by Horace W. Babcock in 1953. Early applications of AO were concentrated in astronomy, where the performance of ground-based telescopes is ultimately limited by turbulence introduced by the earth's atmosphere. One solution to resolve this issue is to send the telescope into space; although this is effective, this solution is also very expensive. AO provides a more cost-effective alternative by dynamically compensating for the turbulence and hence increasing the resolution of large ground-based telescopes. The first functioning astronomical AO system was reported in 1991 on a 3.6m telescope.

Like many astronomical technologies, AO found its application in other branches of science. In 1997, Junzhong Liang, David R. Williams, and Donald T. Miller reported the first Adaptive Optics flood-illumination ophthalmoscope for imaging cone photoreceptors [27] and demonstrated the potential of AO in correcting ocular aberrations that hinder retinal imaging. Since then, AO was incorporated into three major types of retinal imaging modalities: flood-illumination ophthalmoscopy (fundus camera), scanning laser ophthalmoscopy (SLO), and optical coherence tomography (OCT) [28]. The use of a Shack-Hartmann wavefront sensor played an important role in the development of AO in ophthalmic imaging. Roorda et al demonstrated the first AO SLO system with a wavefront sensor [29]. The first combination of AO and OCT was reported by Miller et al with a time-domain *en face* flood-illumination OCT [30], and the first AO FDOCT was reported in the same year by Zawadzki et al [31]. Besides

providing high resolution volumetric images, AO OCT also revealed functional changes in the retina; human cone outer-segment renewal was observed using a combined transverse-scanning OCT (TSOCT) and SLO system [32].

Figure 2.1 shows a simplified schematic of a basic adaptive optics imaging system. The incident light wave enters the optical system at the telescope indicated by the black arrow. The incoming wavefront has aberrations, as illustrated by the wavy lines. These aberrations usually arise from the transmission of light through different media, such as the atmosphere or anterior chamber of the eye, and will result in decreased resolution and image contrast if uncorrected. After the telescope, the light wave is reflected by the DM to a beam splitter. Light of the wavefront sensing beacon (green lines) is directed to the wavefront sensor (WFS) by the dichroic beam splitter to measure the aberrated wavefront. With the wavefront aberration determined, the control algorithm changes the shape of the DM to be equal to the inverse of the aberrations to flatten the wavefront. In other words, the DM is deformed to match the complex conjugate of the wavefront in order to cancel the wavefront phase error. Instead of using a wavefront sensor to measure the aberrations directly, it is also possible to use some other image quality metric as the feedback to the AO control loop, and interactively search for the optimum wavefront shape that produces the highest image quality metric. Image-based adaptive optics is discussed in more detail in Chapter 5.

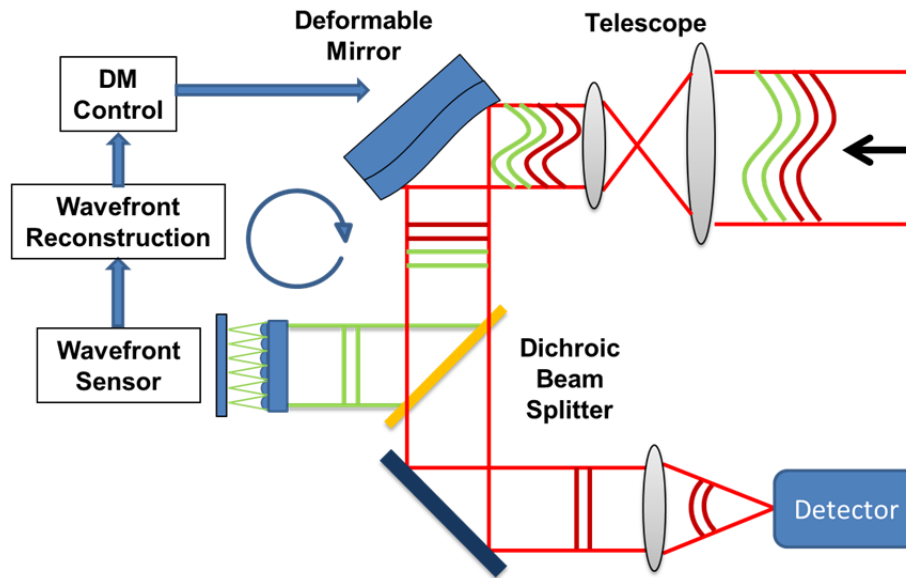


Figure 2.1 Simplified schematic of a basic adaptive optics imaging system. Black arrow indicates the direction that light originated from the sample enters the optical system. The red lines represent the light used by the imaging system, and the green lines represent a different wavelength of light that is commonly used as a beacon for wavefront sensing.

2.2. Point spread function

An optical system can be characterized by its point spread function (PSF), or impulse response, $h(x_2, y_2)$. In the case of a thin lens, where the input pupil is placed at a distance of one focal length away from the lens, $h(x_2, y_2)$ is the Fourier transform of the generalized pupil function, as shown in Eq. 2-1 [33].

$$h(x_2, y_2) = \frac{A}{\lambda f} \mathcal{F} \left\{ P(x_1, y_1) e^{-i \frac{2\pi}{\lambda} W(x_1, y_1)} \right\}, \quad (\text{Eq. 2-1})$$

where x_2, y_2 and x_1, y_1 are the spatial coordinates at the pupil plane and focal plane respectively, λ is the wavelength, f is the focal length of the lens, A is amplitude of the wave and $W(x_1, y_1)$ is the pupil phase function. For an aberration-free optical system, the pupil function should be a circular aperture that acts as a low pass filter in the frequency domain.

For OCT imaging, the sample arm can be modeled as a reflective scanning confocal microscope, where the single mode optical fiber serves as a pinhole aperture for both illumination and collection of light from the sample. A reflective scanning confocal microscope is a coherent imaging system with an effective PSF equal to the square of the PSF of the objective lens [34]. The image formation for such imaging system is,

$$I(x, y) = |h^2 \otimes r|^2, \quad (\text{Eq. 2-2})$$

where h is the point spread function and r is the sample reflectivity profile.

For an aberration-free reflective scanning confocal microscope with a circular pupil, the intensity distribution of a point reflector placed at the focal plane is

$$I_c(v) = \left(\frac{2J_1(v)}{v} \right)^4, \quad (\text{Eq. 2-3})$$

where $J_1(v)$ is a first-order Bessel function of the first kind and v is the normalized lateral range parameter defined by $v = 2\pi x NA / \lambda_0$. Here, x is the lateral distance from the optical axis, NA is the numerical aperture of the objective lens, and λ_0 is the center wavelength of the light source.

2.3. Wavefront aberration

In an ideal optical imaging system, the resolving power is ultimately limited by diffraction. However, practical optical systems are affected by optical aberrations, mainly system and sample induced aberrations that further reduce the resolution. System-induced aberrations arise from imperfect imaging optics. The primary objective in the design of imaging systems is to minimize these system aberrations. For example, in microscopy, multi-element objective lenses are used to reduce both monochromatic and chromatic aberrations. In the field of retinal imaging, several strategies to reduce the system aberrations have also been reported, including non-planar folding of the off-axis spherical mirror, the use of a toroidal mirror, or lens-based design [35]–[38]. In

contrast to system-induced aberrations, sample-induced aberrations occur when light propagates through a medium such as atmosphere or biological tissues and can be static or vary in time. The benefit of AO is to correct for the dynamic sample-induced aberrations that cannot be compensated with static optical designs.

To describe the wavefront aberration, it is convenient to decompose the pupil phase function $W(x,y)$ into a set of orthogonal Zernike polynomials. That is

$$W(x, y) = \sum_{j=0}^{j_{\max}} W_j Z_j(x, y) , \quad (\text{Eq. 2-4})$$

where $Z_j(x,y)$ and W_j are the Zernike polynomials and their corresponding coefficients. Appendix 1 provides the full polynomial equation (up to 5th order) listed by both single and double index scheme.

To demonstrate the effect of wavefront aberrations on the overall image quality, we simulated retinal images with and without wavefront aberrations present. The mouse photoreceptor mosaic was synthesized, as shown in Figure 2.2. The wavefront were reconstructed from published aberration data measured in mice eyes [21]. No other sources of errors were considered in this simulation.

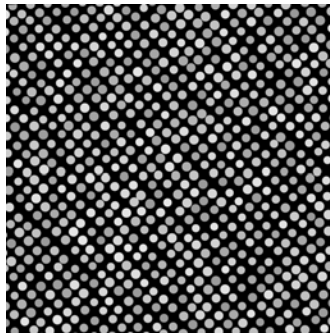


Figure 2.2 Synthetic mouse photoreceptor mosaic.

The simulation of diffraction-limited (aberration-free) images with a NA of 0.5 and 0.25 are shown in Figure 2.3 (a) and (c) respectively. Typical high order wavefront aberrations in the mouse eye were added in the pupil phase function $W(x, y)$ and the aberrated images were simulated shown in Figure 2.3 (b) and (d). Compare to the

diffraction limited images, the aberrated images have lower contrast and image brightness that demonstrated the need for adaptive optics.

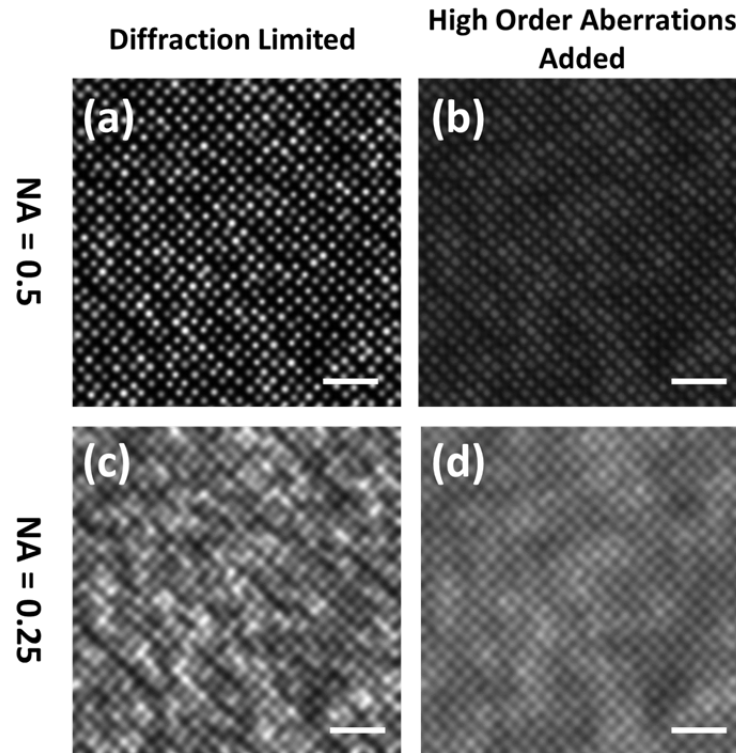


Figure 2.3 Simulated retinal images of mouse photoreceptors mosaic under different imaging conditions.

2.4. Wavefront Corrector

At the heart of an AO system is the wavefront corrector. A wavefront corrector cancels out the phase error of the wavefront that affects the imaging resolution by changing the optical path over the wavefront propagates. There are primarily two categories of wavefront correctors: transmissive liquid crystals spatial light modulators (SLM) that change the refractive index; and deformable mirrors (DM) that alter the physical shape of the reflective surface. DMs can be further classified based on their surface continuity or driving method. Each type of wavefront corrector has its balance of advantages and disadvantages. The choice of wavefront corrector depends on needs for specific imaging system such as the nature of the aberrations being corrected, the amount of correction and level of accuracy required.

In this thesis, we chose to use commercially available segmented MEMS (micro-electro-mechanical-systems) DM from Iris AO Inc (Berkeley, CA). A close-up picture of the Iris AO DM is shown in Figure 2.4. The Iris AO DM has 111 actuators and 37 gold-coated piston-tip-tilt segments with 5μ stroke and $700\mu\text{m}$ pitch. This DM provides a fill factor greater than 98% and minimizes the diffraction effects that are usually present in a segmented DM. Each segment is made flat, and the whole DM can be flattened with an RMS error smaller than 20nm. In addition, the Iris AO DM offers precise linear open-loop piston-tip-tilt positioning with essentially no hysteresis and can be controlled via Zernike mode operation (discussed below). The mechanical response of the DM is under $200\mu\text{s}$.

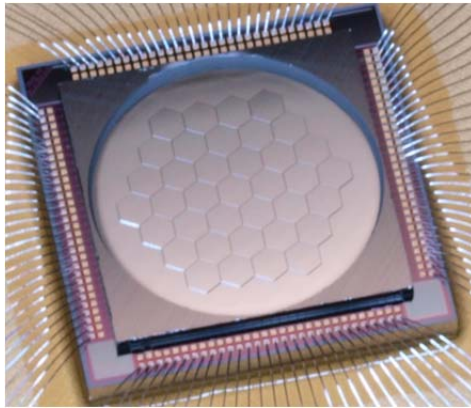


Figure 2.4 Picture of Iris AO PT-111 DM. Reprinted with Iris AO's permission.

2.5. Wavefront sensor

The wavefront sensor (WFS) is used to measure the optical aberrations. Wavefront sensing is an important component of the adaptive optics system. Different types of wavefront sensors have been developed, such as spatially-resolved refractometers, the laser ray tracing technique, and the Hartmann plate test. Ocular aberrations are usually measured by the Shack-Hartmann wavefront sensor [39].

2.5.1. The principle of Shack-Hartmann wavefront sensor

The Shack-Hartmann wavefront sensor is an optical system invented in 1971, derived from the Hartmann method [40]. It is being used in an increasing number of

applications, including the measurement of the human eye aberrations, the evaluation of laser beam quality, and the quantification of aero-optical effects. Shack-Hartmann wavefront sensors consist of a micro lens array and a 2D area detector. The micro lens array is a two-dimensional array consisting of miniature lenses (called lenslets) that all have the same diameter and focal length. Typical lenslets diameters range from about 100 to 600 μm and typical focal lengths range from a few millimeters to about 30 mm. The shape of the lenslets and aperture can differ depending on the application. The lenslet array is placed in front of the detector, at a distance equals to the focal length of the lenslets.

The micro lens array is optically conjugated with the pupil plane to sample the aberrated wavefront. The micro lens array splits the incoming light into a number of small beams, each of which is focused onto the detector. The displacement of the focused spot from each lenslet is proportional to the local slope of the wavefront. In the case of no aberrations, the wavefront that emerges from the pupil is planar, thus the wavefront sensor spots are formed along the optical axis of each lenslet as demonstrated in Figure 2.5 (a). In contrast, when aberrations are present, the individual spots are displaced from the optical axis of each lenslet, as showed in Figure 2.5 (b). The location of each spot with respect to the reference position needs to be determined in order to measure the local slope of the wavefront, and reconstruct the pupil phase function.

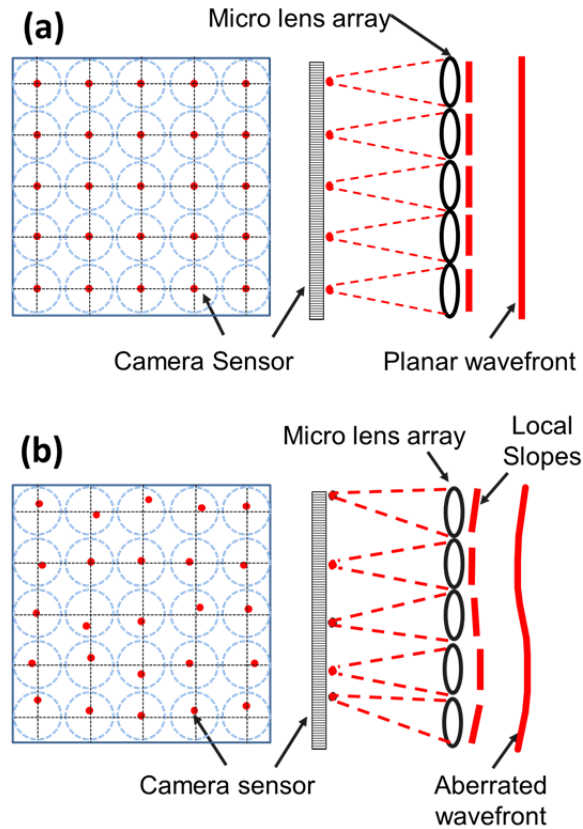


Figure 2.5 Principle of operation of a Shack-Hartmann wavefront sensor. The wavefront spot patterns produced by a planar wavefront (a) and by an arbitrarily aberrated wavefront (b). The blue dotted circles represent lenslets.

2.5.2. Centroiding

The most common way to determine the displaced position of each wavefront sensor spot is to use a centroid (center-of-mass) algorithm. Simple centroid calculation works well when the spots have a Gaussian distribution with Poisson noise. More advanced algorithms, such as weighted centroid and matched filtering, have been developed to increase the detection accuracy [41]. In this thesis work, the wavefront sensor used a simple centroid algorithm which measures the first moment of the focal-plane intensity distribution for each subaperture. That is, the displaced position of the spot, $(\Delta x, \Delta y)$, is calculated using

$$\Delta x = \frac{\sum_{i,j \in AOI} x_{i,j} I_{ij}}{\sum_{i,j \in AOI} I_{ij}} \text{ and } \Delta y = \frac{\sum_{i,j \in AOI} y_{i,j} I_{ij}}{\sum_{i,j \in AOI} I_{ij}}. \quad (\text{Eq. 2-5})$$

2.5.3. Wavefront Reconstruction

The local tilt (slope) of the wavefront within each subaperture can be estimated using the displacement of the focused spot and the focal length of the lenslets as shown in (Eq. 2-6).

$$\begin{aligned} \frac{\partial W(x, y)}{\partial x} &= \frac{\Delta x}{f} \\ \frac{\partial W(x, y)}{\partial y} &= \frac{\Delta y}{f} \end{aligned} \quad (\text{Eq. 2-6})$$

There are a number of different methods for reconstructing the wavefront from the slope measurements. Two of the more commonly used methods are zonal (direct numerical integration) and modal (polynomial fitting) [42]. In this thesis, the Iris AO DM used modal wavefront reconstruction due to the segmented nature of the mirror and the ease of the modal control algorithm. In the modal reconstruction method, the wavefront surface is described in terms of a set of Zernike polynomials. Since the Zernike polynomials are continuous and analytic through the first derivative, the wavefront gradient may be obtained by differentiating Eq. 2-4 as follows [43]

$$\begin{aligned} \frac{\partial W(x, y)}{\partial x} &= \sum_j W_j \frac{\partial Z_j(x, y)}{\partial x} \\ \frac{\partial W(x, y)}{\partial y} &= \sum_j W_j \frac{\partial Z_j(x, y)}{\partial y} \end{aligned} \quad (\text{Eq. 2-7})$$

These equations provide an analytic description of the wavefront slope at the center of every lenslet. By comparing these analytic wavefront slopes with the measured gradient values, an appropriate set of coefficients W_j can be obtained. Least-Squares fitting is usually the method used to calculate these coefficients.

$$\begin{aligned}\beta &= \alpha\omega \\ \omega_{LS} &= (\alpha^T \alpha)^{-1} \alpha^T \beta,\end{aligned}\tag{Eq. 2-8}$$

where β is a vector of measured wavefront slopes, α contains the average gradients of the basis functions (Zernike polynomials) in each subaperture, and ω is a vector of Zernike coefficients to be determined.

2.6. Summary

This chapter presented an overview of adaptive optics. Incorporation of AO with OCT for *in vivo* imaging applications requires rapid display and visualization. In the next chapter, we will describe GPU acceleration of OCT acquisition and processing that allows real time visualization of volumetric OCT images. This high speed processing platform is an essential component of this research and will be used in the rest of the thesis with AOOCT for mouse imaging.

Chapter 3.

Graphics processing unit accelerated optical coherence tomography processing at megahertz axial scan rate and high resolution video rate volumetric rendering

3.1. Introduction

Optical coherence tomography (OCT) is an essential diagnostic tool in ophthalmic clinics and is expanding its range of applications rapidly due to its ability to acquire high resolution cross-sectional images non-invasively [44]. The acquisition speed of OCT has increased tremendously since it was first demonstrated in 1991, going from 400 Hz to 20 MHz line rates for tissue imaging [44]. Commercially available swept sources are able to provide 400 kHz axial scan rate with relatively minor modifications (dual channel, double buffer) [45]. Multi-megahertz FDML-based Swept Source (SS) OCT systems capable of acquiring high-resolution volumes at video-rate have been demonstrated [10], and 1.6MHz systems have been presented that are used for clinical retinal imaging [46]. Spectral domain (SD) OCT systems operating in the 800nm wavelength range have been presented operating with an axial scan rate of 500 kHz with a dual camera configuration [47].

As the ultrahigh-speed OCT acquisition has continuously been extended, there followed an increasing demand for real-time volumetric visualization of OCT data to explore the full potential of the technology, such as intraoperative OCT [48] and functional OCT [49], [50]. However, due to the complexity of OCT data processing and extremely high data throughput, processing interferometric fringe data into images requires significant computational resources, and to date has been far slower than the acquisition rate. Although ultrahigh-speed OCT is capable of acquiring volumetric data

in real-time, nearly all of the OCT systems render the 3D images in post-processing which greatly limits the range of applications. Several attempts have been made to accelerate the OCT data processing and volume rendering utilizing GPUs and FPGA, including [50]–[57] just to name a few. A GPU based approach for volume rendering was presented at a reduced volume size at 5 fps [55], but high resolution, video rate; real-time volumetric rendering has not yet been realized.

Specialized extensions, such as visualization of blood flow, have been developed to enable functional imaging of biological tissues [9]. In addition to traditional Doppler OCT imaging, which is sensitive to flow rate [58], techniques have recently been proposed that highlight tissue in motion, but are insensitive to rate; these include speckle variance OCT (svOCT) [59], phase variance OCT (pvOCT) [60], and optical microangiography [61]. Predominantly, the flow contrast work has been performed in post processing. A few notable exceptions have been presented in literature [50], [62], where real-time flow contrast was demonstrated during acquisition in two dimensions as well as in three dimensions. For effective volume acquisition of flow contrast data, real-time visualizations of capillary networks via en face projections of vasculature are highly desirable.

In this chapter, we discuss strategies to hide the latency of memory transfer, and describe a custom CUDA program for real time OCT structural data processing and volume rendering. We present data processing and display of high resolution volumes at video rate. In addition, we present GPU-accelerated processing for real-time svOCT with cross-sectional (B-scan) and *en face* displays of flow contrast in the retina. Depth resolved vasculature network in both mouse and human retina were visualized.

3.2. Methods

To exploit the massive parallel computational power of the GPU, we used NVIDIA's (Santa Clara, California) parallel programming platform, CUDA (Computer Unified Device Architecture) version 4.2 which offers easy integration and implementation of general purpose computation with GPUs, and OpenGL [63] as our display library. CUDA Visual Profiler was used in our project to record the timing and

calculate the processing speed. Microsoft Visual Studio 2008 was used to build and compile the project. We tested our software on three generations of NVIDIA's low cost consumer grade GPUs (GTX 460 1GB RAM, GTX 560 1GB RAM, and GTX 680 2GB RAM) to investigate their performance and scalability. Each GPU was hosted in a desktop computer with Intel Core i7 CPU running Windows 7 operating system. The only upgrade to the computer was to use a workstation level motherboard that provides sufficient PCIe bandwidth for throughput of the data between the acquisition boards and the GPU.

The OCT images presented in this report were acquired by two custom OCT systems. The SS-OCT system used an AlazarTech (Pointe-Claire, QC, Canada) digitizer and a 100 kHz Axsun (Billerica, MA) wavelength swept laser. This system was used for real-time acquisition and display of human retinal data. The SD-OCT system utilized a high-speed CMOS line scan camera detector (Sprint spL4096-140k, Basler AG, Germany) and superluminescent diode source centered at 860nm with a 135nm FWHM bandwidth (Superlum Inc., Moscow). The maximum line rate attainable to support this bandwidth was 125 kHz. Since we do not have a megahertz line rate OCT system, to evaluate the processing performance we loaded interferometric data from a file into an intermediate buffer in the host RAM, and then transferred the whole volume to another buffer also in the host RAM to represent the acquisition of real-time data from a frame grabber or analog-to-digital converter (ADC). We verified experimentally that the memory transfer speed from host to host in our computer is about 5.1GB/s, thereafter we were able to simulate a specific OCT acquisition speed by adding delays during to the memory transfer. For example, by adding a 5ms delay to a volume (1024*256*200 pixel) transfer, we were able to simulate a 2MHz OCT acquisition.

The limiting factor in the previously reported GPU implementation of OCT data processing was the overhead in memory transfer between the CPU (host) RAM and GPU (device) off-chip global memory. Facing the constraint of the limited PCI Express (PCIe) bus bandwidth, our strategy was to parallelize the data transfer from host to device with processing kernels to hide memory transfer latency, and eliminate the need of transferring the data back to the CPU side (host) by rendering the processed volume and B-scans directly on the GPU. This method itself gives 3x speed boost compared to our previous work [51] since the processing kernel calls take almost the same time as

the memory transfer on the PCIe bus. The concurrent memory transfer from host to device and data processing on GPU was designed using two CUDA streams that are executed concurrently and synchronized after each processing iteration: one to transfer the data from host to device, and one to process the raw OCT data on the GPU memory. The unprocessed raw data was transferred to the GPU as a batch of frames instead of as a single frame to fully utilize the PCIe bandwidth and the copy engine of the GPU. While one batch of raw data was being transferred to the GPU by the transfer stream, the previous batch of frames that was already in the GPU memory was simultaneously being processed by the kernel stream. Note that in Figure 3.1, the memory copy function that was used to transfer data from host to device is asynchronous; it will return immediately without waiting for the completion of the memory transfer and will not block the execution of the processing kernels. In order to fulfill the restriction of concurrent memory transfer and kernel execution, the raw data was stored in the page-locked memory in the host. In addition, transferring data from the page-locked host memory to the device allows the utilization of the full PCIe bandwidth (6.2GB/s in GTX 680, and 5.7GB/s in GTX 460 and 560, compared to ~3GB/s in non-page-locked host memory) [52]. To further reduce the memory transfer overhead, we transfer the interferometric fringe data to the GPU as 16bit integers, and then cast the data to floating point format (float) on the GPU in a parallel manner.

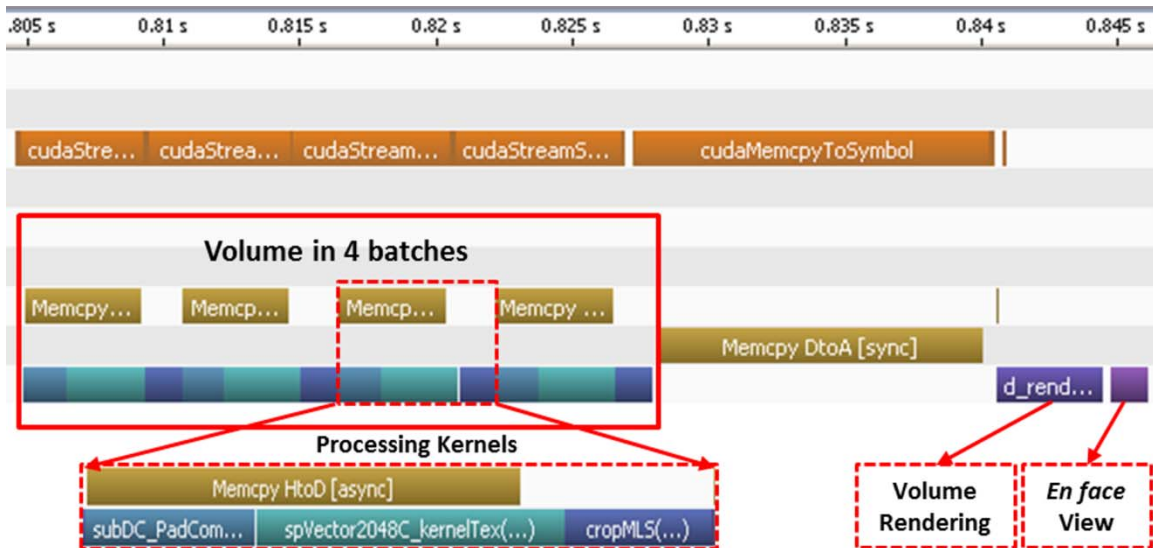


Figure 3.1 CUDA Profiler Timeline for SS-OCT processing and volume rendering pipeline. Memcpy HtoD [async] is transferring the raw data, subDC_PadCom is a kernel with the function of type conversion, DC subtraction and zero padding. spVector2048C_kernelTex is a kernel called by the cuFFT library which performs the FFT. CropMLS performs the modulus and Log. Memcpy DtoA [sync] copy the processed OCT data into CUDA 3D Array for volume rendering.

Figure 3.2 shows a flow chart of the OCT data processing pipeline used in our method. The full OCT processing pipeline was optimized for SD-OCT, but some processing blocks were dropped from the SS-OCT pipeline in exchange for an increase in processing speed. For example, since in SS-OCT the interferometric data can be sampled linearly in wavenumber, the lambda to wavenumber resampling part of the pipeline can be dropped. Similarly, for 1310nm and 1060nm imaging systems, the dispersion can usually be compensated physically, whereas the processing blocks for numerical dispersion compensation are typically needed for SD-OCT systems in the 800nm range.

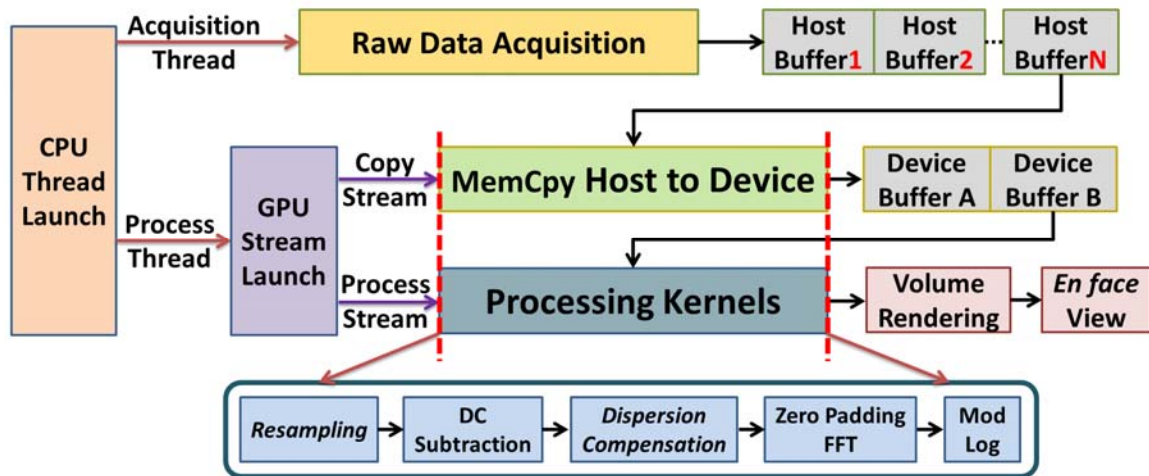


Figure 3.2 Flow chart for OCT acquisition and GPU processing. The italicized procedure names in the Processing Kernels represent the blocks that were dropped for the SS OCT implementation.

3.3. Results and Discussion

A screen capture of the CUDA profiler timeline for SS-OCT processing at the maximum line rate is shown in Figure 3.1 to demonstrate the detailed timing of our program. The timing for one complete SS-OCT volume processing and rendering iteration is shown in Figure 3.1. Every acquired volume (256x200 A-scans) was divided into four batches for transfer and processing in the GPU. The profiler output in Figure 3.1 indicates that the memory transfer and OCT processing kernel were overlapped. Once the whole OCT volume was processed, the processed data was transferred to another device buffer and assembled into a 3D CUDA array in preparation for the volume rendering. As a final step, the volume rendering and *en face* view were executed. The complete pipeline required ~43ms, corresponding to a volume processing and rendering rate of ~23 volumes/s.

As shown in Figure 3.1, an *en face* view and a volume rendering were also performed on the GPU following the volume processing. To render the processed OCT B-scan, *en face* view, and 3D volume directly from the GPU global memory as 32bit floating point texture (which avoids type conversion and transferring data back to the host), the CUDA resource allocated for holding the processed data was registered to OpenGL using CUDA/OpenGL interoperability functions. The *en face* projection of the

volume was generated by the summing up all the pixels in each A-scan using an optimized parallel reduction algorithm [64]. A ray casting method was used to render the processed OCT volume [65]. Compared to other implementations reported in the literature, our method requires only one GPU to process and render the OCT volume which would lower the cost and more importantly reduce the data transfer across the PCIe bus.

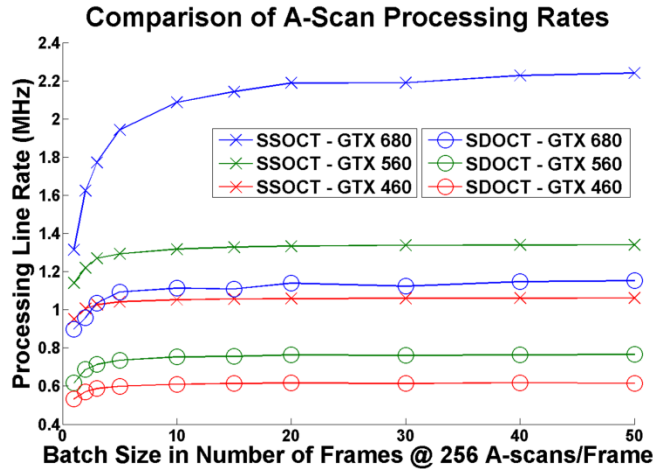


Figure 3.3 OCT A-Scan batch processing rate. For SSOCT, processing pipeline includes DC subtraction, FFT, modulus and Log. For SDOCT, processing pipeline includes linear interpolation, DC subtraction, dispersion compensation, FFT, modulus and Log.

In order to further optimize the processing and memory transfer speed of the GPU, the batch processing size was investigated. Figure 3.3 shows the plot of batch size versus axial scan line rate in our implementation (including time for memory transfer and displaying the B-scan frame). The processing rate plateaued around ~ 3840 A-scans per batch. Our GPU accelerated processing achieved an A-scan (16bit 2048 pixels) rate of >2.24 MHz, and volume (size: $1024 \times 256 \times 200$) rendering at >23 volumes per second. At the current PCIe data transfer rates from host to device (using PCIe 2.0 x16), this upper limit will be at a line rate of ~ 3.1 MHz (16bit 1024 pixels/line). Figure 3.4a and Video 1 [23] present screen captures of images processed and rendered using our GPU accelerated with SS-OCT for human retina. For this video, the raw data was loaded from a file with delays added to simulate an acquisition line rate of 1.2 MHz, as described above. To demonstrate the real-time acquisition and display capability, we performed an *in vivo* real-time SS-OCT imaging for human retina and human anterior

chamber in the Eye Care Center at Vancouver General Hospital with a line rate of 100 kHz that was limited by our source (Figure 3.4b and Figure 3.5). The displayed B-scans were averaged (4 adjacent frames) and a bilateral filter was applied (both steps implemented on the GPU).

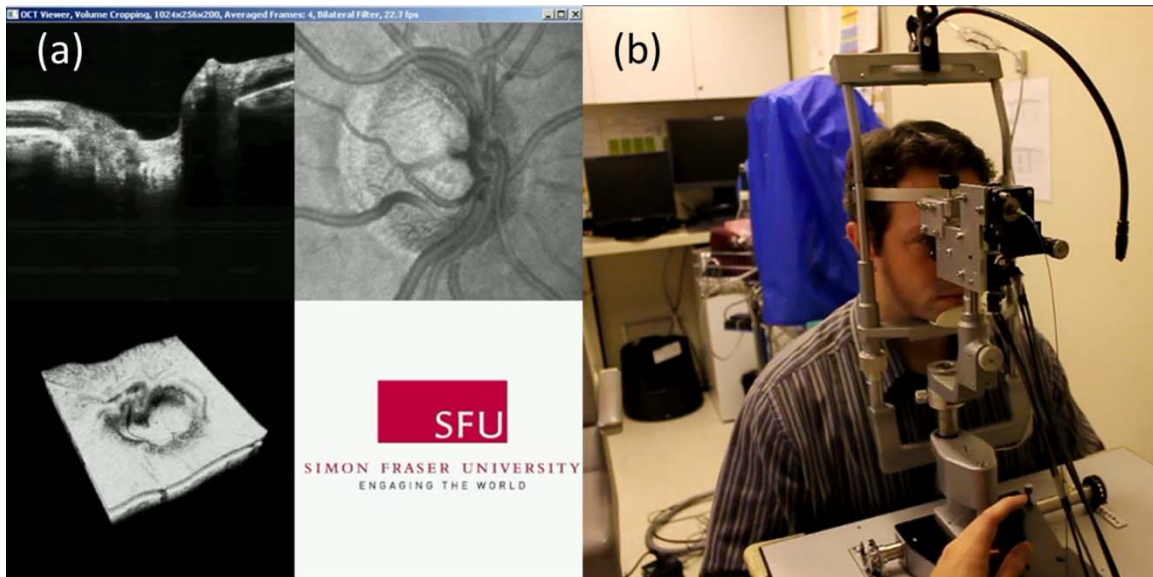


Figure 3.4 (a) Screen captures of OCT images (Video 1). Upper left: OCT B-scan. Upper right: *En face* view. Lower left: 3D volumetric rendering. (b) Real time acquisition and processing of human retinal images (Video 2 [23], QuickTime, 3.33MB).



Figure 3.5 Screen captures of OCT Anterior Chamber Imaging session.

For SD-OCT, the complete processing pipeline with wavenumber resampling and numerical dispersion compensation was implemented. Instead of developing a custom kernel to calculate the interpolation, we utilized GPU texture as a hard-wired linear

interpolation method [66], which also gives an extra benefit of implicitly casting integer data into floating point. Although linear interpolation offered the fastest processing speed, it produced lower quality images. We implemented a fast cubic spline interpolation that provided a balance between the image quality and processing speed [67]. With the additional computational load required for SD-OCT data, we demonstrated volume processing at an A-scan rate of 1.1 MHz using linear interpolation and 1 MHz with fast cubic interpolation. This is well in excess of the fastest SD-OCT acquisition system reported [47], leaving GPU resources available to implement more advanced image processing.

With the computation power afforded by our GPU accelerated OCT processing software, we were able to visualize vasculature network using speckle variance OCT. For svOCT, 3 B-scans were acquired at the same location, a speckle variance kernel is launched after the processing of the OCT structural data, which computed the variance of the speckle intensity [68]. An *en face* projection image was then extracted from the user selected region for visualizing the svOCT data. For the target application of retinal imaging in both human and mouse, the program extracts flow contrast data from up to three user-selected depth regions, processes an *en face* projection for each region, and combines all three projections into a composite R/G/B color-coded *en face* projection. A notch filter, single-pixel rigid registration and Gaussian filter were implemented on the GPU to reduce motion artifact and enhance the image quality of the svOCT.

The representative images in Figure 3.6 were acquired over an area of $1 \times 1 \text{ mm}^2$ in a mouse retina with an acquisition time of $\sim 1.5 \text{ s}$. Speckle variance OCT *en face* images were generated within the user selected region using maximum intensity projection. In Figure 3.6(a), 2(b), and (c), the regions of interest selected were NFL, IPL, and OPL respectively, and these three svOCT *en face* images were made into a composite R/G/B images shown in Figure 3.6 (e). Comparison of the structural *en face* (Figure 3.6 (d)) with the composite svOCT *en face* (Figure 3.6 (e)) images reveals a significant contrast improvement for blood vessels with svOCT; the static retinal structures such as nerve fibres are not visible in the svOCT *en face* projections.

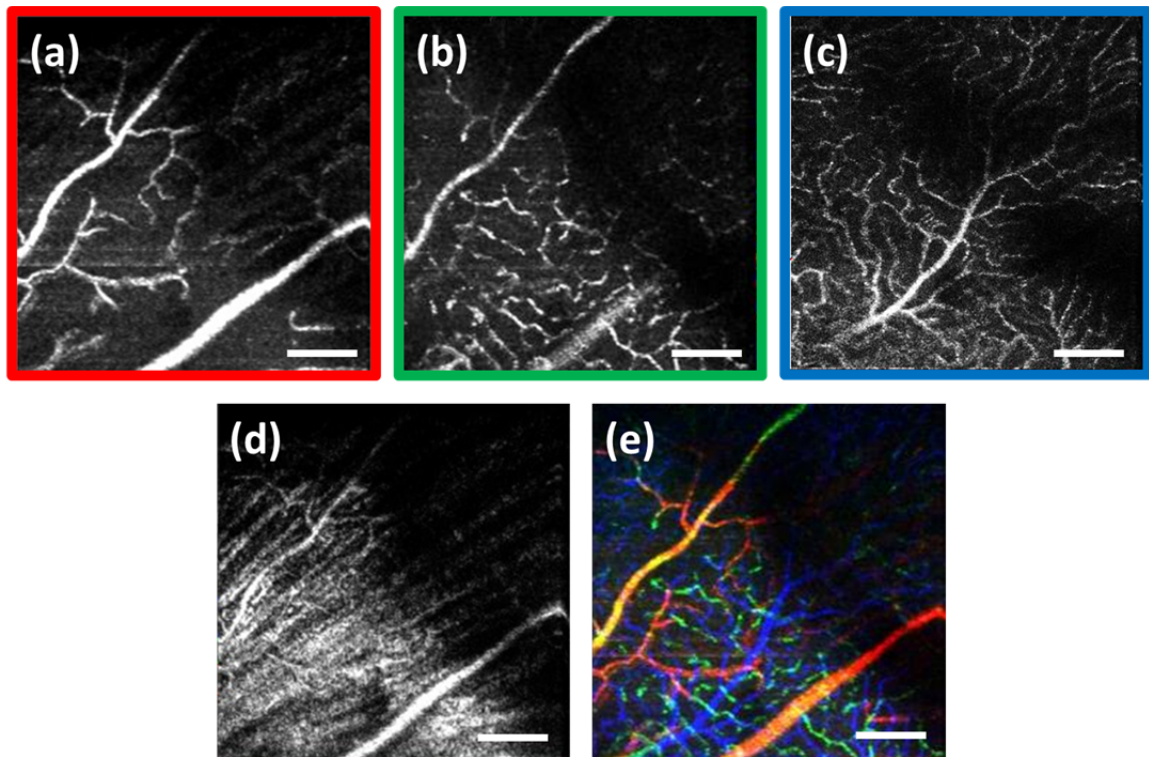


Figure 3.6 The svOCT images are presented in (a), (b) and (c). Color-coded R/G/B composite of (a), (b) and (c), where each color represents: NFL - blue, IPL - green, and OPL - red is shown in (e). The combined intensity *en face* image of all depth regions of interest is presented in (d). Scale bar: 200 μm .

Representative svOCT images of retina acquired on healthy human volunteers with custom built 1060nm SS OCT system are presented in Figure 3.7. The svOCT *en face* images show well-defined capillary networks around the fovea region in the retina with depth encoded via color-coding.

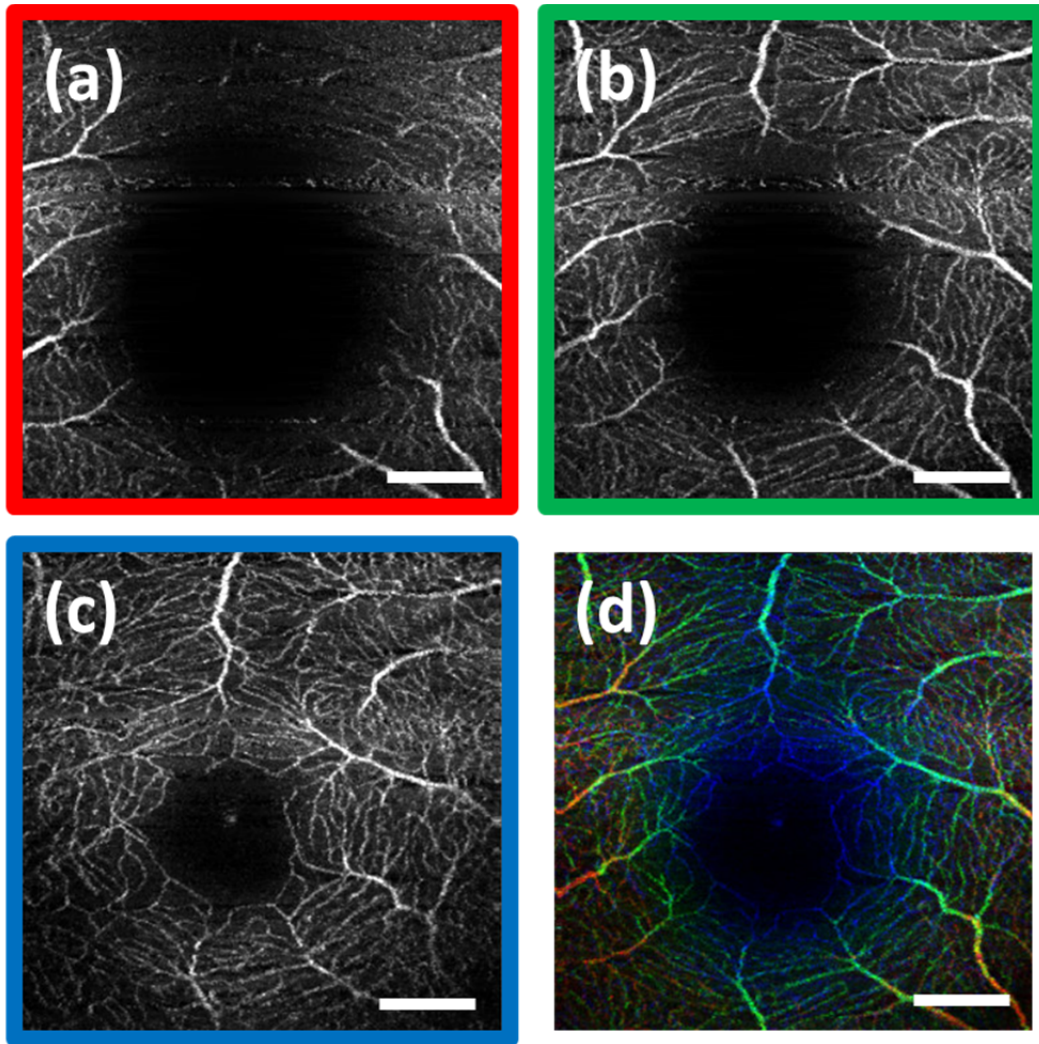


Figure 3.7 Comparison between the intensity en face images (a, c, e, g) and the color-coded composite svOCT *en face* images (b, d, f, h), respectively. Images (a–d) were acquired at the optic nerve head region, and images (e–h) were acquired in the macula. Scale bar: 400 μm .

3.4. Summary

In conclusion, we have demonstrated sustained A-scan processing rates of 2.24 MHz for SS-OCT, and 1MHz for SD-OCT using a commercial grade GPU and desktop computer. Our program is able to process and render the volumetric OCT data at ~23 volumes/s (volume size: 1024*256*200). We have also demonstrated real time speckle variance OCT with clear visualization of depth resolved vasculature network in both

human and mouse retina. Real-time, video rate, volumetric visualization of OCT data has exciting applications in diagnostic and surgical applications. The GPU implementation is low cost, and can be easily integrated with existing acquisition systems. The source code for transferring interferometric data from the host to the GPU, and for processing to the point of display is available at <http://BORG.ensc.sfu.ca/fdoct-gpu-code.html>. The GPU accelerated OCT acquisition and processing software described here is essential and will be used in the rest of the thesis work.

Chapter 4.

Adaptive optics optical coherence tomography for in vivo mouse retinal imaging

4.1. Introduction

Small animal models of human diseases serve as a vital component in modern vision research. Rodents, such as mice and rats, are commonly used in the development of novel therapeutics against diseases causing blindness. To better visualize the cellular microstructure and understand the molecular processes in the living retina, high resolution retinal imaging of rodent eyes is desirable. Techniques such as immunohistology provide a gold standard for studying the animal model retinas with exquisite resolution and a variety of molecular contrast stains, but the invasiveness of the procedure limits it to a single time point and implies the use of many animals. In order to study dynamic processes and the response of a single animal during treatment, non-invasive imaging provides an exciting alternative to histology.

Generally for *in vivo* ocular imaging, obtaining cellular level resolution requires imaging through a large eye pupil and implementation of adaptive optics (AO). AO allows correction of the aberrations caused by refractive surfaces of the eye, allowing diffraction limited lateral resolution [27], [29], [31], [69]–[75]. Visualization of the photoreceptor mosaic has been demonstrated in humans using AO in combination with fundus photography, Optical Coherence Tomography, and Confocal Scanning Laser Ophthalmoscopy [28]. Previous studies have shown that for young healthy volunteers with excellent vision, the cone mosaics could be resolved down to 2° eccentricity from the fovea without Adaptive Optics (AO) using a modest eye pupil size (below 3-4mm) [76]. However the cone packing density closer to the fovea, or rod photoreceptor

packing, is much higher, so a large pupil size and AO correction are required to increase the resolution and allow visualization of these structures.

Compared to the human eye, the mouse eye is about 8x smaller, but its numerical aperture (NA) is more than 2x larger [22]. The effects of optical aberrations on image quality increase as the NA increases, and this hampers *in vivo* high resolution imaging in mice [21], [77]–[79]. Attempts have been made to compensate for the aberrations in order to achieve cellular resolution imaging of living mouse retina by using adaptive optics; Biss et al. demonstrated an AO biomicroscope and Alt et al. demonstrated an AO SLO for *in vivo* imaging of mouse retina, showing that AO correction of monochromatic aberrations increased the brightness and resolution of the images [80]–[82]. However, their results also reported the difficulties of wavefront sensing in mice which might arise from the small eye artifacts. Geng et al. demonstrated the appearance of a double spot in the Hartmann-Shack Wavefront Sensor (WFS) when a small diameter wavefront beacon resulting in a long depth of focus was incident on the mouse retina, versus a single spot when focusing on a retinal vessel [21]. The latest work from Geng et al. showed encouraging results for AO confocal Scanning Laser Ophthalmoscope (cSLO) where the photoreceptor mosaic was visualized for the first time in mouse retina *in vivo* [83].

Compared to cSLO, which is an *en face* imaging modality, OCT has the advantage of being able to acquire micrometer-resolution cross-sectional images of retina structure [11], [17], [18], [84], [85]. This unique property of OCT has enabled longitudinal studies with rodents where high precision retinal thickness measurements and detailed visualization of volumetric morphological changes are required [13], [14], [86], [87]. In addition to the structural information obtained from OCT, its functional extensions such as Doppler OCT [88]–[90], and flow contrast OCT [60], [68], [91], [92], can be used to visualize the vascular network.

The perceived quality of OCT images is largely affected by the focal spot size, scanning length, sampling density, and the OCT B-scan averaging techniques that affect the size and contrast of the speckle (coherent noise). What is very often perceived as improved quality of averaged clinical OCT images is achieved by blurring of the speckle pattern, and consequently reducing the lateral resolution by a factor of three or more.

The goal of this chapter is to investigate methods to improve the lateral resolution for mouse retina imaging with OCT. In our approach, we incorporated an external objective lens in combination with a refraction canceling fundus lens in order to reduce the aberrations in the mouse eye and to facilitate the imaging procedure. Using this technique, we were able to reduce the size of the speckle by increasing the Numerical Aperture (NA) during *in vivo* mouse retinal imaging. To ensure that the improvement in the spot size (lateral resolution) was not offset by spot blurring created by the increased aberrations, we incorporated an off-the-shelf commercially available adaptive optics system into the mouse retina OCT imaging instrument. This allowed for monitoring and correction of the refractive errors and therefore improvement in the focused spot size. Increasing the NA in OCT reduces the speckle size which in turn reduces the need for averaging and blurring of the images, thereby maximizing the resolution of the images at a given NA.

Generally, when implementing AO-OCT for high NA (relative to what is normally used in the OCT technique) retinal imaging there are two main challenges. The first challenge, and the one we address in this report, focuses on increasing the NA of the imaging instrument and our ability to properly measure and correct aberrations in this scenario. As a result, increased lateral resolution and decreased speckle size can be observed. Second, after successful implementation of AO-OCT for high NA imaging, methods to extend the depth of focus of the AO-OCT system while maintaining high lateral resolution can be explored; however, this is beyond the scope of this report.

4.2. Methods

A custom Adaptive Optics (AO) FD-OCT system built at Simon Fraser University was used for mouse retinal imaging. The details of each sub-system are described below.

4.2.1. FD-OCT Engine

A semi-custom FD-OCT engine was used in this research. The light source was a 135nm bandwidth superluminescent diode centered at 860nm from Superlum Inc.

(Moscow, Russia), corresponding to a coherence length in air of $2.4\mu\text{m}$. The spectrometer was integrated with a Basler sprint camera and was built by Biotigen Inc. (Durham, NC). The resolution of the spectrometer is 0.066nm/pixel . The real-time acquisitions of rodent retina volumes consisted of $2048 \times 500 \times 500$ pixels (axial points x number of A-scans/ B-scan x number of B-scans/ volume). We operated the OCT engine at 60 B-scan/s to match the integration time of the wavefront sensor. The corresponding line rate was 33 kHz (accounting for galvo fly-back time). During rodent retinal imaging the power at the cornea was $750\mu\text{W}$, which is below the ANSI limits of maximum permissible exposure at this wavelength for humans [93]. Data acquisition was performed using a custom written program with a Graphics Processing Unit (GPU) processing [23], [51], for real time simultaneous display of B-scans and *en face* view. Final data processing for measurement and presentation was performed using Matlab (Mathworks, Natick MA).

4.2.2. Wavefont sensor

Wavefront sensing was performed using the same light as for the FD-OCT. A Pellicle Beam Splitter (PBS) was placed immediately after the collimating lens to redirect 8% of the light backscattered from the sample to a Hartman-Shack Wavefront Sensor (WFS). The IrisAO Inc. (Berkeley, CA) WFS has 19mm focal length lenslets arranged in a hexagonal pattern in a one-to-one correspondence with the mirror elements on the Deformable Mirror (DM). The DM has 111 (PTT111) actuators connected to 37 hexagonal mirror elements (three actuators per segment) with $5\mu\text{m}$ stroke (piston/tip/tilt) [74]. The wavefront sensing centroiding algorithm and AO control program were provided by Iris AO, Inc. and allowed closed-loop aberration correction at 60Hz.

4.2.3. Adaptive Optics FD-OCT

A schematic of the small animal refractive AO FD-OCT system is presented in Figure 4.1. The sample arm consisted of lens based optics (achromatic lenses from Thorlabs. Inc, Newton,NJ). In order to prevent back-reflections from the lens surfaces entering the WFS, the lenses were tilted with respect to the optical axis while monitoring the wavefront sensor; the tilt angle was less than ~ 3 degrees. Light from the fiber was collimated and directed through a beam expander to the DM. A second set of

telescopes was used to relay the pupil to the galvanometer scanning mirrors. A final telescope relayed the pupil to an achromatic objective lens with focal length of 25mm.

The beam waist ($1/e^2$ radius) at the objective lens was 3.5mm, corresponding to an imaging NA of 0.14. The beam radius was estimated to be ~ 0.5 mm at a distance corresponding to the mouse pupil, which has a maximum dilated radius of ~ 1 mm. The estimated focal width (Gaussian waist $1/e^2$) was $1.96\mu\text{m}$ in air and had a corresponding depth of focus of $28\mu\text{m}$. The system aberrations, measured using a paper scattering phantom placed at the focus, were about 67nm RMS without AO correction at a scanning angle of 1 degree, which is close to the diffraction limited performance of $\lambda/14$. With the AO correction activated, the measured RMS for the phantom went down to 20nm. The Zernike coefficients of the system aberrations are presented in Figure 4.4(a).

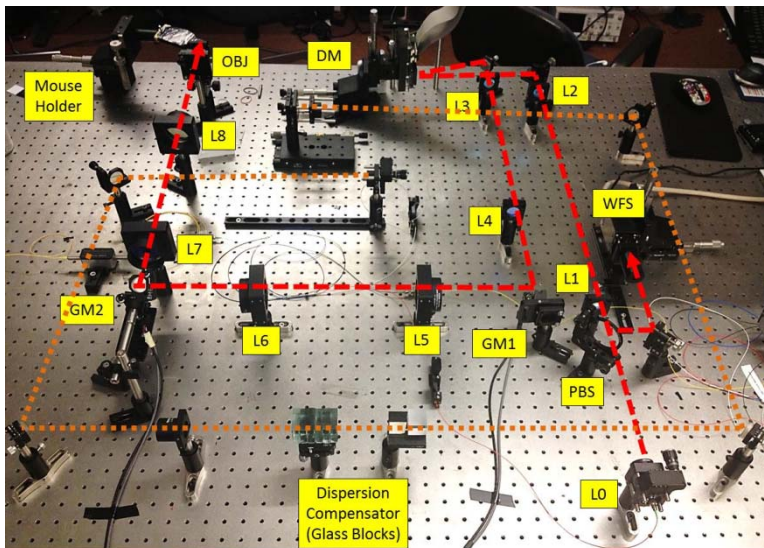
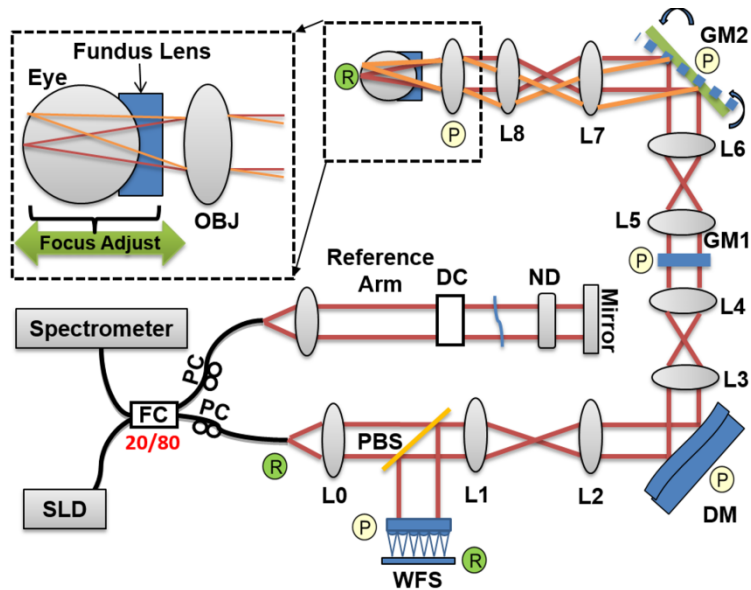


Figure 4.1 (Top) Schematic of the small animal AO FDOCT system. (Bottom) Photograph of optical layout. DC - dispersion compensation; DM - deformable mirror; FC-20/80 fiber coupler, 20% of the light from SLD goes to sample arm, 80% goes to reference arm; GM1, GM2 - horizontal and vertical galvo scanning mirrors; FL - fundus lens; PC - polarization controller. PBS - pellicle beam splitter; SLD, superluminescent diode; WFS, wavefront sensor; L - achromatic lenses: L0: ($f=16\text{mm}$); L1, L2: ($f=300\text{mm}$); L3, L4: ($f=200\text{mm}$); L5, L6: ($f=150\text{mm}$); L7, ($f=100\text{mm}$) L8: ($f=200\text{mm}$); OBJ - objective: ($f=25\text{mm}$); ND, neutral density filter; P represents the location of the planes conjugated to the pupil throughout the system; R represents the retinal conjugate planes. Inset: the mouse and fundus lens combination can be translated to adjust the focus. GM1 is slow scan mirror and is presented unfolded for clarity. Note that the schematic is drawn for illustrative purposes only; it does not reflect the actual physical dimensions or the optical configuration of the system.

For mouse imaging, a plano-concave lens (2mm fundus lens, AR coated, Volk Optical Inc. Mentor, OH) matching the radius of curvature of the mouse eye was placed immediately after the final objective lens. Figure 4.2 shows a representative schematic of the fundus lens and an OCT B-scan of the mouse anterior chamber and fundus lens combination acquired *in vivo* by focusing the beam on the cornea, and adjusting the reference arm path length accordingly.

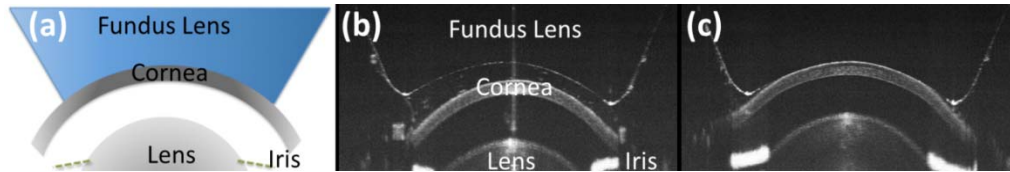


Figure 4.2 (a) Schematic of the fundus lens positioned at the mouse cornea. (b) OCT image of a fundus lens near the cornea. (c) OCT image of a fundus lens in contact with the cornea.

The refraction cancelling fundus lens provided multiple benefits: it reduced lower order aberrations at the highly curved front corneal surface, it reduced back-reflection from the cornea seen by the wavefront sensor, and it helped maintain corneal hydration during imaging by protecting the tear film. Furthermore, the concave surface of the fundus lens provided a point of contact for the small animal, bringing the mouse eye to the correct location for imaging. Additionally, since the corneal refraction is cancelled by the fundus lens, this allows us to use an objective lens with arbitrarily chosen focal length. By using a longer focal length objective, a smaller stroke in the deformable mirror is needed for the same amount of focal shift at the focal plane. This is especially important for designs utilizing small stroke deformable mirrors, such as the one used in this report.

4.2.4. Mouse Handling

Mice of strain C57BL/6J (pigmented) were obtained from Jackson Laboratories (Bar Harbor, ME) and Charles River (Wilmington, MA). All mouse imaging experiments were performed under protocols compliant to the Canadian Council on Animal Care, and with the approval of the University Animal Care Committee at Simon Fraser University. The mice were anesthetized (ketamine, xylazine, and acepromazine mixture (50:5:1 mg/kg body weight) injected intraperitoneally) and their pupils were dilated using a

topical solution (atropine sulphate 1%) prior to imaging. Some motion was evident, however, due to animal respiration as observed during image acquisition. During imaging, the anesthetized mouse was placed in an adjustable holder with 5 degrees of freedom that offered translation and rotation, allowing the mouse eye positioned for acquisition of images from different retinal eccentricities. In order to maintain corneal hydration, generous amounts of artificial tear gel (Novartis Tear-Gel, 10g tube) were applied, and held in place with the fundus lens.

4.3. Results

With the anesthetized mouse placed with the eye aligned at the fundus lens, modest focus adjustment was performed by axial translation of the mouse and fundus lens combination relative to the fixed objective lens (see inset in Figure 4.1). Since the FD-OCT and the WFS used the same light source, the effects to the WFS spots could be monitored as the location of the focal plane on the mouse retina was adjusted by looking at B-scan. Representative images from the WFS camera are presented in Figure 4.3 with the DM held in a “flat” position as characterized by the DM manufacturer. The data in Figure 4.3 (a) was acquired when the focus was not optimized; the entire retinal thickness was observed to be generally bright in the B-scan, and the wavefront spots were large. Closer inspection revealed two peaks in the wavefront spots, similar to results reported in the literature [21]. The WFS data in Figure 4.3 (b) was acquired after adjusting the position of the focus on the outer retina. In the magnified view, the WFS spots are seen to be more circular, and contain only a single peak which is important for centroid detection and the adaptive optics aberration correction algorithm. In the corresponding simultaneously acquired B-scan, the intensity of the outer retina layers is higher than the inner retinal layers when compared to Figure 4.3 (a).

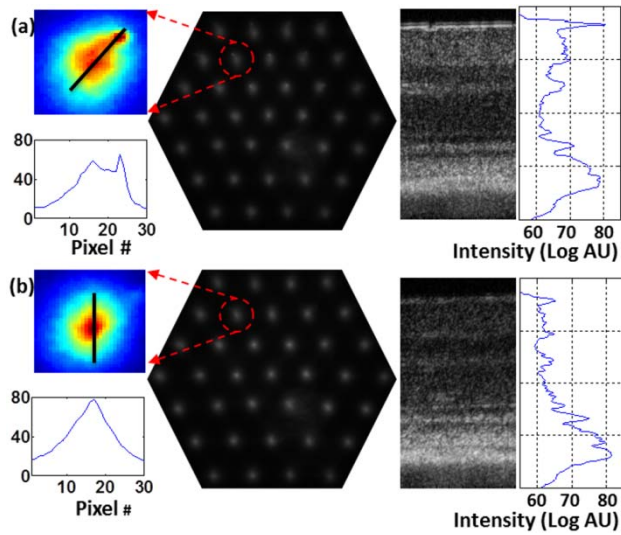


Figure 4.3 Images from the wavefront sensor camera and corresponding log scale B-scans acquired simultaneously at the same location. A single wavefront sensor spot (in the red dotted circles) are shown at higher magnification in the heat maps, and the corresponding intensity profiles were taken at the position of the black line. (a) WFS image with non-optimized focus. (b) WFS images acquired with the beam focus optimized on the outer retinal layers.

Figure 4.4 (b-d) shows representative measurements of the Zernike coefficients and RMS error recorded by our wavefront sensor before and after the AO correction during mouse imaging. Before engaging the AO correction, the mouse eye was aligned along the optical axis and the focus was set to the outer retina. The RMS error before AO correction was measured to be in the range of $0.2\mu\text{m} - 0.6\mu\text{m}$, and was dominated by defocus and astigmatism. After the AO correction was activated during animal imaging, the RMS wavefront error was reduced to about 50nm . The AO system performance for a sample of 8 mice (right eye only) is presented by plotting the averaged magnitude (mean \pm standard deviation) for each of the Zernike coefficients before and after correction in Figure 4.4 (e).

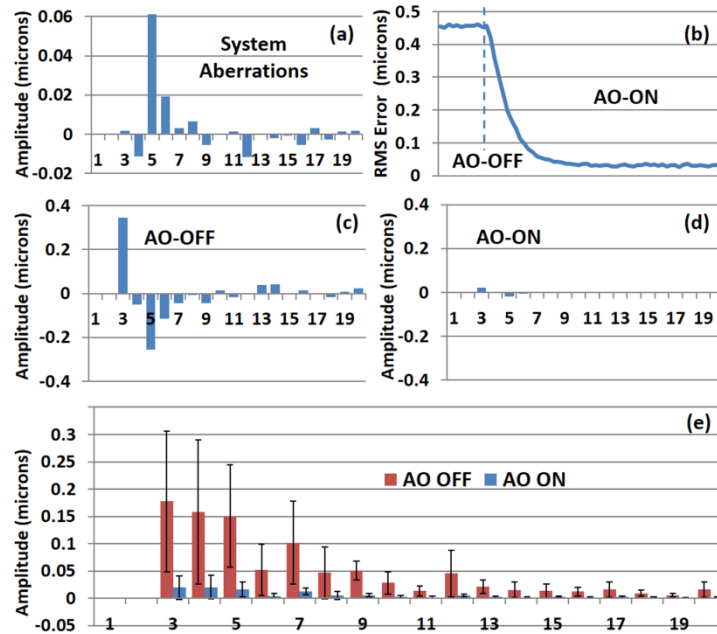


Figure 4.4 (a) Measurement of the system residual aberrations with a paper phantom in the retinal plane. (b) A representative trace of the RMS wavefront error during mouse imaging. The corresponding Zernike coefficients measured before (c) and during (d) AO correction while imaging a mouse retina with the AO FD-OCT. Note that the scale of vertical axis in (a) is 10 times smaller than that of (c) and (d). (e) Averaged magnitude of Zernike coefficients and standard deviation before and after correction as measured for sample of 8 mice. The Zernike coefficients follows the OSA standard for reporting the optical aberrations of eyes.

Representative images of mouse retina with a custom built standard resolution FD-OCT system and images from our AO FD-OCT system with a similar light source (axial resolution) are presented in Figure 4.5. The optical system of the standard lateral resolution rodent FD-OCT system used to acquire these images is described elsewhere [11], [14]. Briefly, the system had Gaussian waist ($1/e^2$) $\sim 6.5\mu\text{m}$, and a depth of focus of $\sim 308\mu\text{m}$ (which is long enough to contain the full thickness of the mouse retina). The standard resolution FD-OCT images were acquired and processed with the same custom written software as the images acquired with the AO FD-OCT system presented in this report. The standard resolution B-scan in Figure 4.5 was acquired with a 1.5mm lateral scan length. Note that all the major retinal layers can be identified in the images and all the retinal layers appear to be bright. The inset shown in the yellow dotted box was acquired with the AO FD-OCT system from a mouse of the same strain as the one used for imaging with the standard resolution FD-OCT system. In the inset, the AO FD-

OCT beam is focused on the outer retinal layers which are brighter than the inner retinal layers, if compared to the standard resolution FD-OCT image. As expected the speckle size observed in the AO FD-OCT image is significantly smaller than that of the standard resolution FD-OCT image, enhancing the visibility of the retinal layers.

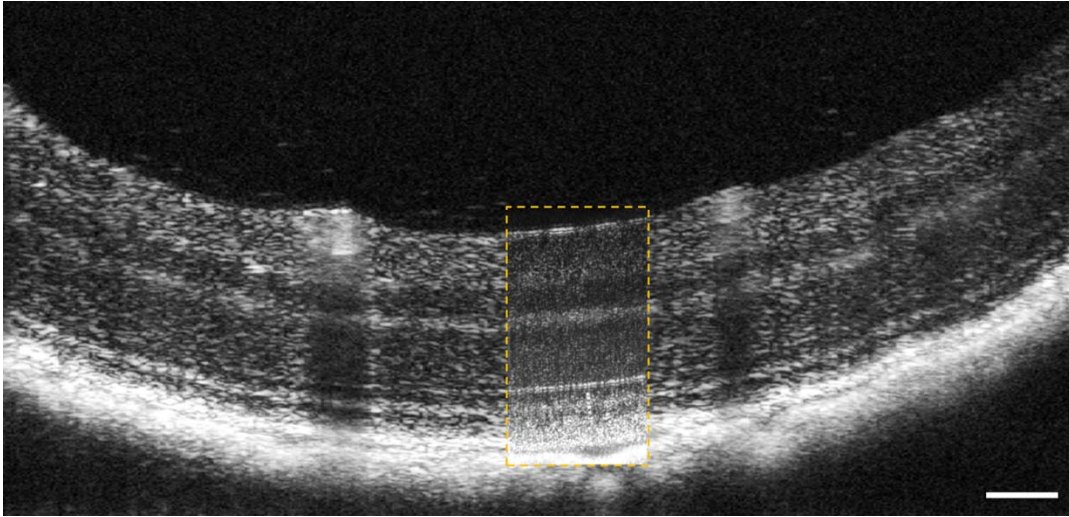


Figure 4.5 A comparison of regular rodent OCT B-scan with high resolution AO-OCT B-scan (inside yellow dotted box acquired with AO-ON). Both images were acquired from C57BL/6J (pigmented) mouse, and were generated by averaging 20 motion corrected B-scans. A logarithmic intensity scale was used for both sets of data. Note the smaller speckle size seen on AO FD-OCT inset. Scale bar: 100 μ m.

To visualize the effects that the AO system has on the B-scans, we acquired several sets of data at the same retinal location with AO system OFF and ON and displayed the results using linear intensity scale. Figure 4.6 (a) shows an image with the AO system OFF (flat DM) with the focus of the objective lens set on the outer retina. Figure 4.6 (b) shows a B-scan acquired with AO-ON and focused at the outer retina, and Figure 4.6 (c) shows a B-scan with the focus at the inner retina. With the AO correction activated (AO-ON), the B-scan is brighter as demonstrated on the right panels of Figure 4.6; as an example, with the AO activated and focused at the outer retina, the measured intensity of the OLM increased by a factor $\sim 3x$ as can be observed in panels (a) and (b). The effect of the focus shift can be observed by the change of the intensity of corresponding retinal layers in Figure 4.6 (b) and (c).

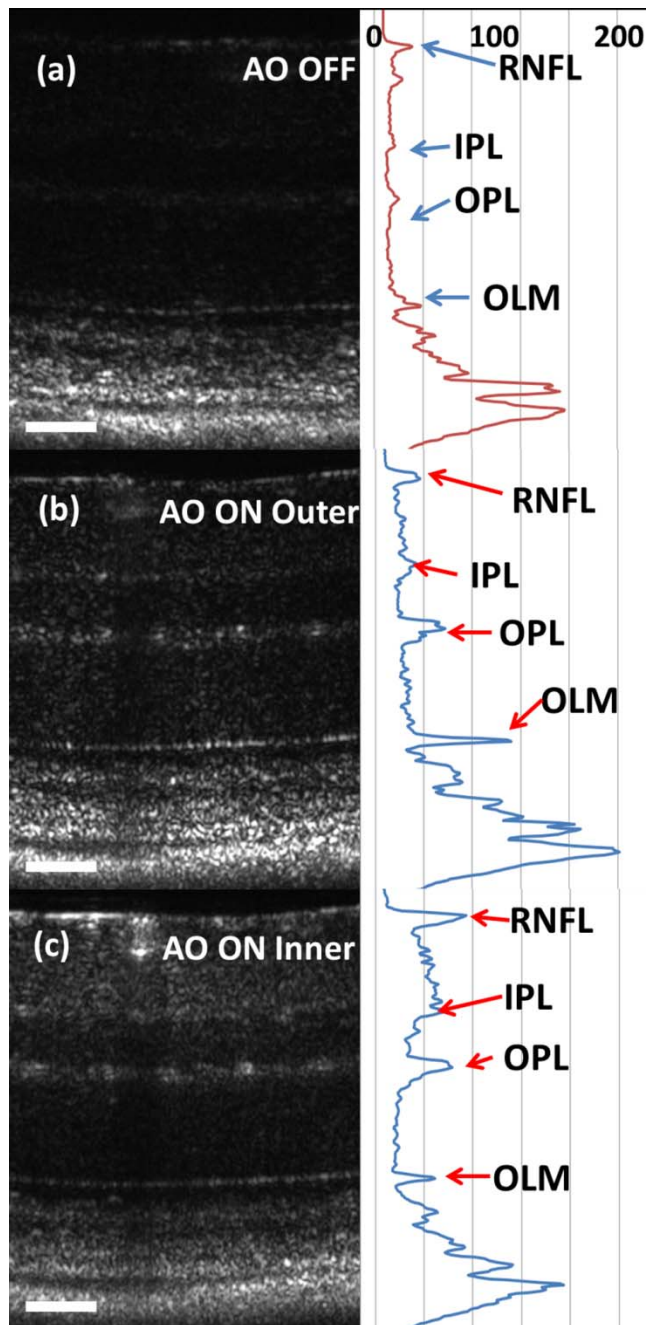


Figure 4.6 *In vivo* OCT B-scans images. (left) acquired at the same eccentricity from the retinas of C57BL/6J (pigmented) mice and depth intensity profiles (right); (a) was acquired when AO is turned off (DM flat) (b) was acquired when AO was activated and focus set on the outer retina, (c) was acquired when AO was activated and shifting the focus through the AO software to the inner retina. Images (a, b, and c) were generated by averaging 20 B-scans and are presented on a linear intensity scale. Scale bar: 50 μ m.

After activating the adaptive optics, the focal plane position could be adjusted by changing the defocus in the AO control software. The change in the location of the focal plane in the B-scan image of the mouse retina could be observed in real time as a significant increase in the brightness of the layers at the focus. *En face* images of the mouse retina were extracted from AO FD-OCT volumes acquired by raster scanning the beam across the retina, with vertically stacked B-scan frames separated by $0.6\mu\text{m}$. Representative images of the Retinal Nerve Fiber Layer (RNFL), Inner Plexiform Layer (IPL), and Outer Plexiform Layer (OPL) are presented in Figure 4.7. The axial depths indicated by the brackets in the cross sectional images represent the layers (RNFL, IPL, and OPL) that were in focus and the range of pixels that were summed up to create the *en face* images. Four sets of volumetric data were acquired at the same location, post-processed with identical parameters (same DC spectrum and same dispersion compensation values), and presented on the same linear intensity scale. The image data in the yellow dotted boxes were averaged along the short axis to generate the intensity plots on the right (the blue line represents AO-ON, and the red line represents AO-OFF). Note the improvement in the sharpness and brightness of the nerve fibers in RNFL and the capillaries in IPL and OPL in Figure 4.7 with the AO activated. With the AO-OFF, only the OPL (Figure 4.7 (f)) had sufficient contrast to enable comparison to the corresponding AO-ON image (Figure 4.7(c)), where a 2~3x increase in the intensity of the capillaries can be observed from the line graph in the right column.

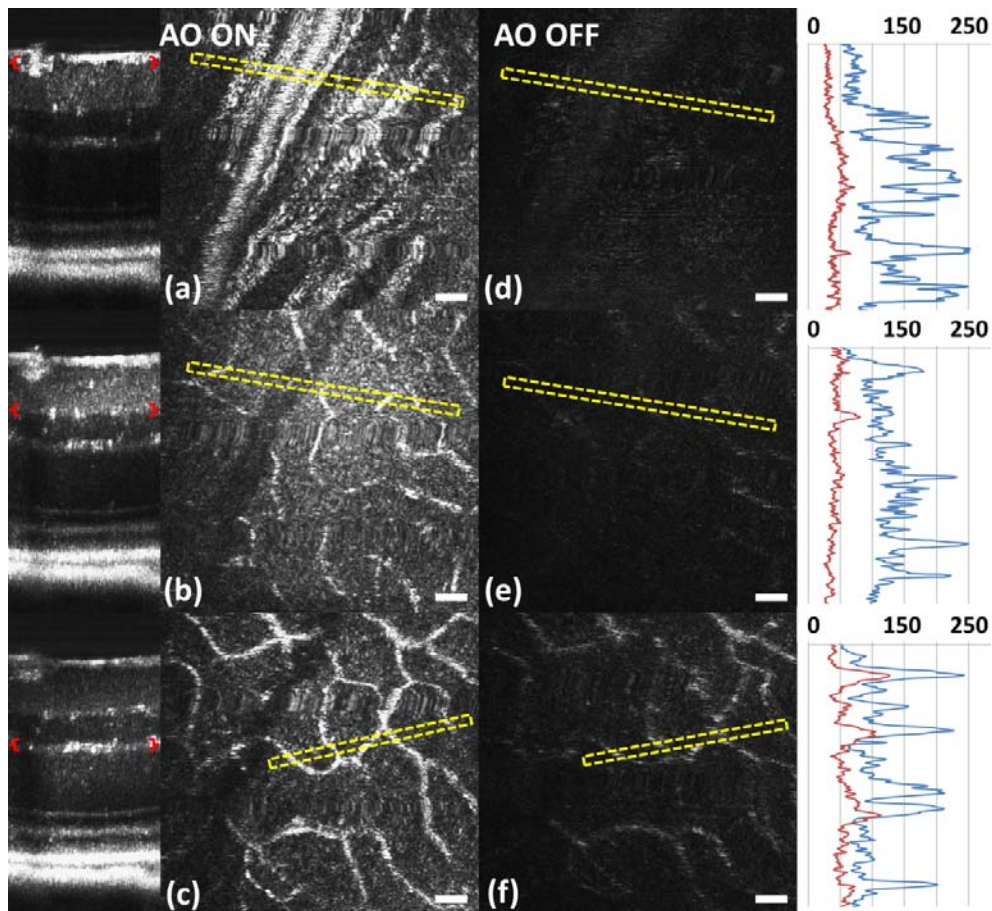


Figure 4.7 Cross sectional images of the mouse retina acquired *in vivo* with the AO FD-OCT system. The focal plane was set on the inner retina by changing the defocus in the AO control software. The axial depths indicated by the brackets in the B-scan represent the locations of (a-c) *en face* projections of different retinal layers with AO-ON and (d-f) *en face* projections at the same location with AO-OFF (DM flat). Scale bar: 30 μ m.

Figure 4.8 shows example images of the retina from a different animal than shown in Figure 4.7. Here we visualized different capillary plexus layers and the photoreceptor layer (PRL). Note the improvement in both intensity and resolution (improved width of retinal capillaries) seen on the images. The green boxes in Figure 4.8 (c) and (g) represent the locations where the widths of several capillaries of different sizes were measured with AO ON and OFF. The corresponding line graphs were normalized and are presented in panel (1), (2) and (3) at the bottom of Figure 4.8. On average, the diameter of capillaries measured with the AO-ON was $\sim 2.5x$ narrower than with the AO-OFF.

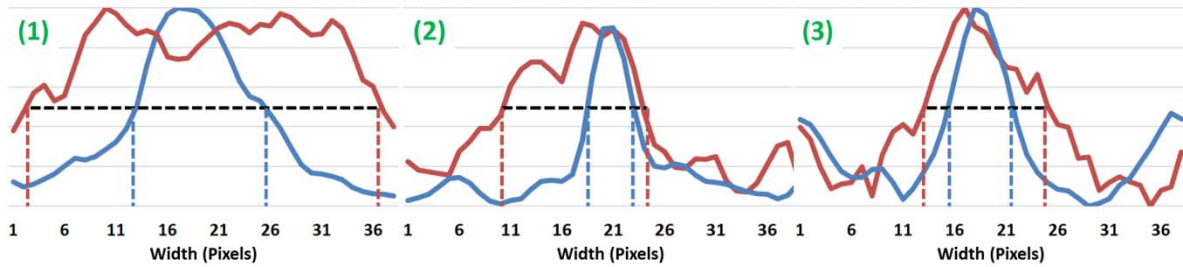
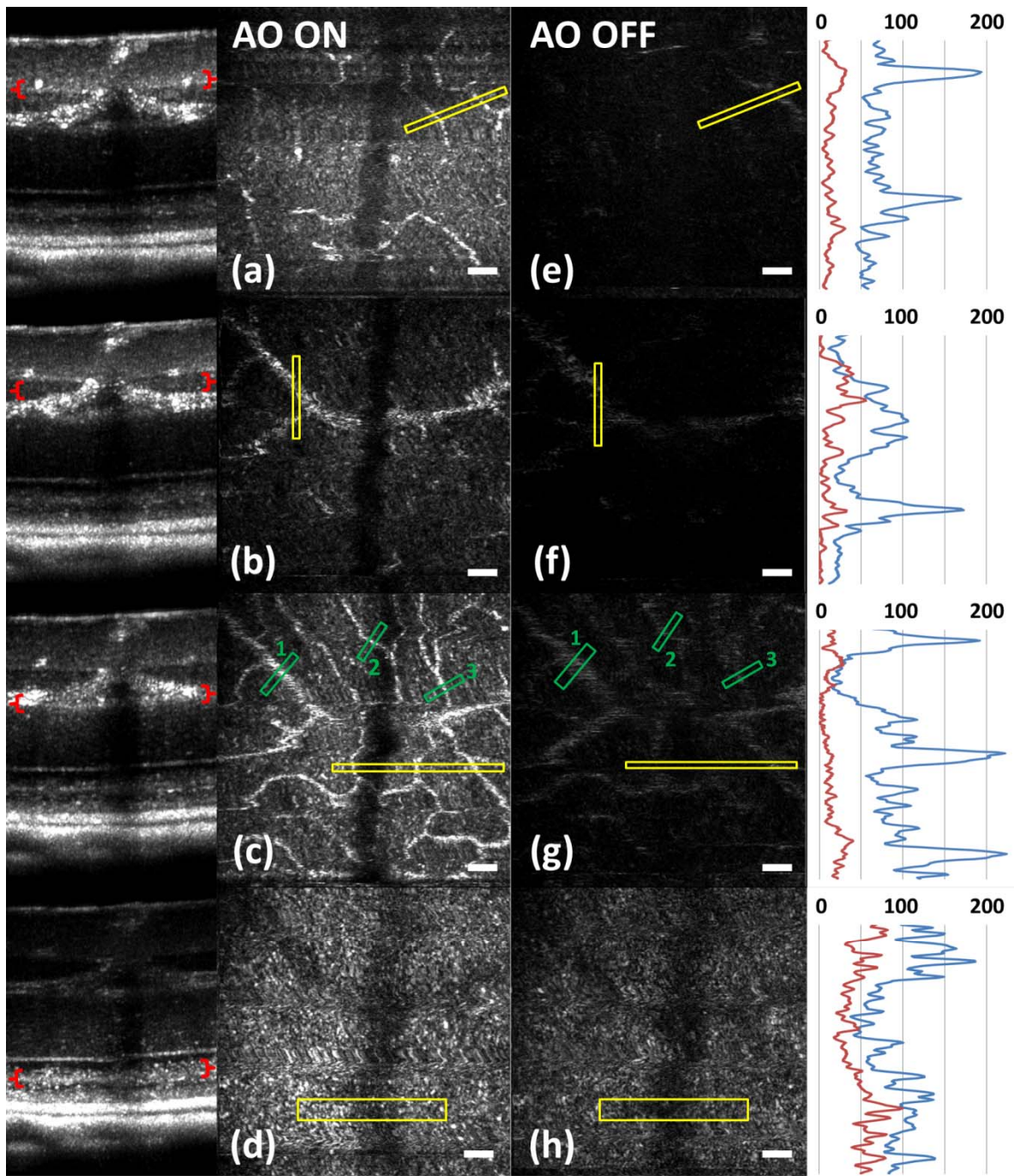


Figure 4.8 Cross sectional and *en face* images (IPL, INL, OPL and PRL) of the mouse retina acquired *in vivo* with the AO FD-OCT system. The focal plane was adjusted on the layers of interest as indicated by the red brackets in the B-scan images by changing the defocus in the AO control software. The axial depths indicated by the brackets in the B-scan represent the locations of (a-d) *en face* projections of the different retinal layers with AO-ON and (e-h) *en face* projections at the same location with AO-OFF (DM flat). Normalized line graphs of the image intensity taken across the capillaries at the locations labeled 1, 2 and 3 in (c) and (g) are presented in the bottom panel. Scale bar: 30 μ m.

Unlike humans, in mice the rods and cones are approximately the same size, $\sim 1.5\mu\text{m}$ in diameter. AO FDOCT images acquired using our system with the focus set at the photoreceptor layer (PRL) are presented in Figure 4.9, the imaging system was modified to have increased numerical aperture of 0.17. With AO ON, an increase in the intensity can be observed, as well as the appearance of bright circular structures that resemble individual photoreceptors. However, the resolution of our AO FDOCT system with increase NA (0.17) is still below what is required to fully resolve the photoreceptor mosaic. Based on the modeling results performed by Putnum et al. for an AO SLO [94], the appearance of the photoreceptor layer that we acquired with the AO ON is similar to what is expected given the current lateral resolution of our system.

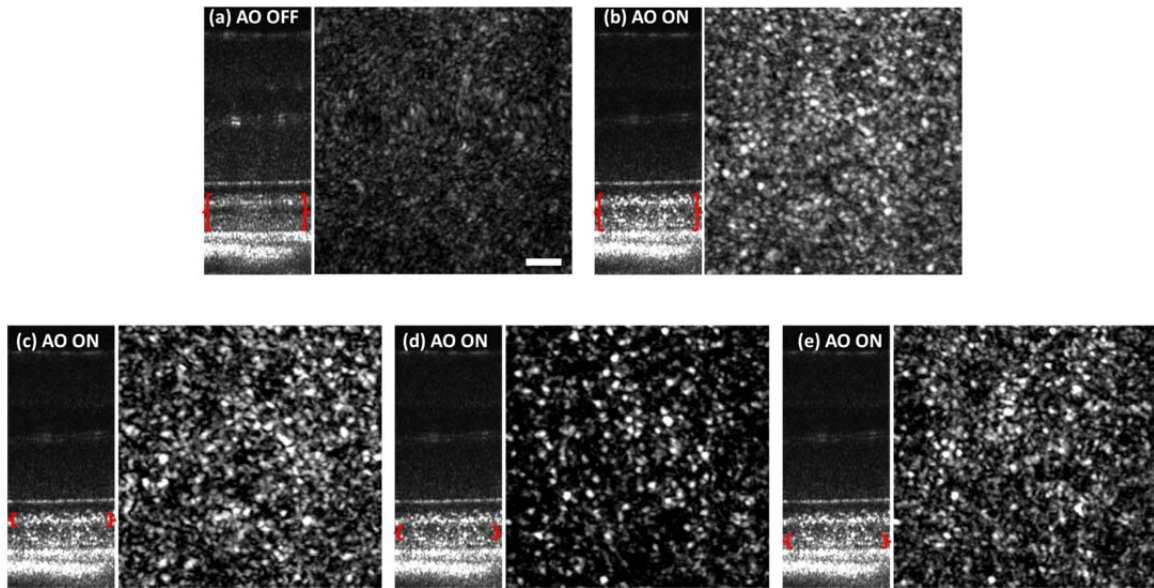


Figure 4.9 AO FDOCT images of the mouse photoreceptor layer acquired *in vivo* with (a) adaptive optics off and (b) with the adaptive optics activated. The bright, circular features observed in the en face images correspond to individual photoreceptors. Bottom row: the en face images are extracted from the depth positions of the photoreceptor layer identified in the B-scan and corresponding to (c) the inner / outer segment junctions, and (d) and (e) two different depths of the outer segments. Scale bar: 10 μ m.

4.4. Discussion

The crucial component in adaptive optics retinal imaging is accurate wavefront sensing. It is particularly challenging with small animals such as mice. Several factors contribute to the complexity of the problem. First, the small size and highly curved eye create large low order aberrations which necessitate a large dynamic range wavefront sensor and correction. Second, the quality of the wavefront spots is poor and greatly decreases the accuracy of wavefront measurement. As discussed in the literature [21], the dual peak wavefront spots are likely caused by the two strong reflections in the retina, from the inner retina (RNFL) and from the outer retina (RPE and choroid) which are observed due to the relatively thick retina compared to the short focal length of the eye. Third, the mouse needs to be anesthetized during image acquisition, causing their cornea to dry out and become cloudy. The increased anterior segment scattering blurs the wavefront sensor spots and decreases the SNR of light backscattered from the

retina if the eyes are not kept moist after anesthetization. Both wavefront images and OCT images will degrade severely with increased clouding of the mouse eye, eventually making wavefront sensing and imaging not possible.

One of the design features of our AO FD-OCT system is that we used a fundus lens to remove the refraction at the air-cornea interface, and instead focused the light with an objective lens. This arrangement allowed light to be focused easily on the outer retina by moving the fundus lens and eye combination together axially, where single peak good quality wavefront images could be acquired. Moreover, by using a single beam for both wavefront sensing and FD-OCT, we were able to monitor the region of the retina on which the imaging beam was focused in real time by observing the B-scans. Also, since the eye being imaged was in contact with the fundus lens, drying of the cornea and clouding was effectively reduced. One potential issue of using an objective lens to focus the light on the retina is that the resulting field of curvature of the image plane does not match the curvature of the mouse retina. This is not a concern for our imaging applications because with AO FD-OCT we are only scanning over a very small region. As observed in the B-scan images in Figure 4.6-Figure 4.8 the retinal surface is effectively flat over small distances.

In order to accurately measure and correct the wavefront error, the pupil plane needs to be optically conjugated onto the wavefront sensor and deformable mirror. We chose to use lens based 4-f telescopes to relay the pupil conjugate planes in order to minimize the astigmatism build-up, a common issue in the mirror based relay systems, and to simplify the optical system design and construction. The compromise with using lenses is the increased back-reflection from the optical refractive elements despite the use of anti-reflection coatings. We mitigated this issue by background subtraction at the wavefront sensor, and slightly tilting the lenses. The residual aberrations of our optical system were measured to be on the order of 60nm RMS, which was negligible compared to the aberrations with the mouse eye present. Alternative techniques to reduce back reflection from the lenses that could be used in the next phase of this research include a confocal pinhole [95], or polarization optics [38].

Compared to what has been reported in the literature [21], the defocus term measured in our study with the AO-OFF (presented in Fig 4 (e) as the 4th coefficient of

the Zernike polynomial) does not represent the refractive power of the mouse eye, but rather the displacement of the retina relative to the focal plane of the objective. Variations in the measured defocus coefficients may be also affected by the small eye artifact [21], [79], [96], which arises due to the fact that the mouse retina is relatively thick compared to the focal length of the mouse eye. Additionally, the presence of the fundus lens and objective lens influences the amplitudes of the Zernike coefficients and therefore they should be used as a metric of the optical system performance, rather than as a measure of the remaining aberrations in the mouse eye. The aberrations that can be reliably measured are also limited by the number of lenslets across the pupil; we are using a commercial AO system with 7 lenslets across the pupil (corresponding to 37 lenslets in the wavefront sensor). To accommodate to this constraint we adopted a smaller pupil size.

The full numerical aperture of the mouse eye was not utilized with the current system design. We estimate that a two-fold increase in the resolution will be needed to resolve with high contrast the complete photoreceptor mosaic in cross sectional and *en face* images. Unlike cSLO, the axial resolution of OCT depends on the bandwidth of the light source; in order to achieve ultrahigh axial resolution, a wide spectral bandwidth is required. This introduces additional challenges for AO-OCT because as the spectrum is broadened, chromatic aberrations will start to affect the spot size [97]. The effect of these chromatic aberrations needs to be studied in further detail to utilize the full NA of the mouse eye. Furthermore, the depth of focus is naturally coupled with the spot size; a small spot size results in a very narrow depth of focus, which is less than the thickness of the photoreceptor layers. Fortunately, OCT has very high sensitivity, and out of focus structures are still visible, but with degraded intensity and resolution [97]. The work by Geng et al. described that application of a deformable mirror with large stroke (45 μm for defocus) was necessary for an ophthalmoscope design utilizing the full NA of the mouse eye [83]. In our method, the refraction cancelling fundus lens combined with the external objective lens extended the effective focal length of the eye. In combination with the use of a smaller pupil size at the mouse eye, this permitted dynamic focusing throughout the full thickness of the mouse retina even with the use of a small stroke (5 μm) deformable mirror.

The implementation of our AO FD-OCT system for mouse imaging is generally in agreement with the results of simulations performed for AO imaging in a model of a rat eye [98]. By using the same light source for both the OCT imaging and the WFS, the strong chromatic aberrations of the mouse eye resulting in different focal planes were avoided. Furthermore, by using the plano-concave fundus lens in contact with the cornea, we largely removed variation between animals of different strains and ages. The conjugated pupil plane became the objective lens instead of mouse pupil which allows us to place the pupil plane with higher precision, and position the retinal layer of interest to the focal plane.

In the future, we plan to improve on the resolution and depth of focus of our system. One of the first steps will be to modify our refractive AO system to allow imaging of the mice through a larger pupil size, thereby increasing the theoretical lateral resolution that is achievable, similarly to recent reports by Geng et. al. [83] where a 2mm pupil at the mouse eye was used for imaging with AO-SLO. Using adaptive optics to improve the lateral resolution and eventually achieve cellular resolution imaging of the photoreceptors *in vivo* is the long range motivation behind this project. Additionally, we plan to incorporate an SLO imaging channel with our rodent AO-OCT system, similar to the design proposed by Zawadzki et. al. for human retinal imaging [71]. This will allow simultaneous acquisition of structural and potentially functional data from mice *in vivo* by using novel fluorescent molecular probes offered by optogenetics [99], [100]. We also plan to investigate ways to extend the depth of focus for the AO FD-OCT system without sacrificing the lateral resolution afforded by AO. Several possible solutions have already been proposed in the literature for high NA OCT imaging, including the use of dynamic focus [101], implementation of a Bessel beam for imaging [102], or the introduction of additional aberrations in AO-OCT system [103].

4.5. High resolution WFS

One of the most challenging issues in AO for mouse retinal imaging is wavefront sensing. In the previous section, we demonstrated the use of a fundus lens to reduce the low order aberrations of the mouse cornea and improve wavefront sensing. In order to fully resolve the photoreceptors mosaic in the mouse eye, a higher NA must be used

for imaging. However, the scattering and the amount of aberrations increase with higher NA which deteriorates the quality of wavefront sensor spots and ultimately leads to reduced wavefront sensor performance. Figure 4.10 (a) and (b) are the wavefront sensor images acquired under different imaging NA; the spots became much larger at higher NA. One possible method to mitigate this effect is to use a higher resolution micro lens array. An array with 300 μ m diameter lenslets and \sim 6mm focal length was evaluated; the wavefront sensor image using this micro lens array is shown in Figure 4.10 (c), the wavefront sensor spots were much smaller compared to ones from lower resolution wavefront sensor.

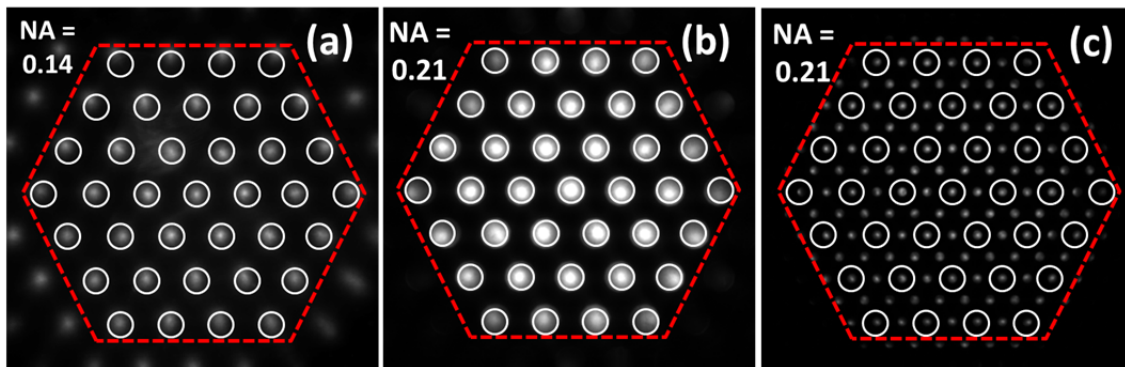


Figure 4.10 Comparison between high resolution and low resolution wavefront sensor under different imaging NA.

The ideal DM to be used with this high resolution wavefront is Iris AO PTT489 DM which offers one to one mapping of the segments to the lenslets. With our current DM (Iris AO PT111), we had to mask out the lenslets that are not in the center of the corresponding DM segments in software to avoid the spots corresponding to light diffracting from the edges of the DM segments. The spots that were included in the wavefront reconstruction are enclosed by the white circles, and correspond to the center of the mirror segments in the IrisAO PT111 DM. Two WFS (high resolution and low resolution) were placed in the AO OCT setup to simultaneously sample the wavefront, and the AO loop could be closed by either WFS. The performance of the two WFS was evaluated with wavefront sensing experiment in the mouse eye. The AO loop was closed by two WFS separately without changing other imaging conditions; the wavefront sensing results for the two WFS from mouse eye was shown in Figure 4.11. Before AO correction two WFS measured similar wavefront aberrations with slightly lower amplitude

from the high resolution WFS. After closing the loop, high resolution wavefront sensor provided a better wavefront correction than the low resolution WFS as illustrated by wavefront map. However, further investigations are needed to confirm the performance of the high resolution wavefront sensor ideally with a matching DM (Iris AO PT489).

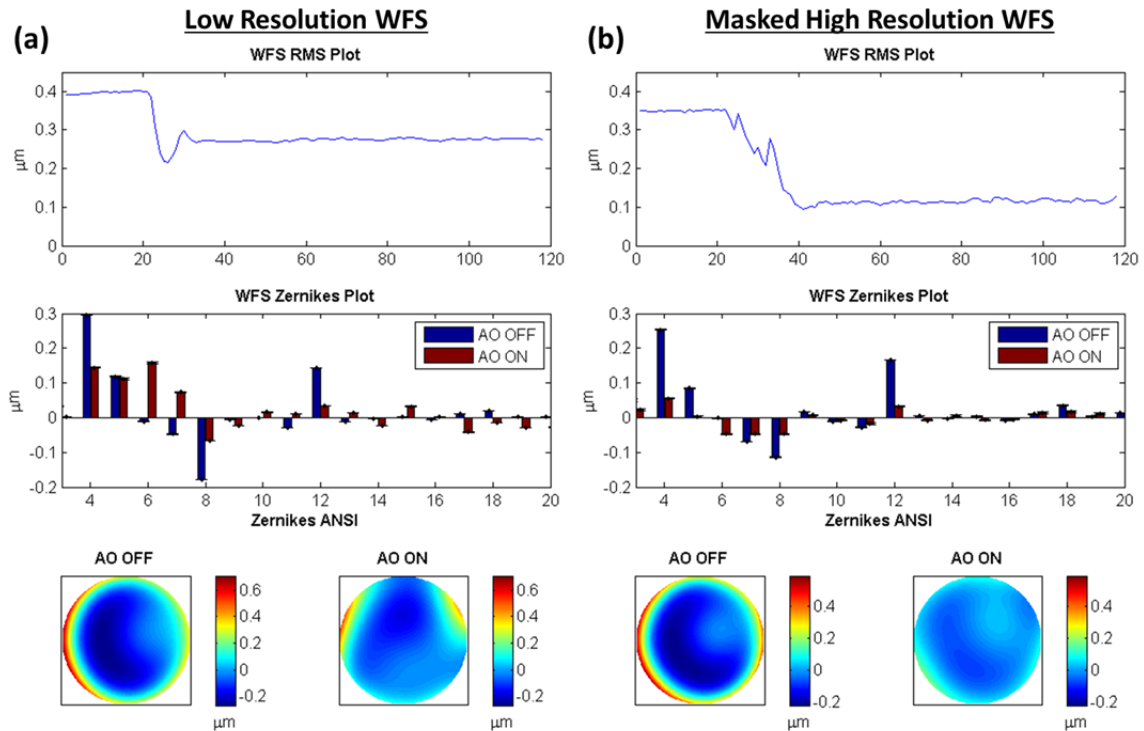


Figure 4.11 Comparison of the performance of low resolution WFS and masked high resolution WFS in the mouse retina. Images from top to bottom are wavefront sensor RMS error plots, Zernike coefficient plots and reconstructed wavefront before and after AO correction.

4.6. Summary

We presented an AO FD-OCT system for small animal retinal imaging using the same light source for both imaging and wavefront sensing. To facilitate mouse imaging, we used a fundus lens to assist with specimen alignment and cancelation of refraction at the cornea. The *in vivo* imaging results presented in this chapter showed an improvement in the brightness and contrast of capillaries and nerve fiber bundles in mouse retina images.

One of the limitations of this approach is the accuracy of wavefront sensing complicated by small eye artifacts. A possible solution to resolve this issue was explored, using a high resolution micro lens array. However, there are still many challenges and requirements. In the next chapter, AO imaging without the wavefront sensor is investigated, using the image quality metric as feedback for aberration correction.

Chapter 5.

Wavefront Sensorless Adaptive Optics Optical Coherence Tomography for in vivo retinal imaging in mice

5.1. Introduction

Adaptive optics (AO) was originally developed to correct for the perturbations of star light passing through the atmosphere that affected the resolving power of large pupil diameter optical telescopes. Over the last fifteen years, adaptive optics has also been integrated into ophthalmoscopes and microscopes for retinal and biological tissue imaging, correcting monochromatic optical aberrations and allowing diffraction limited imaging. AO is required for retinal imaging in humans when the pupil is larger than 3mm [104], to achieve diffraction limited performance using fundus photography, scanning laser ophthalmoscopy (SLO), or optical coherence tomography (OCT) [28], [105]. To better visualize the cellular microstructure and to understand the molecular processes in living retinas, high resolution retinal imaging is desired. Diffraction limited high resolution imaging can be achieved with AO incorporated into the sample arm of an OCT system [31], [69]–[71], [75], [106].

Most AO systems use a wavefront sensor (WFS) which measures the wavefront aberrations, and compensate for them with a wavefront corrector, usually a deformable mirror (DM). The performance of an AO system is limited by the accuracy of the wavefront sensor, and there are various sources of error which lead to imperfect correction of wavefront aberrations [107]. Additionally, wavefront sensing can suffer from non-common path errors, misalignment, detected spot centroiding and wavefront reconstruction errors, back-reflection from lens based systems, etc. Moreover, these issues are exacerbated in small animal retinal imaging systems. Biss et al. demonstrated

that with AO correction of monochromatic aberrations, the brightness and resolution of the image can be increased in mouse retinal imaging with SLO [81]. However, they also reported on the difficulties of wavefront sensing for mice, which may arise from the ‘small eye artifact’. Geng et al. demonstrated the appearance of a double spot in the wavefront sensor (WFS) when the wavefront beacon with a long depth of focus was reflected from the mouse retina, in contrast to a single spot when focusing on a retinal vessel [21]. The latest work from Geng et al. showed exciting results for AO cSLO in a mouse retina *in vivo*, where the wavefront sensing beam was kept in focus on the outer retina to obtain reliable and accurate the wavefront measurements [83]. However, the approach used in these reports on wavefront sensing is likely limited to pigmented mice, and would not likely perform as well in the presence of strong back reflection from the choroid in albino animals.

In order to resolve the issues associated with the Shack-Hartmann wavefront sensing and to extend the applications of AO imaging systems, wavefront sensorless adaptive optics (WSAO) systems have been developed and successfully demonstrated in microscopy and retinal imaging for both humans and mice [80], [82], [108], [109]. These reports have shown that WSAO imaging systems can achieve comparable performance as those with wavefront sensor control. Many different WSAO control algorithms have been extensively investigated and discussed [110]–[112], and can be separated into two main categories: stochastic and imaged-based. Bonora and Zawadzki recently reported on a modal control WSAO OCT system capable of optimizing low order Zernike terms [113], and proposed the possibility of extending the technology for real-time *in vivo* imaging.

The purpose of this chapter is to investigate the combination of WSAO with FD-OCT, enabling selection of the axial position of the AO-system focus using the OCT B-scans, and thus allowing AO correction at the structure of interest. We present a novel modal control WSAO OCT system for small animal retinal imaging, which enables correction of aberrations up to the fifth radial Zernike orders for user-selected layers in real-time. *In vivo* retinal imaging of pigmented and albino mice is presented, and the image quality improvement resulting from AO correction is demonstrated. This work combines the high speed FDOCT GPU processing with the work on AO.

5.2. Methods

5.2.1. AO FD-OCT engine

Our previously reported lens based AO-OCT system was modified for this project, and the details are presented in Figure 5.1. The same light source, spectrometer, and deformable mirror (DM) were used as reported in the manuscript describing our previous AO-OCT system [25]. The spectrometer was custom built with a high speed line scan CMOS camera (Bioptigen, Inc, Durham, NC). The IrisAO segmented MEMS DM (PT111, Iris AO, Inc, Berkeley, CA) was factory-calibrated for accurate open-loop operation for modal control [114]. Due to the wavefront sensorless operation, back-reflection from the lenses was no longer a concern for the AO subsystem, and the mechanical tilt of the lenses was removed to minimize the system aberrations. Removal of restrictions connected with use of the wavefront sensor allowed us to increase the numerical aperture from 0.14 NA up to 0.21 NA. The relatively small (5 μ m) stroke of our DM was sufficient for wavefront correction because the use of the fundus lens reduced the low order aberrations and permitted manual adjustment of the focus [25]. The estimated focal width (Gaussian waist $1/e^2$) for our imaging beam was 1.3 μ m in air and had a corresponding depth of focus of 12 μ m. In order to accommodate the increased NA and pupil size on the objective lens, the 2mm fundus lens (Volk Optical Inc, Mentor, OH) was replaced with a 6mm diameter, -12.5 mm focal length plano-concave lens (KPC013, Newport Instruments, Irvine, CA). The real-time acquisition of rodent retinal volumes consisted of 2048x128x128 pixels (axial points x number of A-scans/B-scan x number of B-scans/volume) with a line rate of 80 kHz during the WSAO optimization stage, and 2048x360x360 pixels with a line rate of 90 kHz for the final data acquisition and saving stage. The increased acquisition speed compared to our previous report helped to significantly reduce motion artifacts when imaging the mouse retina *in vivo*.

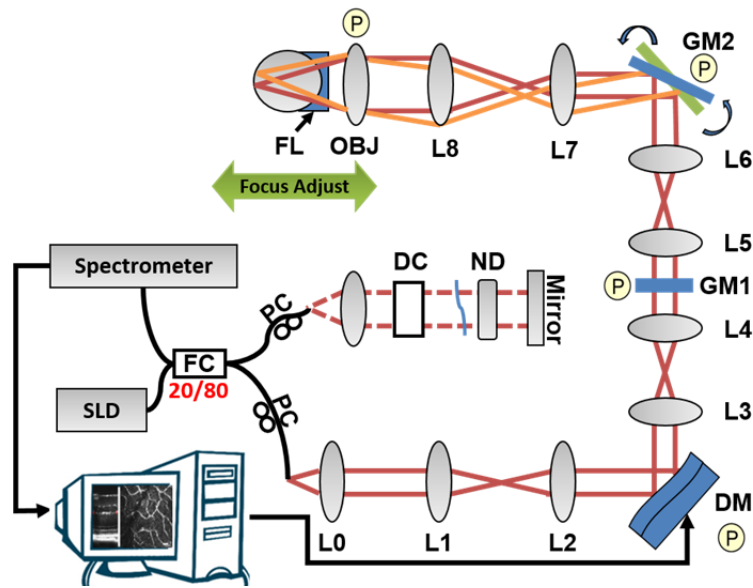


Figure 5.1 Schematic of the WSAO FD-OCT system: DC - dispersion compensation; DM - deformable mirror; FC - 20/80 fiber coupler, 20% of the light from SLD goes to sample arm, 80% goes to reference arm; GM1, GM2 - horizontal and vertical galvo scanning mirrors; FL - fundus lens; PC - polarization controller; SLD - superluminescent diode; L - achromatic lenses: L0: ($f=16\text{mm}$); L1, L2: ($f=300\text{mm}$); L3, L4: ($f=200\text{mm}$); L5, L6: ($f=150\text{mm}$); L7, ($f=100\text{mm}$) L8: ($f=300\text{mm}$); OBJ - objective: ($f=25\text{mm}$); ND - neutral density filter; P represents the location of the planes conjugated to the pupil throughout the system. GM1 is slow scan mirror and is presented unfolded for clarity. Note that the schematic is drawn for illustrative purposes only; it does not reflect the actual physical dimensions of the system.

A custom written program for FD-OCT acquisition with GPU accelerated processing [23], [51], was modified for this project. The updated software is able to generate an *en face* view from the layers of interest, selected by the operator in the OCT B-scan window. Advanced camera controls offer the ability of seamlessly changing the image acquisition parameters, such as the A-scan line rate and sampling rate, in real-time. The DM control functions, whose implementation was based on the IrisAO API, were incorporated into the software for fully automated WSAO. The entire WSAO OCT system requires only one PC and one operator. The OCT processing steps (resampling, numerical dispersion compensation, and FFT) were performed on the GPU [23]. The CPU was used for coordinating data acquisition, configuring the camera via serial control, and synchronizing the scanner (6210H, Cambridge Technology Inc., Lexington, MA) with the camera and frame grabber (PCIe-1433, National Instrument, Austin, TX).

The CPU also controlled the AO optimization. During the optimization stage, the time to update the DM through the controller (Smart Driver II - 128™, IrisAO, Inc, Berkeley, CA) was ~7.1ms.

Data saved during acquisition was written to binary files as unprocessed interferograms. The saved data was processed in Matlab (Mathworks, Inc, Natick, MA) with standard OCT processing (resampling, numerical dispersion compensation, and FFT) for presentation; there was no additional post processing done on the images. Measurement and analysis of the image data was performed using Amira (FEI Visualization Sciences Group, Burlington, MA), and Fiji [115].

5.2.2. Imaged Based Wavefront Sensorless Adaptive Optics Modal Optimization Algorithm

The WSAO optimization process was initialized with manual selection of the axial position (depth range, Δz) of the retinal layer of interest in the B-scan display window of the software. An OCT *en face* image was generated from the user selected region using maximum intensity projection; the brightness of this 2D *en face* image was calculated by summing the intensity of each pixel, and was used as the merit function $J(\mathbf{k})$ as formulated in Eq. 5-1 [116]:

$$J(\mathbf{k}) = \sum_{x,y} \left(\max_{\Delta z} \left(I^{w(\mathbf{k})}(x, y, z) \right) \right), \quad (\text{Eq. 5-1})$$

where \mathbf{k} is vector of the Zernike coefficients; x , y and z are coordinates in image space; and $I^{w(\mathbf{k})}$ is the intensity of the OCT data acquired with the wavefront aberrations $w(\mathbf{k})$ applied to the DM.

The wavefront aberrations $w(\mathbf{k})$ can be represented by a set of orthonormal Zernike polynomials as shown in Eq. 5-2. The IrisAO DM has software libraries to produce approximations of the shapes corresponding to each Zernike polynomial up to the 5th order in the Zernike expansion [117]. For n Zernike radial modes Z , the wavefront aberration was represented as

$$w(\mathbf{k}) = \sum_{n=3}^{20} k_n Z_n. \quad (\text{Eq. 5-2})$$

The modal WSAO algorithm searches for the coefficients of the Zernike polynomial that produce the highest merit function value, and thus minimizes the optical aberrations as indicated in Eq. 5-3. The optimized values of the coefficients are denoted as k_i^* , and the initial value of the Zernike coefficients are denoted as $k^{(0)}$.

$$k_i^* = \arg \max_{k_i} \left(J \left(k_1^*, k_2^*, \dots, k_i, \dots, k_{n-1}^{(0)}, k_n^{(0)} \right) \right),$$

$$k_1^{(0)}, k_2^{(0)}, \dots, k_n^{(0)} = 0. \quad (\text{Eq. 5-3})$$

Due to the orthogonal nature of the Zernike polynomials, the optimization of each Zernike mode can be performed independently [118]. Our optimization determines the appropriate value of the coefficient for each mode. The first Zernike mode to be optimized is the defocus ($n = 4$) followed by astigmatism ($n = 3, 5$) and then the remaining modes. A flowchart for the WSAO modal optimization algorithm is shown in Figure 5.2.

The search for the optimum coefficient began by applying nine linearly spaced values of the Zernike mode coefficient that was being optimized to the DM, with the initial step size determined by prior knowledge. The image intensity merit function corresponding to each of the nine coefficients was acquired and the highest value was found. If there was an improvement in image brightness compared to the last optimized Zernike mode, and the index of the maximum valued coefficient was near the center of the range of coefficients searched (i.e. 4-6), then the shape was applied to the DM and the optimization algorithm advanced to the next Zernike mode. If the index of the maximum valued coefficient was off centered (i.e. 1-3 or 7-9), then a new linear search commenced with a new linearly spaced steps centered on the maximum valued coefficient. If there was no improvement in image quality after one iteration, the algorithm attempted a non-linear search in the central region, with a finer step size for the nine new Zernike coefficients. The algorithm limited the number of search iterations for each Zernike mode, and after reaching the limit, the algorithm applied the DM shape that produced the best merit function, then moved on to optimize the next Zernike mode.

If there was no improvement during the search for specific Zernike mode, the coefficient of that mode was set to zero. Once all Zernike modes were optimized, the adaptive search algorithm terminated.

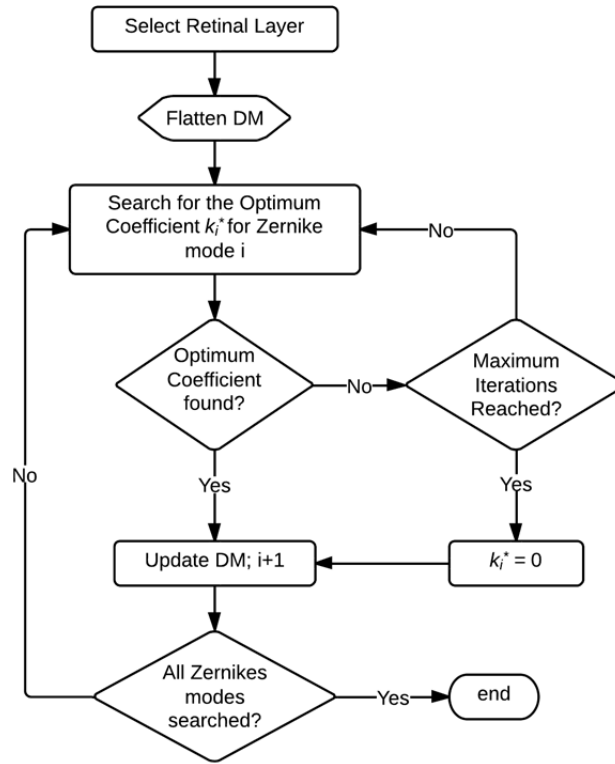


Figure 5.2 WSAO search algorithm flowchart. DM – Deformable Mirror; k_i^* - the optimized coefficient for Zernike mode i .

5.2.3. Mouse Handling

Mice of strain C57BL/6J (pigmented) and BALB/cByJ (albino) imaged in this report were obtained from Jackson Laboratories (Bar Harbor, ME). All mouse imaging experiments were performed under protocols compliant to the Canadian Council on Animal Care, and with the approval of the University Animal Care Committee at Simon Fraser University. The mice were anesthetized (ketamine, dexmedetomidine, and acepromazine mixture (75:1:1 mg/kg body weight) injected intraperitoneally) and revived after the imaging experiment using atipamezole (1mg/kg). A drop of topical anesthetic (Alcaine) was applied before their pupils were dilated using a topical solution (Tropicamide, 0.8%) prior to imaging. Generous amounts of artificial tear gel (Systane

Original, Alcon) were applied in order to maintain corneal hydration. During the imaging session, the mouse was placed on a stage with a bite bar, then the eye was aligned so that it was coupled into the fundus lens with gentle contact. Each imaging session lasted ~30 minutes. The optical power at the mouse eye was ~750 μ w. The maximum time (number of iterations) for the WSAO optimization was fixed; however, the actual number of iterations was dependent on the aberrations present in each individual mouse. We did not observe any differences in the optimization time between albino and pigmented mice. The results presented in this manuscript are representative of the imaging sessions with the 7 mice used in this research.

5.3. Results

5.3.1. Phantom imaging

The WSAO OCT system was tested and validated by imaging a biological phantom (a leaf) placed at the focus of the objective lens. The optimized Zernike coefficients are shown in Figure 5.3, along with the merit function value for each optimized Zernike term. The RMS wavefront of the correction applied was computed from the coefficients of the Zernike polynomial determined through our WSAO algorithm. The final resultant wavefront had an RMS of 52.2nm, which is smaller than $\lambda/14$ (the Maréchal criterion for a diffraction limited optical system). Note that in the Zernike plot of Figure 5.3, the merit function decreased after the optimization of the Zernike mode 16; this could be caused by system errors such as laser power fluctuation and interferometric instability due to the long optical path (~3.5m).

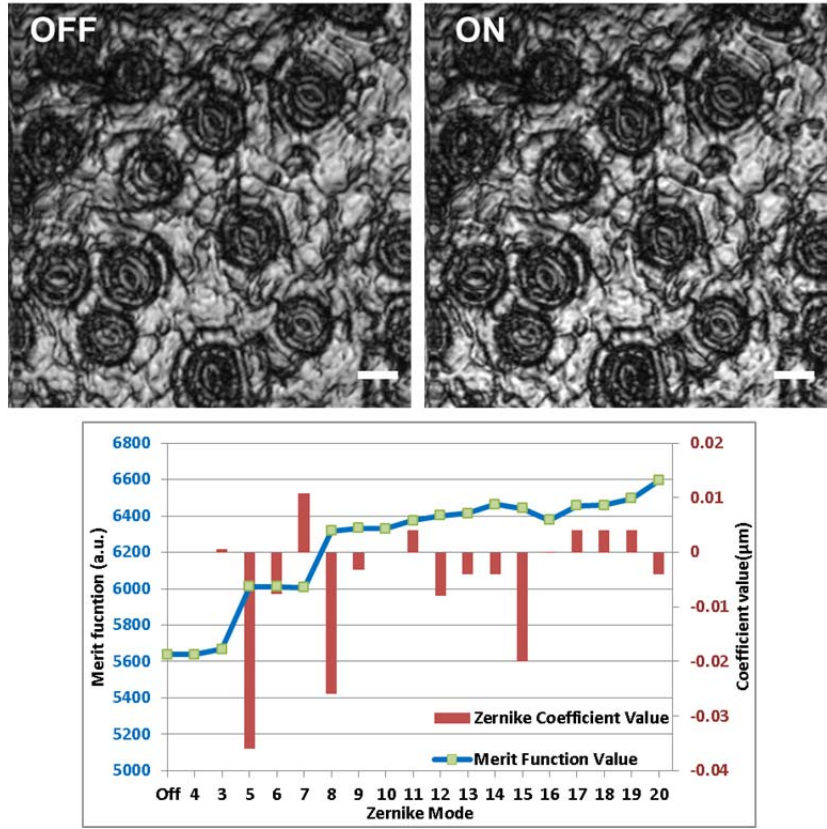


Figure 5.3 OCT images of a leaf with and without WSAO corrections. Bottom figure: (blue line graph) The summed intensity (merit function value) of *en face* images after optimization of each Zernike mode. (red bar graph) The optimized Zernike coefficient value for each Zernike mode. Scale bar: 20 μ m. The Zernike coefficients follow the OSA standard for reporting the optical aberrations of eyes.

Figure 5.4 shows the merit function during the optimization process starting from optimizing of the defocus term ($n = 4$), then the rest of the Zernike terms in increasing order. For demonstration purposes, only the first search iteration for 8 Zernike modes were shown. The merit function for each Zernike mode typically forms a convex shape that is suitable for the optimization algorithm.

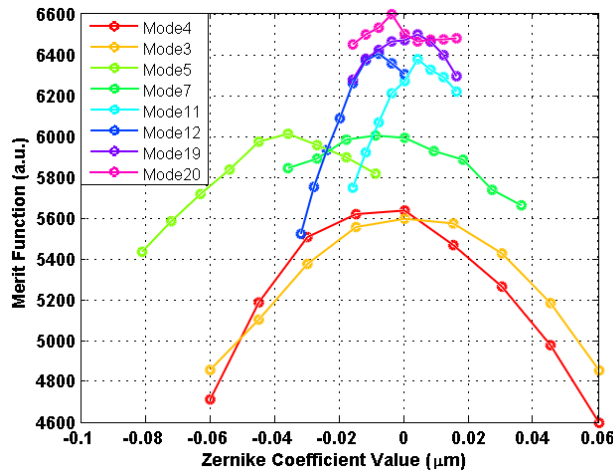


Figure 5.4 Merit function during the optimization process. Only the first search iteration of 8 Zernike modes are shown for clarity of the presentation, further iterations resulted in an increased value of the merit function for some of the terms. The data presented in Figure 5.3 were obtained after the complete optimization process.

5.3.2. Pigmented mouse retinal imaging

The first step in mouse imaging was to use a cross-aiming scan pattern in order to facilitate the alignment, and to ensure that the retina layers were perpendicular to the incident beam. Next, the layer of interest (Nerve Fiber Layer, NFL in this case) was manually placed at the focus of the OCT by translating the combination of mouse and fundus lens relative to the fixed objective. The layer of interest was highlighted by the operator in the OCT B-scan window within the two red lines. The program then generated the *en face* view of the selected layer by maximum intensity projection, and calculated the sum of pixels in the *en face* view, corresponding to the image intensity merit function. Note that the OCT B-scan was displayed in a linear scale. Prior to the WSAO optimization, the low resolution (128 x 128, ~4.6 vol/s) scanning pattern was chosen, and the DM was flattened. All 18 Zernike terms were optimized in 33 iterations, with each iteration consisting of 9 steps. The whole process took ~65 seconds. Figure 5.5 is a screen capture from a video (Media 1 in [26]) that was recorded during an *in vivo* imaging session of a pigmented mouse to demonstrate the WSAO OCT optimization process. For illustration purposes, the video was sped up by a factor of 4. The increase in image brightness and contrast can clearly be observed as the Zernike terms were optimized. Nerve fiber bundles, a blood vessel, and capillaries can be easily

differentiated as the flow in the blood vessel and capillaries was clearly visualized. After WSAO optimization, the scanning pattern was switched to high resolution (360x360pixels) mode visualization and for saving data. Volumes of various fields of view with wavefront optimized (AO ON), as well as volumes with the DM flattened (AO OFF), were saved for comparison purposes.

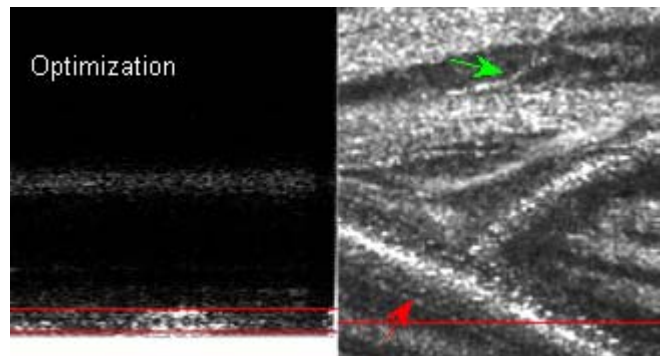


Figure 5.5 Screen capture of an imaging session of a pigmented mouse. The first part of the video presents the WSAO optimization on the nerve fiber layer with a low resolution scanning pattern. The field of view (170x170 μm) was close to the optic nerve head as indicated by the converging nerve fibers. The green arrow points to a capillary and the red arrow points to the edge of the blood vessel wall. The second part of the video that shows the high resolution images is displayed at 2x the acquisition speed, and the field of view was changed to 250x250 μm and 333x333 μm during acquisition.

Images extracted from these volumes are presented in Figure 5.6; the orientation of the B-scan was inverted relative to video. The *en face* images of the NFL were extracted from the OCT volumes at the locations indicated on the B-scan. As mentioned above, for these images, the focal plane was manually placed on the inner retina before WSAO optimization by moving the fundus lens and mouse relative to the fixed objective lens. Not only did the overall image contrast and brightness increase, but more importantly, features such as the capillaries above the nerve fibers and the blood vessel wall around the large vessel at the bottom of the image became more visible and well-defined after AO correction. Figure 5.6(e) shows the summed intensity merit function value (blue line graph) of *en face* images after optimization of each Zernike mode, and the optimized Zernike coefficient value for each Zernike mode (red bar graph). The defocus term (mode 4) provided approximately 40% of the improvement in the image

intensity, whereas correction of the high order aberrations (modes 6 and greater) provided approximately 45% of the total intensity improvement.

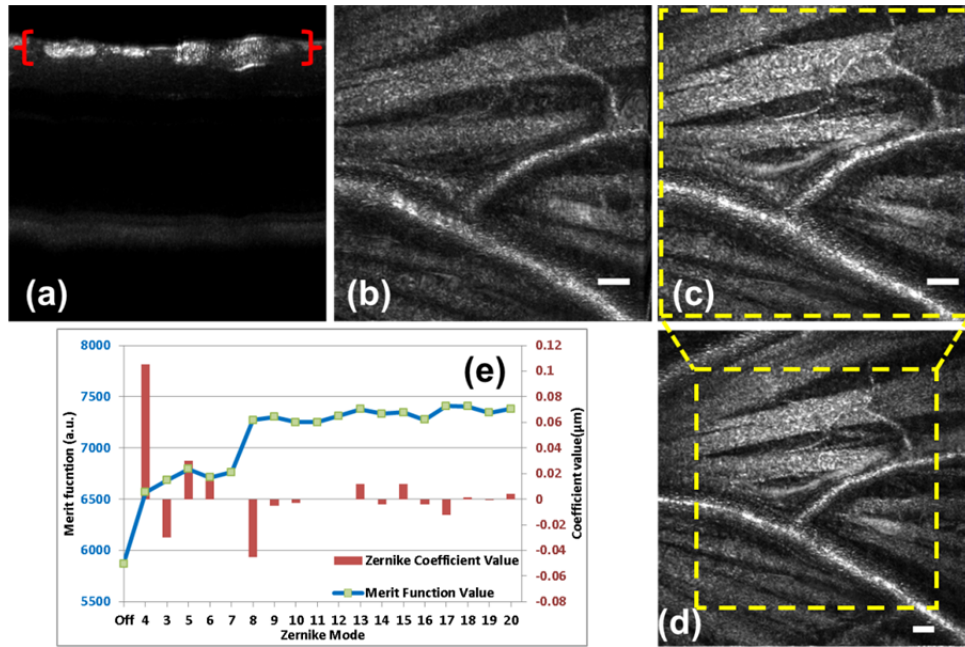


Figure 5.6 WSAO OCT images of NFL of a pigmented mouse. (a) OCT B-scan in linear scale, emphasizing the location and depth of focus of the imaging beam at the NFL. (b-d) *En face* projection of the nerve fiber layer (generated within the red brackets in (a)) before (b) and after (c) WSAO optimization. (d) was acquired with a larger field of view after WSAO optimization. (e) (Blue line graph) the summed intensity (merit function value) of *en face* images after optimization of each Zernike mode. (Red bar graph) the optimized Zernike coefficient value for each Zernike mode. The RMS of the wavefront applied by the DM is 0.125µm. Scale bar: 25µm.

5.3.3. Albino mouse retinal imaging

The lack of pigment in the RPE layer of albino mice results in large and blurry spots when using conventional wavefront sensing. With WSAO OCT, no wavefront sensing is needed, and there is essentially no difference between imaging the inner retina of pigmented versus albino mice. Images acquired *in vivo* from an albino mouse with the WSAO OCT are presented in Figure 5.7. With the AO activated, the layer of interest (Outer Plexiform Layer, OPL) was selected and the aberration correction optimization was performed to obtain the best wavefront correction at that layer. The improvement in image quality with WSAO correction can be seen qualitatively in Figure

5.7 through sharper lines and brighter features (indicative of an improvement in resolution). A quantitative comparison of the increase in brightness and sharpness of the capillaries in the OPL with the WSAO correction is also presented in Figure 5.7. For this imaging session, the defocus term (mode 4) provided approximately 12% of the improvement in the image intensity. Similar to the results presented in Section 3.2, correction of the high order aberrations (modes 6 and greater) provided approximately 40% of the total intensity improvement.

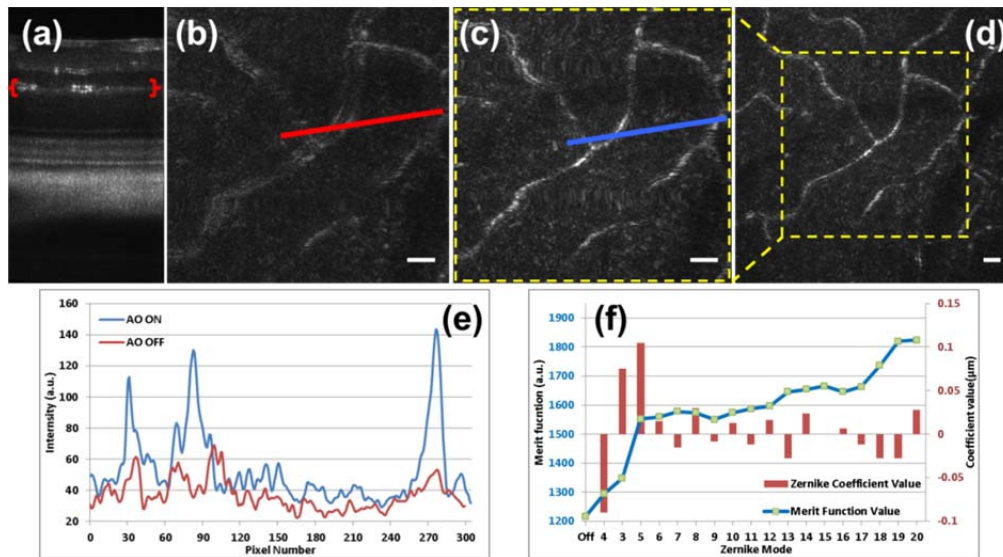


Figure 5.7 (a) Cross sectional images of the albino mouse retina acquired *in vivo* with the sensorless WSAO OCT system presented on a linear scale. The axial depths indicated by the brackets represent the location of the *en face* projection of the retinal layers of interests with AO-OFF (b) and AO-ON (c,d). Scale bar: 20µm. (e) The effect of AO correction is demonstrated by comparing the signal intensity across lines taken from the *en face* images at locations (b, red) and (c, blue). (f) (Blue line graph) The summed intensity (merit function value) of the *en face* images after optimization of each Zernike mode. (Red bar graph) The optimized Zernike coefficient value for each Zernike mode. The RMS of the wavefront applied by the DM is 0.175µm.

5.4. Discussion

Adaptive optics wavefront error correction is an active research area. The performance of the adaptive optics system largely depends on the reliability and accuracy of the wavefront aberration measurements. The issue is further complicated

with strongly scattering and multi-layered samples. Many different techniques have been investigated, such as coherence-gated and confocal wavefront sensing, to name a few [83], [119]–[121]. Wavefront sensorless AO offers a more direct solution. Instead of relying on wavefront aberration measurement from the Shack-Hartmann wavefront sensor as feedback to the AO loop, wavefront sensorless AO analyzes merit functions based on the image (such as image intensity), then iteratively searches for the optimal Zernike modes to apply to the DM.

WSAO OCT provides a practical and promising way to achieve depth resolved aberration correction that does not rely on a wavefront sensor. The WSAO system presented in this report has several advantages over a conventional AO system with wavefront sensor control: it reduces the system complexity and cost, it is immune to the wavefront sensor centroid and reconstruction error, non-common path error, and back-reflection in a lens based system. Lower light levels can be achieved, since there is no consumption of the signal light for wavefront sensing. More importantly, because WSAO OCT detects coherence gated ballistic photons with high SNR, it allows aberration correction in situations when the images have low intensity, or when the layer of interest is obscured by other surfaces in the object. This is the case for mouse retinal imaging, in particular for albino strains where scattering from the choroid dominates. Furthermore, since the OCT provides a cross-sectional view of the retina, our sensorless AO enables aberration correction for user-selected layers in real-time. The capability of depth resolved aberration correction may also be very beneficial for other applications such as deep tissue imaging in brain [122].

We demonstrated WSAO OCT for mouse retinal imaging of structures like nerve fiber bundles, capillaries and a blood vessel wall in pigmented and albino animals. To the best of our knowledge, only Geng et al [83] demonstrated *in vivo* imaging of the photoreceptor mosaic in a pigmented mouse eye with an AO SLO system that had two times higher resolution than the system presented in this report. Increasing the NA of the current system by a factor of two would decrease the depth of focus to be comparable to the coherence length of the source. Our future work includes the investigation of techniques to extend the depth of focus of high NA imaging with OCT. An increased NA would also increase the amplitude of the aberrations, but that could be

mitigated by the use of a deformable mirror with more segments and a larger stroke or a woofer-tweeter configuration [123].

The iterative WSAO aberration correction algorithm is inherently slower than systems with a wavefront sensor that provide direct wavefront measurement. A main challenge of implementing a WSAO imaging system for *in vivo* imaging is the requirement to keep the aberrations relatively static by reducing the subject motion. In our mouse retinal WSAO OCT imaging system, the fundus lens coupled with the mouse eye not only helped to keep the cornea hydrated, but it also reduced the low order aberrations and facilitated alignment. More importantly from the WSAO perspective, it kept the aberrations of the mouse eye static, which allowed the WSAO correction to converge. Furthermore, the anesthetic prescription provided a deeper plane of anesthesia and the increased OCT acquisition speed significantly reduced the motion artifacts when imaging the mouse *in vivo*. As indicated in video, the eye motion was confined to tens of microns both axially and laterally. The residual small motion while imaging the mouse retina *in vivo* is likely the cause of the slight decrease in image intensity after the optimization of some Zernike modes (Figure 5.6(e) Zernike modes 6 and 16, and Figure 5.7(f) Zernike modes 9 and 16). Therefore, our current WSAO implementation is not yet suitable for imaging living human retinas due the dynamic nature of the tear film and constant motion of the human eye.

The converging speed of the WSAO is limited by several factors. Currently, the WSAO OCT operates at 600 B-scans per second, equivalent to ~4.6 volumes per second at our volume size. We could potentially increase the acquisition imaging speed by a factor of 2 by reducing the A-scan length to 1024 pixels per A-scan. In order to further shorten the WSAO converging time, improvements to the optimization algorithm also need to be investigated. We will also explore different merit functions, such as low frequency components in the Fourier domain, and their relationship with the Zernike modes.

5.5. Summary

We presented a wavefront sensorless adaptive optics OCT system that overcomes the issues associated with conventional Shack-Hartmann wavefront sensing in mice, by directly using the image quality data as a merit function for aberration correction. Furthermore, our wavefront sensorless AO approach facilitates the use of a lens based OCT system, which greatly reduces the system complexity. A GPU processing platform was used to accelerate Fourier domain OCT processing for real-time extraction of intensity information from specific retinal layers in the acquired volume. A modal approach of optimizing Zernike terms on the segmented MEMS-based DM was used in combination with an adaptive search algorithm to provide rapid convergence. Images of both pigmented and albino mouse retinas acquired using WSAO OCT system *in vivo* demonstrated improvement in image brightness and feature sharpness. We have demonstrated coherence gated depth resolved AO correction in user selected retinal layers. Combination of WSAO with OCT allows for precise optimization of the image of the structure at the pre-set depth.

In this chapter WSAO OCT was demonstrated that can be used for longitudinal studies. In the next chapter, the real time high resolution WSAO OCT is leveraged for a time course study of laser exposure in the retina.

Chapter 6. In vivo real time visualization of the mouse retina response to laser exposure using wavefront sensorless adaptive optics optical coherence tomography

6.1. Introduction

In the previous chapters, we demonstrated real time *in vivo* high resolution imaging of the mouse retina with AOOCT. We were able to correct aberrations in selected layers in the mouse retina, and retinal structures such as nerve fibre bundles and capillaries have been visualized with exquisite resolution. Although the rod photoreceptors mosaic in the mouse eye has not been fully resolved by our AOOCT imaging system yet, structures that resemble photoreceptors have been visualized with AO correction. Besides the high lateral resolution afforded by the adaptive optics, our AO OCT provides real time visualization of volumetric images which allows the dynamic structural and functional changes in the mouse retina to be captured. The ability to perform detailed time course studies of mouse retina *in vivo* has the potential to accelerate the preclinical investigation of therapies for retinal degeneration. *In vivo* visualization of cellular-level retinal structures with AO FDOCT will enable studies of changes in the retina preceding vision loss in mouse models of diseases causing blindness.

Laser photocoagulation of the retina is a standard treatment for several retinal disease such as age-related macular degeneration (AMD) and diabetic retinopathy [124]. Conventional laser photocoagulation however suffers from some serious side effects such as retinal scarring and decreased peripheral, color, and night vision [125]–[128]. Recently, an exciting model for studying retinal plasticity in response to laser damage [129] and laser exposures [128], [130] has become available. Selective Retinal Therapy (SRT) is a novel research direction using carefully calibrated laser exposure to

selectively photocoagulate only the photoreceptors and RPE, or just the RPE, while leaving the inner retina intact [131]. Research has shown that after selective laser photocoagulation of photoreceptors, unaffected photoreceptors from surrounding areas can migrate into the damaged region to restore continuity of photoreceptors [132]. These migrated photoreceptors can then reconnect to local inner retinal neurons and consequently revive the retinal response to light. Similarly, after selective retinal treatment of RPE, the surrounding RPE cells could also move to the damaged sites and restore RPE continuity. Therefore, in contrast to conventional photocoagulation, selective retinal treatment would not cause permanent retinal scarring or loss of vision. The discovery of retinal plasticity opens new opportunities to improve laser retinal treatment, study retinal circuitry and model retinal degeneration.

In this chapter, we will investigate the ability of AO FDOCT to visualize the morphodynamics of the photoreceptors *in vivo*, and in future study longitudinally as the damaged photoreceptors by laser exposure are replaced by neighboring cells. Studying the retinal response to laser damage will serve as the preliminary data toward the development of a laser induced mouse model of dry AMD, and future *in vivo* studies on retinal plasticity.

6.2. Method

The WSAO OCT imaging system described in Chapter 5 was used in this work with some modifications; Figure 6.1 shows the detailed system schematic. Compared to the previous system, a new objective lens (30mm focal length air-spaced achromat from Thorlabs, Inc) that offered a larger NA (0.23) and better optical quality was used. A continuous wave 473 nm Diode-Pumped Solid-State laser was combined with the NIR OCT light by a hot mirror (#64-471, Edmund Optics Inc) and then focused onto the mouse retina by the objective lens. Two beams were aligned to travel along the same optical path to permit simultaneous imaging and laser exposure at the center of the field of view. The power of the 473nm laser on the mouse cornea was ~10mW; this relatively low power was used to preferentially coagulate the mouse outer retina. Previous studies on the laser injury of mouse retina using standard OCT are limited in the imaging speed and resolution [133]. In this preliminary study, we focused on visualizing the dynamic

response of the mouse retina to laser exposure as the lesion is forming in real time and with high resolution. During the experiment, the anesthetized mouse was first aligned and imaged by the WSAO OCT; the imaging beam was focused on the photoreceptor layer. Then the 473nm laser was turned on, and as the laser exposure started, the real time OCT *en face* images were recorded by screen capture software (Bandicam), future improvement will allow streaming the raw data for further image processing. The 473nm laser was turned off once the lesion formed in the mouse retina. OCT images with different fields of view were saved for reference purposes, and the retinal vessels were used as landmarks to return to the same location in repeat scans in the future.

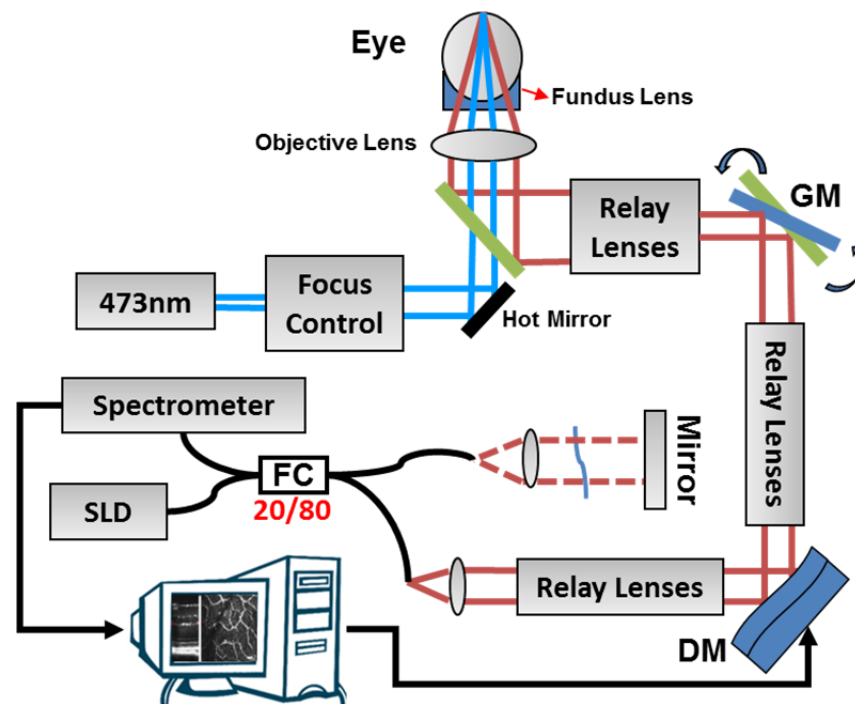


Figure 6.1 Modified WSAO OCT system schematic. SLD - superluminescent diode; GM - galvo scanning mirrors; DM – deformable mirror; FC – fibre coupler.

6.3. Results

The laser exposure experiment was performed with a pigmented wild-type mouse. Our GPU accelerated OCT system allows the volumetric visualization in real time, we were able to monitor the response of the mouse retina to the laser exposure, after the laser exposure started, in ~17 seconds, the retinal lesion was fully formed.

Figure 6.2 shows images of photoreceptor layer and outer nuclear layer before and after laser exposure. The change of the appearance of photoreceptors after laser exposure, and the lesion formation in the ONL can be clearly observed.

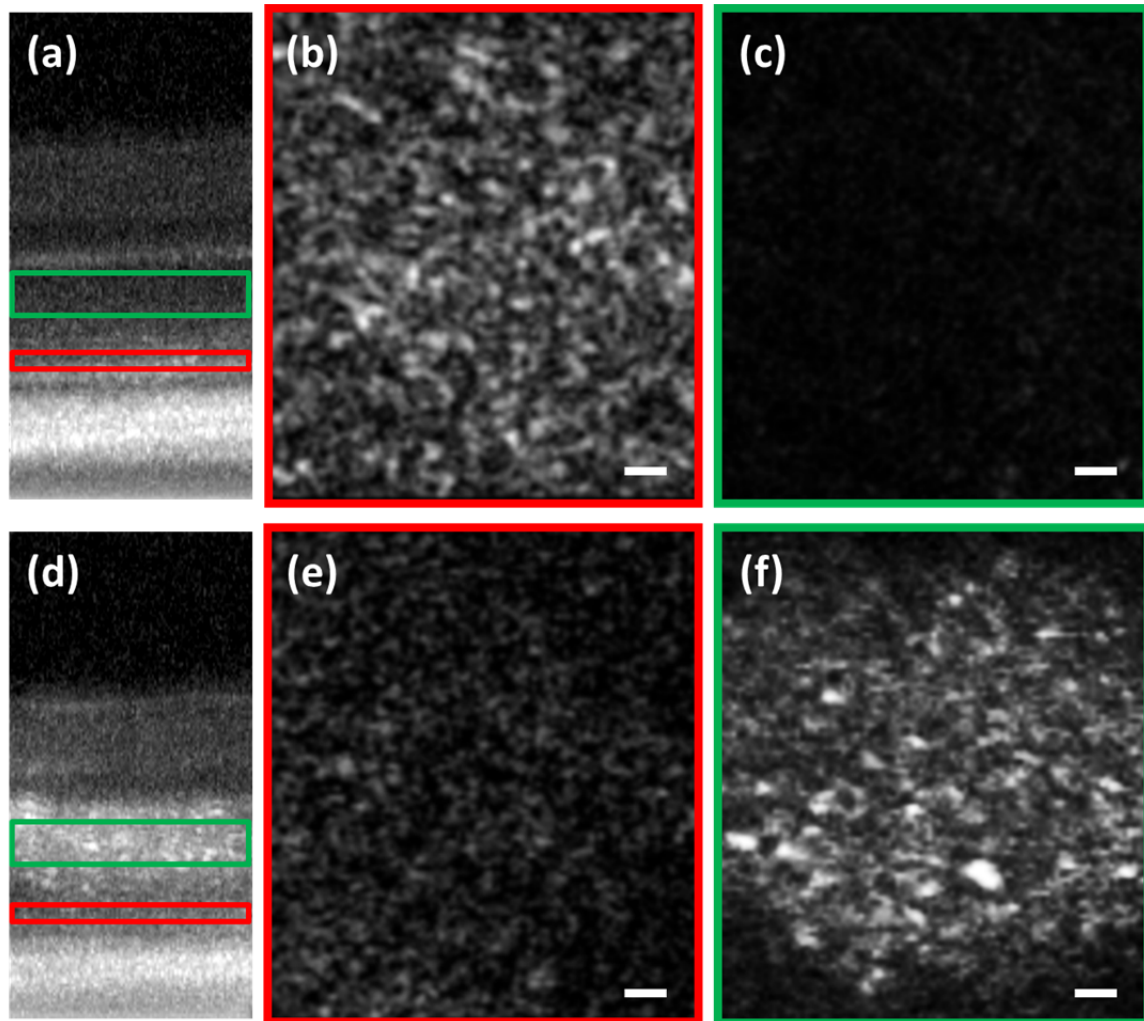


Figure 6.2 OCT images of mouse retina before and after laser exposure, (a) and (d) are mouse retina OCT B-scan, *en face* projection were generated from the layers indicated by the green (ONL) and red (photoreceptors layer) box in the B-scan. (b) and (c) are images before laser exposure, and (e) and (f) are images after laser exposure.

6.4. Discussion

Images presented in the results section are the preliminary data from our early experiments of laser exposure on the mouse retina. We demonstrated the ability to acquire high lateral resolution data with WSAO AO, and leveraged the high speed imaging with GPU to visualize retina structural changes in real time. Due to the availability of the suitable laser light source, the laser exposure made on the mouse retina was relatively long but with low power. OCT imaging results suggested that laser exposure only selectively affected the outer retina while leaving the inner intact; however, further validation is needed. High speed volumetric visualization of the OCT images and the ultra-high lateral resolution afforded by WSAO enabled capturing cellular level structural changes in the retina in real time. Although we have not yet resolved the complete photoreceptor mosaic, the bright circular structures closely resembling the photoreceptors were evident in the images and appeared to be static before laser exposure. Shortly after the laser exposure started, the appearance of these structures changed dramatically, indicating photodamage to this layer. As the laser exposure continued, the light scattering from ONL increased significantly, and a lesion was formed in the ONL at the end of the exposure indicating changes in the cell nuclei in that layer.

Experiments performed in this chapter demonstrated exciting application of WSAO OCT and high speed volumetric imaging studying the response of the mouse retina to laser exposures. In the future, we will longitudinally study the healing processing and retinal plasticity of the mouse retina after laser exposure, imaging the same mouse at different times. Selective laser treatments will be investigated using short duration of high intensity light with limited photodamage to the photoreceptors and RPE as proposed in the literature [134].

6.5. Summary

In this chapter, we used the WSAO OCT to study and visualize the dynamic response of mouse retina to laser exposure. The GPU accelerated processing was an integral component of the imaging; real time *en face* images were used for WSAO

optimization, and for visualization of changes in mouse retina in real time. Preliminary results have shown that we were able to capture the rapid morphology changes of the retinal layers. Future experiments will be conducted to study the healing process and retinal plasticity of the mouse retina after laser exposure, longitudinal studies will be performed with the same mouse over time.

Chapter 7. Conclusion and future work

7.1. Conclusion

In this thesis, we described a highly optimized CUDA-based program to perform FDOCT data processing and 3D volumetric rendering in real time, to the best of our knowledge this is the fastest implementation of the FDOCT processing pipeline presented in literature to date. GPU accelerated OCT processing provides real time visualization of volumetric images which was essential for *in vivo* mouse retinal imaging with AOOCT. The ultra-high processing speed and the robust implementation of our GPU acceleration OCT software enables research in a wide range of OCT applications such as intra-operative OCT for image guided ophthalmic surgery.

We demonstrated the first adaptive optics optical coherence tomography imaging system for mouse retinal imaging that is specifically designed to accommodate the special optical properties for the mouse eye. To facilitate mouse imaging, a fundus lens was used to reduce the low order aberration. Images of mouse retina acquired with AOOCT showed significant improvement in the brightness and contrast of capillaries and nerve fiber bundles. However, the accuracy of the wavefront sensing in the mouse eye limited the numerical aperture that could be used in the system and only pigmented mice were imaged with good performance.

A novel wavefront sensorless adaptive optics OCT system was developed to overcome the issues associated with conventional Shack-Hartmann wavefront sensing in mice and facilitates the use of a lens based OCT system, which greatly reduces the system complexity. GPU accelerated processing of the OCT data permitted real-time extraction of image quality metrics (intensity) for arbitrarily selected retinal layers to be optimized. Modal control of a commercially available segmented deformable mirror (IrisAO Inc.) provided rapid convergence using a sequential search algorithm. Combination of WSAO with OCT allows for precise optimization of the image of the

structure at the pre-set depth. Images of both pigmented and albino mouse retinas acquired using WSAO OCT system *in vivo* demonstrated superior image quality.

The depth resolved aberration correction capability of WSAO OCT may also be very beneficial for other applications such as deep tissue imaging in brain where the direct wavefront sensing is challenging. Since WSAO OCT uses image quality metric directly as the metric to optimize the wavefront, no wavefront sensor is needed.

The real time high resolution WSAO OCT was leveraged for a time course study of laser exposure in the retina. Cellular level structural changes in the retina were captured in real time during the laser exposure. The preliminary results from this study are useful for future study of healing process and retinal plasticity after laser exposure.

7.2. Future work

Adaptive optics optical coherence tomography demonstrated in this thesis holds great potential in scientific and clinical application. Some possible directions to advance the AOCT technology are listed below.

7.2.1. Refinement of WSAO OCT system

Custom high NA objective lens for mouse retinal imaging

The AOCT system presented in this thesis did not utilize the full NA of the mouse eye. The fundus lens approach offers multiple benefits as discussed in Chapter 4 and 5; however, with the refraction power of the mouse cornea canceled, an objective lens is needed to focus the light on the retina, the maximum attainable numerical aperture of our imaging system is currently limited by the availability of long working distance near infrared objective lens. One possible solution is to design a multi-element positive meniscus lens integrating the attributes of the objective lens and the fundus lens. The first element will provide focusing, and the last element will provide refraction cancellation at the cornea. Incorporating an air (or fluid-filled) adjustable gap between the first and last element will permit focus adjustment through the depth of the retina, which is a strength of our initial design, and will also enable scanning with a higher NA

beam. Another potential benefit in combining the objective and fundus lenses is that the static spherical aberration compensation can be inserted in the objective lens as well.

Reduction of motion artifact during in vivo retinal imaging in mice

Motion is a significant source of artifact when imaging at cellular resolution *in vivo*. Even though the mice are anaesthetised during imaging, micron-scale motion persists. In order to stabilize the mouse during imaging, a custom stereotactic mouse holder with bite bar and ear bars that accommodates the AO FDOCT system can be designed. Alternatively, motion artifacts can also be reduced by minimizing the volume acquisition time with either increasing the acquisition speed or acquiring smaller volumes. Furthermore, the GPU-accelerated FDOCT processing described in Chapter 3 can be extended to a multi-GPU system that performs real time motion rejection via software registration of OCT B-scans to reduce the errors in optimization process. OCT *en face* view can be motion corrected and registered as well to improve the image quality. Lastly, dynamic three dimensional cellular level motion tracking might be possible if combine the state of the art retinal motion tracking system with real time retinal segmentation that may be implemented with our GPU accelerated OCT processing software [135].

Faster converging algorithm for WSAO

Compared to closed-loop AO, wavefront sensorless AO is inherently slower due to the iterative optimization process. For our WSAO OCT system described in Chapter 5, we used a relatively exhaustive search method. Our image-based modal WSAO algorithm can be potentially sped 20x by leveraging the quartic relationship between the amplitude of Zernike mode and the merit function, the optimization process can be potentially completed with $N+1$ measurements, where N is the number of Zernike modes to be corrected [136]. WSAO OCT for human imaging might be possible with an improved algorithm, faster image acquisition, and more intelligent scanning pattern.

7.2.2. Wavefront sensorless adaptive optics simultaneous two-photon excitation fluorescence and optical coherence tomography using the same light source

Two-photon excitation fluorescence (TPEF) is a powerful functional imaging modality. Unlike single photon fluorescence, where the molecule is excited throughout the optical path of the beam, TPEF only occurs with significant intensity within the narrow focal volume where the photon density is highest, thus reducing photobleaching [137]. Consequently, TPEF allows optical depth sectioning of fluorescence without the need for a confocal pinhole. TPEF is of particular interest to functional retinal imaging thanks to its ability of exciting fluorophores at longer wavelength [138]–[140], and adaptive optics two-photon retinal imaging has been demonstrated in the living primate and mouse eye [141], [142].

The femtosecond-pulse laser used in two-photon imaging with sufficiently broad optical spectrum can also be used as the light source for FDOCT. The high pulse energy of femtosecond lasers opens the exciting possibilities of complementing FDOCT imaging with multi-photon, non-linear optical processes as methods of generating contrast [143]. With the improved focusing ability afforded by the WSAO system described in Chapter 5, AO FDOCT and TPEF images can be acquired simultaneously in the mouse RPE *in vivo* with a femtosecond pulsed laser as the light source. This novel combination of naturally co-registered structural and functional imaging has the potential to revolutionize *in vivo* studies of mouse models of retinal diseases by allowing the design of new experiments that take advantage of non-invasive visualization of both the RPE cell function preceding photoreceptor death and volumetric photoreceptor morphology.

Non-invasive cellular-resolution fluorescence imaging of the RPE in mice can facilitate the understanding of the mechanisms of diseases such as Stargardt's disease and AMD, and accelerate the development of therapies for potential use in humans. Additionally, the AO FDOCT / TPEF system can be used to visualize the endogenous fluorescence from molecules in the photoreceptors whose excitation spectrum is below 400nm (the short wavelength limit of the optical window in the eye), and enable studies on the visual cycle in mouse models of retinal degenerative diseases such as Retinitis Pigmentosa. Given that the optical power used for AO FDOCT / TPEF is low enough

that no damage to the retina is anticipated, the research may also lay the groundwork for future human functional retinal imaging, where it may be used to study progressive retinal pathology, and an individual's response to therapies in early stage trials.

7.2.3. Extended depth of focus optical coherence tomography with wavefront sensorless adaptive optics

The high numerical aperture used in the AO OCT imaging system results in a very short depth of focus. Although the lateral and axial resolution of OCT are decoupled, most OCT systems use an imaging beam with an approximately Gaussian profile, where the depth of focus decreases with the square of the beam waist. Therefore, the OCT *en face* images extracted from outside of the focus region are still severely blurred.

An extended depth of focus imaging scheme for OCT is possible through the use of an axicon lens, which converts a Gaussian beam into a Bessel beam in the near field. Several reports have used a Bessel beam profile in the OCT sample arm, extended depth of focus has been realized despite a few issues [102] [144] [102] [145]. Recently, Lorensen et al reported a low-Fresnel-number regime, in which axicons with Gaussian illumination can generate energy-efficient Bessel beams with a small number of side lobes, thus consequently increase the SNR of OCT [146].

Bessel beam OCT is attractive and promising; however, the effect of optical aberrations on the Bessel beam has not yet been explored. With our WSAO technique, it is possible to incorporate the adaptive optics with the extended depth of focus OCT, since the WSAO does not need a wavefront reference to operate. An ultra-high resolution OCT imaging system with same resolution in all the voxels may be realized by the combining the extended depth of focus and wavefront sensorless adaptive optics OCT, and such system will has great potential and applications in imaging of biological tissues.

7.3. Acknowledgements

The research in this thesis is generously supported by multiple funding agencies and foundations, we gratefully acknowledge Michael Smith Foundation for Health Research (MSFHR), Natural Sciences and Engineering Research Council of Canada (NSERC), Canadian Institutes of Health Research (CIHR), and the Foundation Fighting Blindness (FFB).

R.J. Zawadzki was supported by the National Eye Institute (EY 014743), UC Davis RISE Grant, NSF I/UCRC CBSS Grant and Research to Prevent Blindness. S. Bonora acknowledges the Short Term Mobility 2013 program of the National Council of Research of Italy. We would like to acknowledge the kind support of Iris AO, Inc and insightful discussions with Mr. Weiguang Ding.

References

1. A. F. Fercher, K. Mengedocht, and W. Werner, "Eye-length measurement by interferometry with partially coherent light," *Opt. Lett.*, vol. 13, no. 3, p. 186, Mar. 1988.
2. D. Huang, E. Swanson, C. Lin, J. Schuman, W. Stinson, W. Chang, M. Hee, T. Flotte, K. Gregory, C. Puliafito, and al. et, "Optical coherence tomography," *Science (80-.)*, vol. 254, no. 5035, pp. 1178–1181, Nov. 1991.
3. A. F. Fercher, W. Drexler, C. K. Hitzenberger, and T. Lasser, "Optical coherence tomography - principles and applications," *Reports Prog. Phys.*, vol. 66, no. 2, pp. 239–303, Feb. 2003.
4. W. Drexler and J. G. Fujimoto, Eds., *Optical Coherence Tomography*. Berlin, Heidelberg: Springer Berlin Heidelberg, 2008.
5. G. Song and K. Harding, "OCT for industrial applications," in *Photonics Asia*, 2012, p. 85630N.
6. M. Choma, M. Sarunic, C. Yang, and J. Izatt, "Sensitivity advantage of swept source and Fourier domain optical coherence tomography," *Opt. Express*, vol. 11, no. 18, p. 2183, Sep. 2003.
7. R. Leitgeb, C. Hitzenberger, and A. Fercher, "Performance of fourier domain vs time domain optical coherence tomography," *Opt. Express*, vol. 11, no. 8, p. 889, Apr. 2003.
8. J. F. de Boer, B. Cense, B. H. Park, M. C. Pierce, G. J. Tearney, and B. E. Bouma, "Improved signal-to-noise ratio in spectral-domain compared with time-domain optical coherence tomography," *Opt. Lett.*, vol. 28, no. 21, p. 2067, Nov. 2003.
9. M. Wojtkowski, "High-speed optical coherence tomography: basics and applications.," *Appl. Opt.*, vol. 49, no. 16, pp. D30–61, Jun. 2010.
10. W. Wieser, B. R. Biedermann, T. Klein, C. M. Eigenwillig, and R. Huber, "Multi-Megahertz OCT: High quality 3D imaging at 20 million A-scans and 45 GVoxels per second," *Opt. Express*, vol. 18, no. 14, p. 14685, Jun. 2010.
11. M. V. Sarunic, A. Yazdanpanah, E. Gibson, J. Xu, Y. Bai, S. Lee, H. U. Saragovi, and M. F. Beg, "Longitudinal study of retinal degeneration in a rat using spectral domain optical coherence tomography," *Opt. Express*, vol. 18, no. 22, pp. 23435–23441, Oct. 2010.

12. Y. Bai, J. Xu, F. Brahim, Y. Zhuo, M. V Sarunic, and H. U. Saragovi, "An agonistic TrkB mAb causes sustained TrkB activation, delays RGC death, and protects the retinal structure in optic nerve axotomy and in glaucoma.," *Invest. Ophthalmol. Vis. Sci.*, vol. 51, no. 9, pp. 4722–4731, 2010.
13. Y. Bai, P. Dergham, H. Nedev, J. Xu, A. Galan, J. C. Rivera, S. ZhiHua, H. M. Mehta, S. B. Woo, M. V Sarunic, K. E. Neet, and H. U. Saragovi, "Chronic and acute models of retinal neurodegeneration TrkA activity are neuroprotective whereas p75NTR activity is neurotoxic through a paracrine mechanism.," *J. Biol. Chem.*, vol. 285, no. 50, pp. 39392–400, Dec. 2010.
14. J. Xu, L. L. Molday, R. S. Molday, and M. V. Sarunic, "In Vivo Imaging of the Mouse Model of X-Linked Juvenile Retinoschisis with Fourier Domain Optical Coherence Tomography," *Invest. Ophthalmol. Vis. Sci.*, vol. 50, no. 6, pp. 2989–2993, Jan. 2009.
15. D. C. Lee, J. Xu, M. V Sarunic, and O. L. Moritz, "Fourier domain optical coherence tomography as a noninvasive means for in vivo detection of retinal degeneration in *Xenopus laevis* tadpoles.," *Invest. Ophthalmol. Vis. Sci.*, vol. 51, no. 2, pp. 1066–1070, 2010.
16. Y. Jian, A. Issaei, R. J. Zawadzki, and M. V. Sarunic, "Adaptive optics: optical coherence tomography system for in-vivo imaging of the mouse retina," in *SPIE BIOS*, 2012, vol. 8213, p. 82130L–82130L–7.
17. V. J. Srinivasan, T. H. Ko, M. Wojtkowski, M. Carvalho, A. Clermont, S.-E. Bursell, Q. H. Song, J. Lem, J. S. Duker, J. S. Schuman, and J. G. Fujimoto, "Noninvasive volumetric imaging and morphometry of the rodent retina with high-speed, ultrahigh-resolution optical coherence tomography.," *Invest. Ophthalmol. Vis. Sci.*, vol. 47, no. 12, pp. 5522–8, Dec. 2006.
18. M. Ruggeri, H. Wehbe, S. Jiao, G. Gregori, M. E. Jockovich, A. Hackam, Y. Duan, and C. A. Puliafito, "In Vivo Three-Dimensional High-Resolution Imaging of Rodent Retina with Spectral-Domain Optical Coherence Tomography," *Invest. Ophthalmol. Vis. Sci.*, vol. 48, no. 4, pp. 1808–1814, Apr. 2007.
19. K. H. Kim, G. N. Maguluri, K. Cusato, R. B. Barlow, and J. F. De Boer, "Monitoring mouse retinal degeneration with high-resolution spectral-domain optical coherence tomography," *J. Vis.*, vol. 8, pp. 1–11, 2008.
20. M. Ruggeri, G. Tsechpenakis, S. Jiao, M. E. Jockovich, C. Cebulla, E. Hernandez, T. G. Murray, and C. a Puliafito, "Retinal tumor imaging and volume quantification in mouse model using spectral-domain optical coherence tomography.," *Opt. Express*, vol. 17, no. 5, pp. 4074–83, Mar. 2009.
21. Y. Geng, L. A. Schery, R. Sharma, A. Dubra, K. Ahmad, R. T. Libby, and D. R. Williams, "Optical properties of the mouse eye.," *Biomed. Opt. Express*, vol. 2, no. 4, pp. 717–738, Jan. 2011.

22. Y. Geng, K. P. Greenberg, R. Wolfe, D. C. Gray, J. J. Hunter, A. Dubra, J. G. Flannery, D. R. Williams, and J. Porter, "In vivo imaging of microscopic structures in the rat retina.," *Invest. Ophthalmol. Vis. Sci.*, vol. 50, no. 12, pp. 5872–9, Dec. 2009.
23. Y. Jian, K. Wong, and M. V Sarunic, "Graphics processing unit accelerated optical coherence tomography processing at megahertz axial scan rate and high resolution video rate volumetric rendering," *J. Biomed. Opt.*, vol. 18, no. 2, pp. 026002–026002, Feb. 2013.
24. J. Xu, K. Wong, Y. Jian, and M. V. Sarunic, "Real-time acquisition and display of flow contrast using speckle variance optical coherence tomography in a graphics processing unit," *J. Biomed. Opt.*, vol. 19, no. 2, p. 026001, Feb. 2014.
25. Y. Jian, R. J. Zawadzki, and M. V Sarunic, "Adaptive optics optical coherence tomography for in vivo mouse retinal imaging.," *J. Biomed. Opt.*, vol. 18, no. 5, p. 56007, May 2013.
26. Y. Jian, J. Xu, M. A. Gradowski, S. Bonora, R. J. Zawadzki, and M. V. Sarunic, "Wavefront sensorless adaptive optics optical coherence tomography for in vivo retinal imaging in mice," *Biomed. Opt. Express*, vol. 5, no. 2, p. 547, Jan. 2014.
27. J. Liang, D. R. Williams, and D. T. Miller, "Supernormal vision and high-resolution retinal imaging through adaptive optics.," *J. Opt. Soc. Am. A. Opt. Image Sci. Vis.*, vol. 14, no. 11, pp. 2884–92, Nov. 1997.
28. D. R. Williams, "Imaging single cells in the living retina.," *Vision Res.*, vol. 51, no. 13, pp. 1379–1396, Jul. 2011.
29. A. Roorda, F. Romero-Borja, I. Donnelly, H. Queener, T. Hebert, and M. Campbell, "Adaptive optics scanning laser ophthalmoscopy," *Opt. Express*, vol. 10, no. 9, pp. 405–412, May 2002.
30. D. T. Miller, "Coherence gating and adaptive optics in the eye," *Proc. SPIE*, vol. 4956, pp. 65–72, 2003.
31. R. J. Zawadzki, S. M. Jones, S. S. Olivier, M. Zhao, B. A. Bower, J. A. Izatt, S. Choi, S. Laut, and J. S. Werner, "Adaptive-optics optical coherence tomography for high-resolution and high-speed 3D retinal in vivo imaging.," *Opt. Express*, vol. 13, no. 21, pp. 8532–8546, Oct. 2005.
32. M. Pircher, J. S. Kroisamer, F. Felberer, H. Sattmann, E. Götzinger, and C. K. Hitzenberger, "Temporal changes of human cone photoreceptors observed in vivo with SLO/OCT.," *Biomed. Opt. Express*, vol. 2, no. 1, pp. 100–12, Jan. 2010.
33. J. W. Goodman, *Introduction to Fourier Optics*. Roberts and Company Publishers, 2005, p. 491.
34. T. W. C. J. R. Sheppard, "Image formation in confocal scanning microscopes," *Optik (Stuttg.)*, vol. 55, no. 4, pp. 331–342, 1980.

35. A. Dubra and Y. Sulai, "Reflective afocal broadband adaptive optics scanning ophthalmoscope.," *Biomed. Opt. Express*, vol. 2, no. 6, pp. 1757–68, Jun. 2011.
36. S.-H. Lee, J. S. Werner, and R. J. Zawadzki, "Improved visualization of outer retinal morphology with aberration cancelling reflective optical design for adaptive optics - optical coherence tomography.," *Biomed. Opt. Express*, vol. 4, no. 11, pp. 2508–17, Jan. 2013.
37. Z. Liu, O. P. Kocaoglu, and D. T. Miller, "In-the-plane design of an off-axis ophthalmic adaptive optics system using toroidal mirrors.," *Biomed. Opt. Express*, vol. 4, no. 12, pp. 3007–29, Jan. 2013.
38. F. Felberer, J.-S. Kroisamer, C. K. Hitzenberger, and M. Pircher, "Lens based adaptive optics scanning laser ophthalmoscope," *Opt. Express*, vol. 20, no. 16, pp. 17297–17310, Jul. 2012.
39. J. M. Geary, *Introduction to Wavefront Sensors*. SPIE Press, 1995, p. 168.
40. B. C. Platt and R. Shack, "History and principles of Shack-Hartmann wavefront sensing.," *J. Refract. Surg.*, vol. 17, no. 5, pp. S573–7.
41. S. Thomas, "Optimized centroid computing in a Shack-Hartmann sensor," in *Advancements in Adaptive Optics. Edited by Domenico B. Calia*, 2004, vol. 5490, pp. 1238–1246.
42. W. H. Southwell, "Wave-front estimation from wave-front slope measurements," *J. Opt. Soc. Am.*, vol. 70, no. 8, p. 998, Aug. 1980.
43. R. Cubalchini, "Modal wave-front estimation from phase derivative measurements," *J. Opt. Soc. Am.*, vol. 69, no. 7, p. 972, Jul. 1979.
44. W. Drexler and J. G. Fujimoto, "State-of-the-art retinal optical coherence tomography.," *Prog. Retin. Eye Res.*, vol. 27, no. 1, pp. 45–88, Jan. 2008.
45. B. Potsaid, B. Baumann, D. Huang, S. Barry, A. E. Cable, J. S. Schuman, J. S. Duker, and J. G. Fujimoto, "Ultrahigh speed 1050nm swept source / Fourier domain OCT retinal and anterior segment imaging at 100,000 to 400,000 axial scans per second," *Opt. Express*, vol. 18, no. 19, p. 20029, Sep. 2010.
46. C. Blatter, T. Klein, B. Grajciar, T. Schmoll, W. Wieser, R. Andre, R. Huber, and R. A. Leitgeb, "Ultrahigh-speed non-invasive widefield angiography," *J. Biomed. Opt.*, vol. 17, no. 7, p. 070505, Jun. 2012.
47. L. An, P. Li, T. T. Shen, and R. Wang, "High speed spectral domain optical coherence tomography for retinal imaging at 500,000 A-lines per second.," *Biomed. Opt. Express*, vol. 2, no. 10, pp. 2770–83, Oct. 2011.
48. Y. K. Tao, J. P. Ehlers, C. A. Toth, and J. A. Izatt, "Intraoperative spectral domain optical coherence tomography for vitreoretinal surgery," *Opt. Lett.*, vol. 35, no. 20, p. 3315, Oct. 2010.

49. M. Sylwestrzak, D. Szlag, M. Szkulmowski, I. Gorczynska, D. Bukowska, M. Wojtkowski, P. Targowski, and P. Sylwestrzak, M., Szlag, D., Szkulmowski, M., Gorczynska, I., Bukowska, D., Wojtkowski, M., and Targowski, "Four-dimensional structural and Doppler optical coherence tomography imaging on graphics processing units.," *J. Biomed. Opt.*, vol. 17, no. 10, p. 100502, Oct. 2012.
50. K. K. C. Lee, A. Mariampillai, J. X. Z. Yu, D. W. Cadotte, B. C. Wilson, B. A. Standish, and V. X. D. Yang, "Real-time speckle variance swept-source optical coherence tomography using a graphics processing unit.," *Biomed. Opt. Express*, vol. 3, no. 7, pp. 1557–64, Jul. 2012.
51. J. Li, P. Bloch, J. Xu, M. V Sarunic, and L. Shannon, "Performance and scalability of Fourier domain optical coherence tomography acceleration using graphics processing units.," *Appl. Opt.*, vol. 50, no. 13, pp. 1832–1838, 2011.
52. J. Rasakanthan, K. Sugden, and P. H. Tomlins, "Processing and rendering of Fourier domain optical coherence tomography images at a line rate over 524 kHz using a graphics processing unit.," *J. Biomed. Opt.*, vol. 16, no. 2, p. 020505, Feb. 2011.
53. M. Sylwestrzak, D. Szlag, M. Szkulmowski, and P. Targowski, "Real-time massively parallel processing of spectral optical coherence tomography data on graphics processing units," in *Proceedings of SPIE*, 2011, vol. 8091, no. 1, p. 80910V–80910V–7.
54. Y. Watanabe and T. Itagaki, "Real-time display on Fourier domain optical coherence tomography system using a graphics processing unit.," *J. Biomed. Opt.*, vol. 14, no. 6, p. 060506, Jan. 2009.
55. K. Zhang and J. U. Kang, "Graphics processing unit-based ultrahigh speed real-time multidimensional Fourier domain optical coherence tomography," in *IEEE Journal of Selected Topics in Quantum Electronics*, 2012, vol. 18, no. 4, p. 82132B–82132B–13.
56. A. E. Desjardins, B. J. Vakoc, M. J. Suter, S.-H. Yun, G. J. Tearney, and B. E. Bouma, "Real-time FPGA processing for high-speed optical frequency domain imaging.," *IEEE Trans. Med. Imaging*, vol. 28, no. 9, pp. 1468–72, Sep. 2009.
57. T. E. Ustun, N. V Iftimia, R. D. Ferguson, and D. X. Hammer, "Real-time processing for Fourier domain optical coherence tomography using a field programmable gate array.," *Rev. Sci. Instrum.*, vol. 79, no. 11, p. 114301, Nov. 2008.
58. M. Adhi and J. S. Duker, "Optical coherence tomography--current and future applications.," *Curr. Opin. Ophthalmol.*, vol. 24, no. 3, pp. 213–221, May 2013.
59. A. Mariampillai, M. K. K. Leung, M. Jarvi, B. A. Standish, K. Lee, B. C. Wilson, A. Vitkin, and V. X. D. Yang, "Optimized speckle variance OCT imaging of microvasculature.," *Opt. Lett.*, vol. 35, no. 8, pp. 1257–9, Apr. 2010.

60. J. Fingler, R. J. Zawadzki, J. S. Werner, D. Schwartz, and S. E. Fraser, "Volumetric microvascular imaging of human retina using optical coherence tomography with a novel motion contrast technique.," *Opt. Express*, vol. 17, no. 24, pp. 22190–200, Nov. 2009.
61. R. K. Wang, L. An, P. Francis, and D. J. Wilson, "Depth-resolved imaging of capillary networks in retina and choroid using ultrahigh sensitive optical microangiography.," *Opt. Lett.*, vol. 35, no. 9, pp. 1467–9, May 2010.
62. P. Sylwestrzak, M., Szlag, D., Szkulmowski, M., Gorczynska, I., Bukowska, D., Wojtkowski, M., and Targowski, "Four-dimensional structural and Doppler optical coherence tomography imaging on graphics processing units and Doppler optical coher-," *J. Biomed. Opt.*
63. Opengl, D. Shreiner, M. Woo, J. Neider, and T. Davis, *OpenGL(R) Programming Guide: The Official Guide to Learning OpenGL(R), Version 2 (5th Edition)*. Addison-Wesley Professional, 2005.
64. M. Harris, S. Sengupta, and J. Owens, "Parallel Prefix Sum (Scan) with CUDA," in *GPU Gems 3*, H. Nguyen, Ed. Addison Wesley, 2007.
65. J. Probst, D. Hillmann, E. Lankenau, C. Winter, S. Oelckers, P. Koch, and G. Hüttmann, "Optical coherence tomography with online visualization of more than seven rendered volumes per second.," *J. Biomed. Opt.*, vol. 15, no. 2, p. 026014, Jan. 2010.
66. S. Van Der Jeught, A. Bradu, and A. G. Podoleanu, "Real-time resampling in Fourier domain optical coherence tomography using a graphics processing unit.," *J. Biomed. Opt.*, vol. 15, no. 3, p. 030511, Jan. 2010.
67. D. Ruijters and P. Thevenaz, "GPU Prefilter for Accurate Cubic B-spline Interpolation," *Comput. J.*, vol. 55, no. 1, pp. 15–20, Dec. 2012.
68. A. Mariampillai, B. A. Standish, E. H. Moriyama, M. Khurana, N. R. Munce, M. K. K. Leung, J. Jiang, A. Cable, B. C. Wilson, I. A. Vitkin, and V. X. D. Yang, "Speckle variance detection of microvasculature using swept-source optical coherence tomography," *Opt. Lett.*, vol. 33, no. 13, pp. 1530–1532, Jun. 2008.
69. B. Hermann, E. J. Fernández, A. Unterhuber, H. Sattmann, A. Fercher, W. Drexler, P. M. Prieto, and P. Artal, "Adaptive-optics ultrahigh-resolution optical coherence tomography.," *Opt. Lett.*, vol. 29, no. 18, pp. 2142–2144, Sep. 2004.
70. Y. Zhang, B. Cense, J. Rha, R. S. Jonnal, W. Gao, R. J. Zawadzki, J. S. Werner, S. Jones, S. Olivier, and D. T. Miller, "High-speed volumetric imaging of cone photoreceptors with adaptive optics spectral-domain optical coherence tomography.," *Opt. Express*, vol. 14, no. 10, pp. 4380–4394, May 2006.
71. R. J. Zawadzki, S. M. Jones, S. Pilli, S. Balderas-Mata, D. Y. Kim, S. S. Olivier, and J. S. Werner, "Integrated adaptive optics optical coherence tomography and adaptive optics scanning laser ophthalmoscope system for simultaneous cellular

- resolution in vivo retinal imaging.," *Biomed. Opt. Express*, vol. 2, no. 6, pp. 1674–1686, Jun. 2011.
72. A. Dubra, Y. Sulai, J. L. Norris, R. F. Cooper, A. M. Dubis, D. R. Williams, and J. Carroll, "Noninvasive imaging of the human rod photoreceptor mosaic using a confocal adaptive optics scanning ophthalmoscope.," *Biomed. Opt. Express*, vol. 2, no. 7, pp. 1864–76, Jul. 2011.
 73. D. X. Hammer, R. D. Ferguson, M. Mujat, D. P. Biss, N. V. Iftimia, A. H. Patel, E. Plumb, M. Campbell, J. L. Norris, A. Dubra, T. Y. P. Chui, J. D. Akula, and A. B. Fulton, "Advanced capabilities of the multimodal adaptive optics imager," *SPIE BiOS*, p. 78850A–78850A–11, 2011.
 74. S. Manzanera, M. A. Helmbrecht, C. J. Kempf, and A. Roorda, "MEMS segmented-based adaptive optics scanning laser ophthalmoscope.," *Biomed. Opt. Express*, vol. 2, no. 5, pp. 1204–17, Jan. 2011.
 75. O. P. Kocaoglu, S. Lee, R. S. Jonnal, Q. Wang, A. E. Herde, J. C. Derby, W. Gao, and D. T. Miller, "Imaging cone photoreceptors in three dimensions and in time using ultrahigh resolution optical coherence tomography with adaptive optics.," *Biomed. Opt. Express*, vol. 2, no. 4, pp. 748–763, Jan. 2011.
 76. M. Pircher, E. Götzinger, H. Sattmann, R. A. Leitgeb, and C. K. Hitzenberger, "In vivo investigation of human cone photoreceptors with SLO/OCT in combination with 3D motion correction on a cellular level," *Opt. Express*, vol. 18, no. 13, p. 13935, Jun. 2010.
 77. S. Remtulla and P. E. Hallett, "A schematic eye for the mouse, and comparisons with the rat," *Vision Res.*, vol. 25, no. 1, pp. 21–31, Jan. 1985.
 78. C. Schmucker and F. Schaeffel, "A paraxial schematic eye model for the growing C57BL/6 mouse.," *Vision Res.*, vol. 44, no. 16, pp. 1857–67, Jan. 2004.
 79. E. G. de la Cera, G. Rodríguez, L. Llorente, F. Schaeffel, and S. Marcos, "Optical aberrations in the mouse eye.," *Vision Res.*, vol. 46, no. 16, pp. 2546–53, Aug. 2006.
 80. D. P. Biss, R. H. Webb, Y. Zhou, T. G. Bifano, P. Zamiri, and C. P. Lin, "An adaptive optics biomicroscope for mouse retinal imaging," in *Proceedings of SPIE*, 2007, vol. 6467, no. 1, pp. 646703–646703–8.
 81. D. P. Biss, D. Sumorok, S. A. Burns, R. H. Webb, Y. Zhou, T. G. Bifano, D. Côté, I. Veilleux, P. Zamiri, and C. P. Lin, "In vivo fluorescent imaging of the mouse retina using adaptive optics.," *Opt. Lett.*, vol. 32, no. 6, pp. 659–661, Mar. 2007.
 82. C. Alt, D. P. Biss, N. Tajouri, T. C. Jakobs, and C. P. Lin, "An adaptive-optics scanning laser ophthalmoscope for imaging murine retinal microstructure," *Bios*, vol. 7550, pp. 1–11, 2010.

83. Y. Geng, A. Dubra, L. Yin, W. H. Merigan, R. Sharma, R. T. Libby, and D. R. Williams, "Adaptive optics retinal imaging in the living mouse eye," *Biomed. Opt. Express*, vol. 3, no. 4, pp. 715–734, Apr. 2012.
84. O. P. Kocaoglu, S. R. Uhlhorn, E. Hernandez, R. A. Juarez, R. Will, J.-M. Parel, and F. Manns, "Simultaneous Fundus Imaging and Optical Coherence Tomography of the Mouse Retina," *Invest. Ophthalmol. Vis. Sci.*, vol. 48, no. 3, pp. 1283–1289, Mar. 2007.
85. S. Hariri, A. A. Moayed, A. Dracopolos, C. Hyun, S. Boyd, and K. Bizheva, "Limiting factors to the OCT axial resolution for in-vivo imaging of human and rodent retina in the 1060nm wavelength range," *Opt. Express*, vol. 17, no. 26, pp. 24304–24316, Dec. 2009.
86. M. D. Fischer, G. Huber, S. C. Beck, N. Tanimoto, R. Muehlfriedel, E. Fahl, C. Grimm, A. Wenzel, C. E. Remé, S. a van de Pavert, J. Wijnholds, M. Pacal, R. Bremner, and M. W. Seeliger, "Noninvasive, in vivo assessment of mouse retinal structure using optical coherence tomography.," *PLoS One*, vol. 4, no. 10, p. e7507, Jan. 2009.
87. M. L. Gabriele, H. Ishikawa, J. S. Schuman, R. A. Bilonick, J. Kim, L. Kagemann, and G. Wollstein, "Reproducibility of spectral-domain optical coherence tomography total retinal thickness measurements in mice.," *Invest. Ophthalmol. Vis. Sci.*, vol. 51, no. 12, pp. 6519–23, Dec. 2010.
88. R. Leitgeb, L. Schmetterer, W. Drexler, A. Fercher, R. Zawadzki, and T. Bajraszewski, "Real-time assessment of retinal blood flow with ultrafast acquisition by color Doppler Fourier domain optical coherence tomography," *Opt. Express*, vol. 11, no. 23, pp. 3116–3121, Nov. 2003.
89. W. Choi, B. Baumann, J. J. Liu, A. C. Clermont, E. P. Feener, J. S. Duker, and J. G. Fujimoto, "Measurement of pulsatile total blood flow in the human and rat retina with ultrahigh speed spectral/Fourier domain OCT.," *Biomed. Opt. Express*, vol. 3, no. 5, pp. 1047–61, May 2012.
90. D. X. Hammer, M. Mujat, R. D. Ferguson, N. Iftimia, D. Escobedo, J. T. Jenkins, H. Lim, T. E. Milner, and M. D. Feldman, "Imaging flow dynamics in murine coronary arteries with spectral domain optical Doppler tomography.," *Biomed. Opt. Express*, vol. 3, no. 4, pp. 701–14, Apr. 2012.
91. D. W. Cadotte, A. Mariampillai, A. Cadotte, K. K. C. Lee, T.-R. Kiehl, B. C. Wilson, M. G. Fehlings, and V. X. D. Yang, "Speckle variance optical coherence tomography of the rodent spinal cord: in vivo feasibility.," *Biomed. Opt. Express*, vol. 3, no. 5, pp. 911–9, May 2012.
92. Z. Zhi, X. Yin, S. Dziennis, T. Wietecha, K. L. Hudkins, C. E. Alpers, and R. K. Wang, "Optical microangiography of retina and choroid and measurement of total retinal blood flow in mice.," *Biomed. Opt. Express*, vol. 3, no. 11, pp. 2976–86, Nov. 2012.

93. ANSI, "American National Standard for the Safe Use of Lasers ANSI Z136.1-2007.," *Laser Institute of America*, 2007. .
94. N. M. Putnam, D. X. Hammer, Y. Zhang, D. Merino, and A. Roorda, "Modeling the foveal cone mosaic imaged with adaptive optics scanning laser ophthalmoscopy," *Opt. Express*, vol. 18, no. 24, p. 24902, Nov. 2010.
95. S. A. Rahman and M. J. Booth, "Adaptive optics for high-resolution microscopy: wave front sensing using back scattered light," *Proc. SPIE MOEMS-MEMS*, vol. 8253, p. 82530I–82530I–5, Feb. 2012.
96. T. M. S. Greiling and J. I. Clark, "The transparent lens and cornea in the mouse and zebra fish eye.," *Semin. Cell Dev. Biol.*, vol. 19, no. 2, pp. 94–9, Apr. 2008.
97. R. J. Zawadzki, B. Cense, Y. Zhang, S. S. Choi, D. T. Miller, and J. S. Werner, "Ultrahigh-resolution optical coherence tomography with monochromatic and chromatic aberration correction.," *Opt. Express*, vol. 16, no. 11, pp. 8126–43, May 2008.
98. X. Zhou, P. Bedggood, and A. Metha, "Limitations to adaptive optics image quality in rodent eyes," *Biomed. Opt. Express*, vol. 3, no. 8, pp. 1811–1824, Jul. 2012.
99. L. Fenno, O. Yizhar, and K. Deisseroth, "The development and application of optogenetics.," *Annu. Rev. Neurosci.*, vol. 34, pp. 389–412, Jan. 2011.
100. D. Oron, E. Papagiakoumou, F. Anselmi, and V. Emiliani, "Two-photon optogenetics.," *Prog. Brain Res.*, vol. 196, pp. 119–43, Jan. 2012.
101. M. Pircher, E. Götzinger, and C. K. Hitzenberger, "Dynamic focus in optical coherence tomography for retinal imaging.," *J. Biomed. Opt.*, vol. 11, no. 5, p. 054013, Jan. 2006.
102. R. A. Leitgeb, M. Villiger, A. H. Bachmann, L. Steinmann, and T. Lasser, "Extended focus depth for Fourier domain optical coherence microscopy," *Opt. Lett.*, vol. 31, no. 16, pp. 2450–2452, Aug. 2006.
103. K. Sasaki, K. Kurokawa, S. Makita, and Y. Yasuno, "Extended depth of focus adaptive optics spectral domain optical coherence tomography.," *Biomed. Opt. Express*, vol. 3, no. 10, pp. 2353–70, Oct. 2012.
104. W. J. Donnelly III and A. Roorda, "Optimal pupil size in the human eye for axial resolution," *J. Opt. Soc. Am. A*, vol. 20, no. 11, p. 2010, 2003.
105. P. Godara, A. M. Dubis, A. Roorda, J. L. Duncan, and J. Carroll, "Adaptive optics retinal imaging: emerging clinical applications.," *Optom. Vis. Sci.*, vol. 87, no. 12, pp. 930–941, Dec. 2010.
106. D. X. Hammer, R. D. Ferguson, M. Mujat, A. Patel, E. Plumb, N. Iftimia, T. Y. P. Chui, J. D. Akula, and A. B. Fulton, "Multimodal adaptive optics retinal imager:

- design and performance.," *J. Opt. Soc. Am. A. Opt. Image Sci. Vis.*, vol. 29, no. 12, pp. 2598–2607, Dec. 2012.
107. J. W. Evans, R. J. Zawadzki, S. M. Jones, S. S. Olivier, and J. S. Werner, "Error budget analysis for an adaptive optics optical coherence tomography system.," *Opt. Express*, vol. 17, no. 16, pp. 13768–13784, Aug. 2009.
 108. A. Jesacher and M. J. Booth, "Sensorless adaptive optics for microscopy," in *SPIE MOEMS-MEMS*, 2011, p. 79310G–9.
 109. H. Hofer, N. Sredar, H. Queener, C. Li, and J. Porter, "Wavefront sensorless adaptive optics ophthalmoscopy in the human eye.," *Opt. Express*, vol. 19, no. 15, pp. 14160–14171, Jul. 2011.
 110. P. Villoresi, S. Bonora, M. Pascolini, L. Poletto, G. Tondello, C. Vozzi, M. Nisoli, G. Sansone, S. Stagira, and S. De Silvestri, "Optimization of high-order harmonic generation by adaptive control of a sub-10-fs pulse wave front," *Opt. Lett.*, vol. 29, no. 2, p. 207, 2004.
 111. M. J. Booth, "Wavefront sensorless adaptive optics for large aberrations," *Opt. Lett.*, vol. 32, no. 1, p. 5, Jan. 2007.
 112. M. Minozzi, S. Bonora, A. V Sergienko, G. Vallone, and P. Villoresi, "Optimization of two-photon wave function in parametric down conversion by adaptive optics control of the pump radiation.," *Opt. Lett.*, vol. 38, no. 4, pp. 489–91, Feb. 2013.
 113. R. J. S. Bonora, Zawadzki, "Wavefront sensorless modal deformable mirror correction in Adaptive Optics - Optical Coherence Tomography," *Opt. Lett.*, vol. 38, p. 22, 2013.
 114. C. J. Kempf, M. A. Helmbrecht, and M. Besse, "Adaptive optics control system for segmented MEMS deformable mirrors," in *Proc. SPIE 7595, MEMS Adaptive Optics IV*, 2010, vol. 7595, p. 75950M–12.
 115. J. Schindelin, I. Arganda-Carreras, E. Frise, V. Kaynig, M. Longair, T. Pietzsch, S. Preibisch, C. Rueden, S. Saalfeld, B. Schmid, J.-Y. Tinevez, D. J. White, V. Hartenstein, K. Eliceiri, P. Tomancak, and A. Cardona, "Fiji: an open-source platform for biological-image analysis.," *Nat. Methods*, vol. 9, no. 7, pp. 676–682, Jul. 2012.
 116. R. A. Muller and A. Buffington, "Real-time correction of atmospherically degraded telescope images through image sharpening," *J. Opt. Soc. Am.*, vol. 64, no. 9, p. 1200, Sep. 1974.
 117. L. Thibos, R. A. Applegate, J. T. Schwiegerling, and V. S. T. M. Webb, Robert, "Standards for reporting the optical aberrations of eyes - OSA Technical Digest," in *Vision Science and its Applications*, 2000, vol. 35, pp. 232–244.

118. D. Debarre, M. J. Booth, and T. Wilson, "Image based adaptive optics through optimisation of low spatial frequencies," *Opt. Express*, vol. 15, no. 13, p. 8176, Jun. 2007.
119. S. Tuohy and A. G. Podoleanu, "Depth-resolved wavefront aberrations using a coherence-gated Shack-Hartmann wavefront sensor.," *Opt. Express*, vol. 18, no. 4, pp. 3458–3476, Feb. 2010.
120. S. A. Rahman and M. J. Booth, "Direct wavefront sensing in adaptive optical microscopy using backscattered light.," *Appl. Opt.*, vol. 52, no. 22, pp. 5523–5532, Aug. 2013.
121. M. Shaw, K. O'Holleran, and C. Paterson, "Investigation of the confocal wavefront sensor and its application to biological microscopy.," *Opt. Express*, vol. 21, no. 16, pp. 19353–19362, Aug. 2013.
122. J. Wang, J.-F. Léger, J. Binding, A. C. Boccara, S. Gigan, and L. Bourdieu, "Measuring aberrations in the rat brain by coherence-gated wavefront sensing using a Linnik interferometer.," *Biomed. Opt. Express*, vol. 3, no. 10, pp. 2510–25, Oct. 2012.
123. R. J. Zawadzki, S. S. Choi, S. M. Jones, S. S. Oliver, and J. S. Werner, "Adaptive optics-optical coherence tomography: optimizing visualization of microscopic retinal structures in three dimensions.," *J. Opt. Soc. Am. A. Opt. Image Sci. Vis.*, vol. 24, no. 5, pp. 1373–83, May 2007.
124. N. S. KAPANY, N. A. PEPPERS, H. C. ZWENG, and M. FLOCKS, "Retinal Photocoagulation by Lasers," *Nature*, vol. 199, no. 4889, pp. 146–149, Jul. 1963.
125. A. Jain, M. S. Blumenkranz, Y. Paulus, M. W. Wiltberger, D. E. Andersen, P. Huie, and D. Palanker, "Effect of pulse duration on size and character of the lesion in retinal photocoagulation.," *Arch. Ophthalmol.*, vol. 126, no. 1, pp. 78–85, Jan. 2008.
126. K. E. Higgins, S. M. Meyers, M. J. Jaffe, M. S. Roy, and F. M. de Monasterio, "Temporary loss of foveal contrast sensitivity associated with panretinal photocoagulation.," *Arch. Ophthalmol.*, vol. 104, no. 7, pp. 997–1003, Jul. 1986.
127. M. Shimura, K. Yasuda, T. Nakazawa, and M. Tamai, "Visual dysfunction after panretinal photocoagulation in patients with severe diabetic retinopathy and good vision.," *Am. J. Ophthalmol.*, vol. 140, no. 1, pp. 8–15, Jul. 2005.
128. Y. M. Paulus, A. Jain, R. F. Gariano, B. V Stanzel, M. Marmor, M. S. Blumenkranz, and D. Palanker, "Healing of retinal photocoagulation lesions.," *Invest. Ophthalmol. Vis. Sci.*, vol. 49, no. 12, pp. 5540–5, Dec. 2008.
129. C. Alt and C. Lin, "In vivo quantification of microglia dynamics with a scanning laser ophthalmoscope in a mouse model of focal laser injury," in *Proceedings of SPIE; Ophthalmic Technologies XXII, Volume 8209*, 2012, pp. 820907– 1 – 9.

130. D. Lavinsky, T. W. Chalberg, Y. Mandel, P. Huie, R. Dalal, M. Marmor, and D. Palanker, "Modulation of Transgene Expression in Retinal Gene Therapy by Selective Laser Treatment.," *Invest. Ophthalmol. Vis. Sci.*, pp. iovs.12–10933–, Feb. 2013.
131. R. Brinkmann, J. Roider, and R. Birngruber, "Selective retina therapy (SRT): a review on methods, techniques, preclinical and first clinical results.," *Bull. Soc. Belge Ophthalmol.*, no. 302, pp. 51–69, Jan. 2006.
132. A. Sher, B. W. Jones, P. Huie, Y. M. Paulus, D. Lavinsky, L.-S. S. Leung, H. Nomoto, C. Beier, R. E. Marc, and D. Palanker, "Restoration of retinal structure and function after selective photocoagulation.," *J. Neurosci.*, vol. 33, no. 16, pp. 6800–8, Apr. 2013.
133. G. M. Pocock, A. Boretzky, P. Gupta, J. W. Oliver, and M. Motamedi, "Laser injury and in vivo multimodal imaging using a mouse model," in *SPIE BiOS*, 2011, pp. 789713–789713–7.
134. Y. M. Paulus, A. Jain, H. Nomoto, C. Sramek, R. F. Gariano, D. Andersen, G. Schuele, L.-S. Leung, T. Leng, and D. Palanker, "Selective retinal therapy with microsecond exposures using a continuous line scanning laser.," *Retina*, vol. 31, no. 2, pp. 380–8, Feb. 2011.
135. C. K. Sheehy, Q. Yang, D. W. Arathorn, P. Tiruveedhula, J. F. de Boer, and A. Roorda, "High-speed, image-based eye tracking with a scanning laser ophthalmoscope.," *Biomed. Opt. Express*, vol. 3, no. 10, pp. 2611–22, Oct. 2012.
136. M. Booth, "Wave front sensor-less adaptive optics: a model-based approach using sphere packings," *Opt. Express*, vol. 14, no. 4, p. 1339, 2006.
137. W. Denk, J. Strickler, and W. Webb, "Two-photon laser scanning fluorescence microscopy," *Science (80-.)*, vol. 248, no. 4951, pp. 73–76, Apr. 1990.
138. E. Beaurepaire, L. Moreaux, F. Amblard, and J. Mertz, "Combined scanning optical coherence and two-photon-excited fluorescence microscopy," *Opt. Lett.*, vol. 24, no. 14, p. 969, Jul. 1999.
139. C. Vinegoni, T. Ralston, W. Tan, W. Luo, D. L. Marks, and S. A. Boppart, "Integrated structural and functional optical imaging combining spectral-domain optical coherence and multiphoton microscopy," *Appl. Phys. Lett.*, vol. 88, no. 5, p. 053901, Jan. 2006.
140. S. Tang, Y. Zhou, K. K. H. Chan, and T. Lai, "Multiscale multimodal imaging with multiphoton microscopy and optical coherence tomography," *Opt. Lett.*, vol. 36, no. 24, p. 4800, Dec. 2011.
141. J. J. Hunter, B. Masella, A. Dubra, R. Sharma, L. Yin, W. H. Merigan, G. Palczewska, K. Palczewski, and D. R. Williams, "Images of photoreceptors in living primate eyes using adaptive optics two-photon ophthalmoscopy.," *Biomed. Opt. Express*, vol. 2, no. 1, pp. 139–48, Jan. 2010.

142. R. Sharma, L. Yin, Y. Geng, W. H. Merigan, G. Palczewska, K. Palczewski, D. R. Williams, and J. J. Hunter, "In vivo two-photon imaging of the mouse retina.," *Biomed. Opt. Express*, vol. 4, no. 8, pp. 1285–93, Jan. 2013.
143. W. R. Zipfel, R. M. Williams, and W. W. Webb, "Nonlinear magic: multiphoton microscopy in the biosciences.," *Nat. Biotechnol.*, vol. 21, no. 11, pp. 1369–77, Nov. 2003.
144. Z. Ding, H. Ren, Y. Zhao, J. S. Nelson, and Z. Chen, "High-resolution optical coherence tomography over a large depth range with an axicon lens.," *Opt. Lett.*, vol. 27, no. 4, pp. 243–5, Feb. 2002.
145. C. Blatter, B. Grajciar, C. M. Eigenwillig, W. Wieser, B. R. Biedermann, R. Huber, and R. a Leitgeb, "Extended focus high-speed swept source OCT with self-reconstructive illumination.," *Opt. Express*, vol. 19, no. 13, pp. 12141–55, Jun. 2011.
146. D. Lorensen, C. Christian Singe, A. Curatolo, and D. D. Sampson, "Energy-efficient low-Fresnel-number Bessel beams and their application in optical coherence tomography," *Opt. Lett.*, vol. 39, no. 3, p. 548, Jan. 2014.

Appendix A.

Zernike Polynomials up to 5th order

| index | Meaning | Zernike term |
|--------------|----------------------|--|
| Zeroth order | | |
| 0 | Piston | 1 |
| First order | | |
| 1 | Vertical prism | $2\rho\sin(\theta)$ |
| 2 | Horizontal prism | $2\rho\cos(\theta)$ |
| second order | | |
| 3 | Astigmatism | $\sqrt{6}\rho^2\sin(2\theta)$ |
| 4 | Defocus | $\sqrt{3}(2\rho^2-1)$ |
| 5 | Astigmatism | $\sqrt{6}\rho^2\cos(2\theta)$ |
| Third order | | |
| 6 | Trefoil | $\sqrt{8}\rho^3\sin(3\theta)$ |
| 7 | Vertical coma | $\sqrt{8}(3\rho^3-2\rho)\sin(\theta)$ |
| 8 | Horizontal coma | $\sqrt{8}(3\rho^3-2\rho)\cos(\theta)$ |
| 9 | Trefoil | $\sqrt{8}\rho^3\cos(3\theta)$ |
| Fourth order | | |
| 10 | Quadrafoil | $\sqrt{10}\rho^4\sin(4\theta)$ |
| 11 | Secondary astig. | $\sqrt{10}(4\rho^4-3\rho^2)\sin(2\theta)$ |
| 12 | Spherical aberration | $\sqrt{5}(6\rho^4-6\rho^2+1)$ |
| 13 | Secondary astig. | $\sqrt{10}(4\rho^4-3\rho^2)\cos(2\theta)$ |
| 14 | Quadrafoil | $\sqrt{10}\rho^4\cos(4\theta)$ |
| Fifth order | | |
| 15 | | $\sqrt{12}\rho^5\sin(5\theta)$ |
| 16 | | $\sqrt{12}(5\rho^5-4\rho^3)\sin(3\theta)$ |
| 17 | | $\sqrt{12}(10\rho^5-12\rho^3+3\rho)\sin(\theta)$ |
| 18 | | $\sqrt{12}(10\rho^5-12\rho^3+3\rho)\cos(\theta)$ |
| 19 | | $\sqrt{12}(5\rho^5-4\rho^3)\cos(3\theta)$ |
| 20 | | $\sqrt{12}\rho^5\cos(5\theta)$ |